Novel bioinspired and biohybrid electrode materials for hydrogen production

Afridi Zamader

UPPSALA UNIVERSITET

Université Grenoble Alpes

THÈSE

Pour obtenir le grade de

DOCTEUR DE L'UNIVERSITÉ GRENOBLE ALPES
et de l'UNIVERSITÉ D'UPPSALA

École doctorale :	École Doctorale de Chimie et Sciences du Vivant
Spécialité :	Chimie inorganique et bio-inorganique
Unité de recherche :	Laboratoire de Chimie et Biologie des Métaux

Nouveaux matériaux d'électrode bioinspirés et biohybrides pour la production d'hydrogène

Novel bioinspired and biohybrid electrode materials for hydrogen production

Présentée par :

Afridi ZAMADER

Direction de thèse :

Vincent ARTERO
Directeur de recherche, CEA — Directeur de thèse

Gustav BERGGREN
Professeur Associé, Uppsala Universitet — Co-Directeur de thèse

Rapporteurs :

Marc ROBERT
Professeur, Université Paris Cité

Ulf-Peter APFEL
Professeur, Ruhr-University, Bochum

Thèse soutenue publiquement le **10 February 2023**, devant le jury composé de :

Marc ROBERT Professeur, Université Paris Cité	Rapporteur
Ulf-Peter APFEL Professeur, Ruhr-University, Bochum	Rapporteur
Helena GRENNBERG Professeure, Uppsala Universitet	Présidente du jury
Ola F. WENDT Professeur, Uppsala Universitet	Examinateur
Anders THAPPER Professeur Assistant, Uppsala Universitet	Examinateur

Titre : Nouveaux matériaux bioinspirés et biohybrides d'électrodes pour la production d'hydrogène

Mots clés : eSCALED, dispositif, feuille artificielle, hydrogène, hydrogénase, catalyseur, électrode

Résumé : Cette thèse a été réalisée dans le cadre du projet eSCALED administré par le programme MSCA horizon 2020 de l'UE, qui visait à développer un dispositif appelé "feuille artificielle" chargé de générer des carburants ou des produits chimiques liquides (production de H_2 ou réduction de CO_2) à l'aide de l'électrolyse solaire. La décomposition de l'eau par électrolyse est l'un des moyens les plus durables de produire de l'hydrogène, qui est alors qualifié de « décarboné » ou « vert ». Ce procédé nécessite un catalyseur (c'est-à-dire un matériau qui accélère la réaction). Les enzymes hydrogénases (catalyseurs naturels protéiques) produisent de l'hydrogène à partir d'eau avec une vitesse et un rendement et une vitesse excellents.

Ma thèse est focalisée sur le développement des catalyseurs inspirés par le site actif de l'hydrogénase à fer et leur intégration dans des matériaux d'électrode pour la production d'hydrogène dans l'eau.

Tout d'abord, nous avons élaboré une stratégie pour immobiliser fortement le catalyseur sur l'électrode et conçu le catalyseur en conséquence. Ensuite, nous avons amélioré la catalyse en améliorant la conception du catalyseur. Nous avons également préparé et étudié une hydrogénase modifiée afin de comprendre les éléments clés du mécanisme responsable de l'activité de l'enzyme.

Title: Novel bioinspired and biohybrid electrode materials for hydrogen production

Keywords : eSCALED, device, artificial leaf, hydrogen, hydrogenase, catalyst, electrode

Abstract: This thesis was accomplished under the scope of eSCALED project administrated by EU MSCA horizon 2020 program, which aimed to develop a device called "artificial leaf" responsible for generating fuels or liquid chemicals (H_2 production or CO_2 reduction) using solar electrolysis.

Hydrogen (H_2) can be used as fuel in H_2/O_2 fuel cell (cell that produces electricity from chemical reaction) to generate electricity with heat and water as sub-products. Water (H_2O) splitting powered by solar energy is one of the most sustainable (environmentally friendly) ways to produce H_2, which requires catalyst (*i.e*. material that make reaction faster).

Hydrogenase enzymes (catalyst made by Nature) do the H_2 production at excellent rate (~10,000 molecules of H_2 per molecule of enzyme per second) in water.

My thesis focused on developing catalysts inspired from hydrogenase and anchor them on electrode (a conductive material that exchanges electron) for H_2 production in water. Firstly, we planned a strategy to immobilize the catalyst on electrode strongly and designed the catalyst accordingly. Subsequently, we improved the catalysis (H_2 production) by redesigning the catalyst. We also prepared and studied a modified hydrogenase to understand some key science run inside the enzyme.

“I have no special talent. I am only passionately curious. The important thing is to not stop questioning. Curiosity has its own reason for existing.”

–Albert Einstein

List of Papers

This thesis is based on the following papers, which are referred to in the text by their Roman numerals.

I. **Zamader, A**.; Reuillard, B.; Pécaut, J.; Billon, L.; Bousquet, A.; Berggren, G.; Artero, V. Non-Covalent Integration of a [FeFe]-Hydrogenase Mimic to Multiwalled Carbon Nanotubes for Electrocatalytic Hydrogen Evolution. *Chem. Eur. J.* **2022**, *e202202260* (n/a)4.
Author's contribution: I synthesized the complexes, and characterized them by spectroscopy and electrochemistry. I analyzed the results, prepared figures, wrote the first draft of the manuscript and was heavily involved in the later stages of manuscript preparation and revisions.

II. **Zamader, A.**; Reuillard, B.; Marcasuzaa, P.; Bousquet, A.; Billon, L.; Gallart, J. J. E.; Berggren, G.; Artero, V. Electrode Integration of Synthetic Hydrogenase as Bio-Inspired and Noble Metal-Free Cathodes for Hydrogen Evolution. *ACS Catal.*, **2023,** 13, 2,1246–1256.
Author's contribution: I synthesized the metallopolymers, characterized them by spectroscopy and electrochemistry; and performed the life cycle assessments. I interpreted the results, prepared the figures, wrote the first draft of the manuscript and was heavily involved in the later stages of manuscript preparation and revisions.

III. **Zamader, A**.; Reuillard, B.; Billon, L.; Berggren, G.; Artero, V. Synthetic Styrene-Based Bioinspired Models of the [FeFe]-Hydrogenase Active Site for Electrocatalytic Hydrogen Evolution. *Manuscript submitted.*
Author's contribution: I contributed by designing and synthesizing metallopolymers. I characterized them by spectroscopy and electrochemistry. I interpreted the results, prepared figures and wrote the first draft of the manuscript.

IV. Lorenzi, M.; Gellett, J.; **Zamader, A.**; Senger, M.; Duan, Z.; Rodríguez-Maciá, P.; Berggren, G. Investigating the Role of the Strong Field Ligands in [FeFe] Hydrogenase: Spectroscopic and Functional Characterization of a Semi-Synthetic Mono-Cyanide Active Site. *Chemical Science* **2022**, 13 (37), 11058–11064.
Author's contribution: I contributed by synthesising the diiron cofactor, and characterized them by spectroscopy. I contributed to the analysis of the results, and the writing of the manuscript.

The first author(s) are highlighted by underlining.

List of Papers that are not included in the thesis

I. Lorenzi, M.; Ceccaldi, P.; Rodríguez-Maciá, P.; Redman, H. J.; **Zamader, A.**; Birrell, J. A.; Mészáros, L. S.; Berggren, G. Stability of the H-Cluster under Whole-Cell Conditions—Formation of an Htrans-like State and Its Reactivity towards Oxygen. *J. Biol. Inorg. Chem.* **2022**, *27* (3), 345–355.

II. Cabotaje, R. P.; Walter, K.; **Zamader, A.**, Huang, P., Ho, F., Land, H., Senger, M., Berggren, G. Probing substrate transport effects in [FeFe] hydrogenase - An alternative proton transfer pathway in putatively sensory [FeFe] hydrogenase. *Manuscript under revision.*

Contents

Abbreviations

GHGs	Greenhouse gases
IEA	International Energy Agency
ESRs	Early stage researchers
$[2Fe]_H$	Diiron active site present in the H-cluster
$[4Fe4S]_H$	Four-iron four- sulfur cluster present in the H-cluster
Fe_p	Proximal iron present in the H-cluster
Fe_d	Distal iron present in the H-cluster
NaDT	Sodium dithionite
AIBN	Azobisisobutyronitrile
RAFT	Reversible Addition-Fragmentation chain Transfer
DOSY	Diffusion-ordered spectroscopy
EPR	Electron paramagnetic resonance
MWNT	Multiwalled carbon nanotubes
THF	Tetrahydrofuran
$TBAPF_6$	Tetrabutylammonium hexafluorophosphate
CV	Cyclic Voltammetry
CA	Chronoamperometry
RHE	Reversible hydrogen electrode
TON_{H2}	Turnover number for H_2 production
XPS	X-ray photoelectronic spectroscopy
OCS	Outer coordination sphere
TOF_{max}	Turnover frequency maxima
DMAEMA	2-(Dimethylamino)ethyl methacrylate
PDMAMEA	Poly-(2-(dimethylamino)ethyl methacrylate)
PyBMA	4-(pyren-1-yl)-butyl methacrylate
ATRP	Atomic transfer radical polymerization
ICP OES	Inductively coupled plasma - optical emission spectrometry
SEC	Size-exclusion chromatography
TFA	Trifluoroacetic acid
GC	Gas chromatography
adt^{2-}	Azaditholate ligand
adt'^{2-}	Azaditholate ligand substituted at bridgehead nitrogen
LCA	Life cycle assessment
LCI	Life cycle inventory

Chapter 1 : Introduction

The climate has a substantial impact on our lives, starting from food production to clothes to living conditions, health and indeed our society's future. Thus, climate change drives the research community, and our societies, towards developing low carbon and cheap alternatives to fossil fuels. Until we uncover such potential alternatives and scale up to industrial level, the world will continue to two face two major problems, (i) poor people will have limited access to energy (ii) fossil fuels will dominate the energy market, which will further push climate change as well as deteriorate human health due to air pollution.

1.1 Current energy consumption and climate condition

The concentration of CO_2 (~440 ppm) in our atmosphere is growing at an alarming rate. As a result, global temperature has increased up to 1.2^0 C from its pre-industrial level **(Figure 1.1)**. In 2021, ~83% of total consumed energy was produced using fossil fuels *i.e.* oil, coal and natural gas (total energy consumed was 595 exajoules).[1] In the same year, ~90% percent of global CO_2 emission originated from fossil fuels (the total CO_2 emission was 34.9 billion ton[2]).[3]

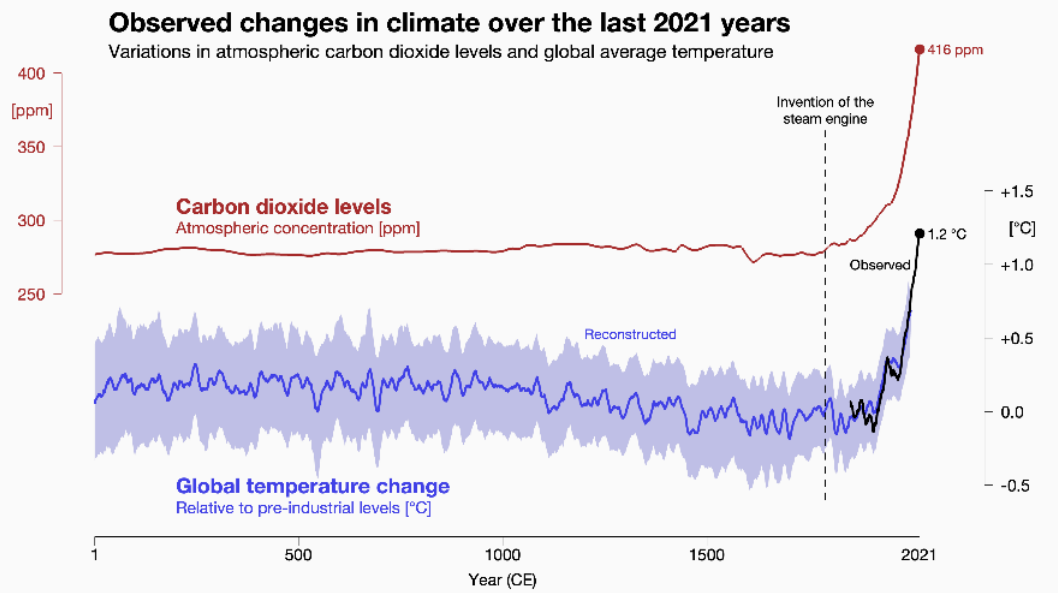

Figure 1.1: CO_2 levels and change in global temperature during the last 2021 years. The image was adopted from "Climate visuals" data by National Centre for Atmospheric Science. All rights are reserved.

The latest report published in 2022 by the "Intergovernmental panel on climate change" (IPCC) called for urgent action against climate change.[4] The report proposed five key steps in order halve the greenhouse gases (GHGs) emissions by 2030, *i.e.* (a) reduction of fossil fuel usage, (b) increase of renewable energy usage, (c) carbon capture and storage, (d) recycling materials to cut down the waste and save energy by avoiding the manufacture of new products from raw materials (e) greener cities (*e.g.* promoting tree planting, encourage public transport by walking, cycling etc.). In the context of energy, storing renewable energy in the form of a carbon-free chemical bond *i.e.* H_2, is one of the most promising approaches to put forward.

1.2 Why Hydrogen (H_2)?

H_2 is potentially the best energy vector to replace our current fossil fuel-based energy system.[5] Oxidation of H_2 delivers an energy output between 120 –140 kJ/mol, which is higher than other combustible carbon based fuels (30 –55 kJ/mol) like coal, diesel, kerosene etc. by a margin. H_2 can be used to feed fuel cells to obtain electricity with only heat and water as side-products. Thus, H_2 offers a solution for the environmental and energy related problems (*i.e.* increasing GHGs emission, global warming) associated with fossil fuels usage.

The International Energy Agency (IEA) has declared H_2 as a promising energy carrier candidate.[6] While "Bloomberg New Energy Finance" reported at the G20 meet in Japan on March 2020 that clean H_2 can help address the GHGs emissions by 2050.[7]

Moreover, in addition to its prospect for carbon free energy storage, H_2 is already being used for some major applications.[8] For example, ammonia (NH_3) production, petroleum refining, methanol (CH_3OH) production, transportation (*e.g.* buses, trains etc.), space industries (rocket fuel and powering spacecrafts), food (hydrogenation of unsaturated fatty acid), medical industries (for generating H_2O_2 for therapeutic application) etc.

As new applications for the gas are envisioned and developed, the demand for hydrogen is continuously increasing. In 2021, around 96 Mt of H_2 was on demand.[9] It has been estimated by the IEA that the demand will be around 180 Mt and 550 Mt in 2030 and 2050, respectively.[9]

1.3 Currently available techniques for H_2 production

The production of H_2 is not green yet. In 2021, ~97% of H_2 (total 96 Mt of H_2 produced[10]) was generated from fossil fuels, causing emissions of nearly 900 Mt of CO_2 (around 0.8% of global CO_2 emission).[11] Therefore, a scalable greener approach is required to yield a zero-emission process. Based on different approaches for its production, H_2 is mainly categorized into three distinct groups, which will be described further below.[5,12]

1.3.1 Grey hydrogen

It is the production of H_2 using natural gas, coal and oil. As mentioned above, this is by far the dominant source currently, and it produces a large amount of CO_2 as side product (~10 kg of CO_2 equivalents emitted per kg of H_2 produced).

1.3.2 Blue hydrogen

This methodology uses the same process as "grey hydrogen" except, the produced CO_2 is captured, used or stored to mitigate the deleterious GHGs effect(s).

1.3.3 Green hydrogen

The H_2 produced via this technique is considered as the most sustainable among the methodologies.[13] The production of "green hydrogen" uses renewable energy (*i.e.* solar, wind etc.) to power the water electrolysis process, or split water (H_2O), to generate H_2 with O_2 as the side product. However, this technology is still immature in term of scalability and about 10 times more expensive than the currently dominant H_2 production strategy (*i.e.* grey hydrogen). In our study we will solely focus on "green hydrogen".

1.3.3.1 Currently available devices for "green hydrogen"

A central component in the production of "green hydrogen" is the electrolyser. Among the current available electrolysers, proton exchange membrane (PEM) and alkaline electrolysers are well known.[14–16]

1.3.3.2 Alkaline electrolysers

This is a typical electrolyser, and consists two compartments (cathode and anode) separated by a microporous membrane (permeable to OH^-) and uses aqueous alkaline electrolytes containing 30 wt% of NaOH or KOH.[16] Normally, the anodes are made of Ni or Cu with a coating of metal (W or Ru) oxides and the cathodes are made of Ni with a coating of Pt. The membrane is made of "Zirfon", a composite of Zirconia (Zr) and polysulfone.

Cathode reaction:

Water reduction takes place at the cathode compartment to generate H_2 and OH^-.

$$2H_2O + 2e^- \longrightarrow H_2 + 2OH^-$$

Anode reaction:

The resulting OH^- diffuses to the anode compartment, where it is oxidized to form oxygen and water.

$$2OH^- \longrightarrow 1/2O_2 + H_2O + 2e^-$$

These electrodes suffer from major drawbacks, including low current densities (0.2 – 0.4 A cm^{-2}) and corrosion due to the caustic basic reaction condition.[16]

1.3.3.3 Acidic electrolyzers

Proton exchange membrane electrolyzers (PEM) or acidic electrolyzers use expensive platinum group metals (PGMs) as cathode and metallic iridium (Ir), Ir-based oxides as anode materials.[14] This is combined with a solid polymer membrane electrolyte (permeable to H^+) and water as reactant.

Anode reaction

The water is oxidized at the anode to produce O_2, H^+ and e^-.

$$2H_2O \longrightarrow O_2 + 4H^+ + 4\ e^-$$

Cathode reaction

The resulting H^+ passes through the membrane to the cathode compartment in order to form H_2.

$$4H^+ + 4e^- \longrightarrow 2H_2$$

This electrolyser method offers various advantages as compared to conventional alkaline electrolyzers. It provides high faradic efficiencies, high current densities (between 0.6 –10 A cm^{-2}), a small footprint and finally functions with pure water rather than corrosive electrolytes as employed in alkaline electrolyzers. However, this kind of electrolyzers operate at low local pH, which corrodes many catalysts, resulting in a demand on expensive PGMs for functioning.[14,15]

1.4 Limitations and challenges still required to overcome

In order to overcome drawbacks, present in current electrolyzers, two major things need to be achieved:

1. The development of a scalable electrolyser that functions close to neutral pH.
2. For that, the development of a noble metal free catalyst, which can function close to neutral pH and with current densities and durability that can compete with the PGMs based systems discussed above.

1.5 Hydrogenase

Fortunately, Nature has evolved a redox enzyme called hydrogenase which does meet all the above-mentioned criteria in terms of activity. Hydrogenase enzymes are found in all domains of life, including *e.g.* photosynthetic prokaryotes and green algae.[17] The first report on the hydrogenase enzyme was in the 1930s.[18] These enzymes primarily function to balance the redox potential in the organism, and produce H_2 in a reversible manner with high catalytic rates (up to 10^2 to 10^4 moles of H_2 per mole of enzyme per second), with zero overpotential requirements at neutral pH.[17] These properties of hydrogenase clearly meet the two requirements mentioned in previous section **(Section 1.4)**. Therefore, it is important to understand these enzymes in detail.

The intrinsic bias between H_2 oxidation and H_2 production of different hydrogenases is dependent on location (membrane bound or in cytoplasm etc.) and physiological context of the enzyme inside the cell. In general, these biomolecules contain a bimetallic or monometallic active site comprised of Ni and/or Fe in a well-defined pocket inside the enzyme. Based upon the presence of different metal ions in their active sites, hydrogenase enzymes are divided into three distinct categories *i.e.* [NiFe], [FeFe] and [Fe] only.[17] Among them, the [FeFe] hydrogenases generally display higher hydrogen production rates, while [NiFe] and [Fe] only hydrogenase are typically involved in H_2 oxidation.[19] Since this thesis work is focussed on H_2 production, we will limit our discussion to [FeFe] hydrogenase.

1.5.1 [FeFe] hydrogenase

[FeFe] hydrogenase enzymes perform reversible hydrogen evolution with high catalytic rates (TOF ~10^4 s^{-1}) and operate close to the thermodynamic potential.[17]

1.5.1.1 Structural details of [FeFe] hydrogenase

The first crystal structure of [FeFe] hydrogenase was reported by Peters *et al.* in 1998 from *CpI* ([FeFe] hydrogenase I from *Clostridium pasteurianum*).[20] Since then, several other crystal structures have been reported, *i.e. Cr*HydA1(from *Chlamydomonas reinhardtii*)[21] and *Dd*HyDAB (from *Desulfovibrio desulfuricans*)[22] etc. Crystal structure data in combination with bioinformatics and spectroscopy revealed that, despite of a huge structural diversity, all [FeFe] hydrogenases feature the H-domain, which contains the active site, called the "H-cluster" **(Figure 1.2)**.[23,24]

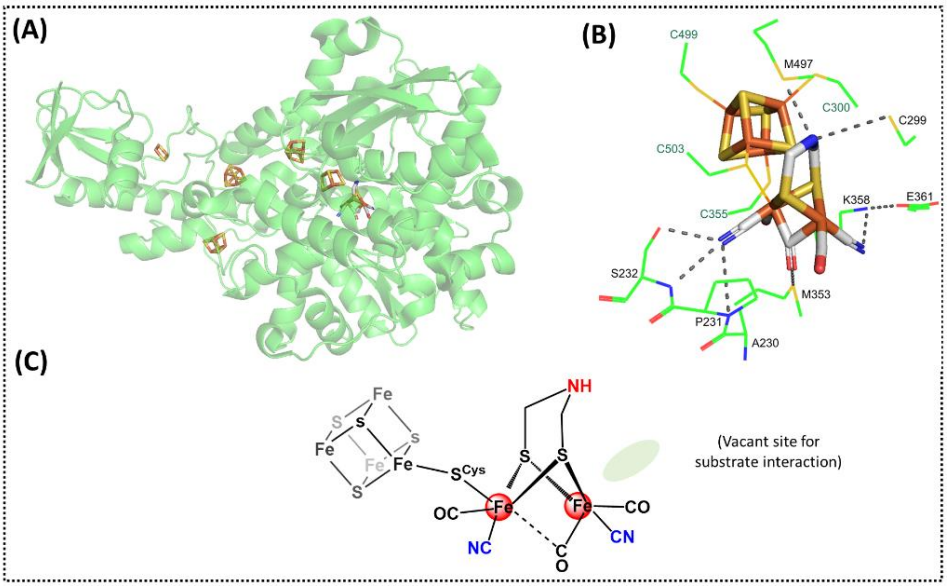

Figure 1.2: (A) Cartoon representation of the X-ray crystallographic structure of [FeFe] hydrogenase *CpI* (PDB: 4XDC, resolution: 1.63 Å) showing the H-cluster and iron-sulfur clusters. The elements represented in sticks are coloured based on the following scheme: Fe = orange, S = yellow, C = grey, N = blue, and O = red. (B) Stick representation of the H-cluster including weak interactions with key amino acid residues (black labels based on *CpI* numbering) and cysteine residues that ligate the $[4Fe\text{-}4S]_H$ cluster (green labels); (C) A Chemdraw representation of the H-cluster.

1.5.1.1.1 H-cluster

The "H-cluster" contains a diiron active site ($[2Fe]_H$) covalently bound to a canonical $[4Fe4S]_H$ cluster via a bridging thiol group of a cysteine residue **(Figure 1.2)**.[20,25] The structure of $[2Fe]_H$ is rather unusual in biology. In the $[2Fe]_H$ active site, the Fe ion which is closest to the $[4Fe4S]_H$ cluster is referred to as the "proximal Fe" (Fe_p), and other one as the "distal Fe" (Fe_d). The Fe ions (Fe_p and Fe_d) of $[2Fe]_H$ are bound to three terminal CO (one could be bridging depending on redox state of the active site) and two terminal CN ligands.[20,25–28] Such strong field ligands stabilise the Fe ions at a low spin mix-valent *i.e.* $Fe_p^{(I)}Fe_d^{(II)}$ state. In addition, Fe_p and Fe_d are bound by a bridging azaditholate ligand (adt^{2-}, $^{-}SCH_2NHCH_2S^{-}$) **(Figure 1.2B,C)**. The latter plays an important role by connecting the proton transport network between the protein and the active site though hydrogen bonding with a nearby cysteine residue (*i.e*. Cys^{299} in *CpI*) **(Figure 1.2B)**.

1.5.1.1.2 Protein matrix around active site

The protein matrix around the active site is important for setting up multiple functionalities essential for stability and the high catalytic rates at low overpotential (*e.g.*, controlling substrate access, providing site isolation, stabilising high energy active states of the H-cluster etc.).[17,20,29–31,32] For example, the amino acid residues present around the $[2Fe]_H$ active site influences the catalytic activity and bias through interactions with the active site as follows: (The position of amino acids is based on *CpI* numbering as shown in **Figure 1.2B**)

Cysteine (299): A cysteine residue interacts with the bridgehead amine of the adt^{2-} ligand of $[2Fe]_H$. This interaction allows to protonate or deproptonate the amine, a key feature during the catalytic cycle **(see Section 1.5.1.3)**.

Proline (P231): A proline backbone interacts with the proximal CN ligand. This interaction has a significant impact on catalytic bias and activity.

Methionine (M353): A methionine residue that has been proposed to play a key role for switching the bridging CO ligand to a terminal position upon reduction of the H-cluster.

Lysine (K358): This amino acid has been proposed to promote the "flip" of Fe_d and give a rotated form, yielding an open coordination site at Fe_d for substrate interactions.

1.5.1.1.3 In vivo maturation process

The "*in vivo* maturation" of [FeFe] hydrogenase, or more specifically, the biosynthesis of the $[2Fe]_H$ cofactor involves three proteins denoted as HydE, -F and -G. Two radical SAM proteins (HydE and G) operate in a collaborative manner to assemble a pre-catalyst on HydF. HydF then transfers the cofactor to the apo-[FeFe] hydrogenase.[33–36] These accessory proteins were first discovered in *Cr* but seem to be conserved in all organisms that contain [FeFe] hydrogenase.[37] In 2013, Berggren *et al.* demonstrated that the $[2Fe]_H$ active site can be synthesised and inserted into HydF, which can then activate the apo-[FeFe] hydrogenase.[28] In the same year, Esselborn *et al.* showed that the synthetic cofactor can be introduced directly into the [FeFe] hydrogenase, circumventing also HydF.[38] Thus, the complicated biosynthesis of the cofactor can be overcome by synthetic chemistry, via a process denoted "artificial maturation".[28,38]

1.5.1.2 Catalytic mechanism

The catalytic cycle of [FeFe] hydrogenase has been intensively studied through a combination of several spectroscopic (FTIR, EPR etc.) and electrochemical techniques by multiple research groups.[39–41] Nevertheless, the exact catalytic mechanism of [FeFe] hydrogenase is still an ongoing debate in the hydrogenase community and several possible reaction intermediates (more than 10 intermediates proposed till today) have been observed during catalysis. This variety of proposed intermediates is based on the observations of different H-cluster states, varying in redox and protonation state, reported by several research groups.[19] I will briefly summarize the catalytic cycle and the key intermediates of what is currently the most commonly discussed model as shown in **Figure 1.3**.[42] The nomenclature of each state is based on the model proposed by Birrell *et al.* [42].

H_{ox} state: This state is also known as the "as prepared" or "active ready" state of the enzyme. The $[2Fe]_H$ active site is in a mixed valent state of $Fe_p^{(I)}$ and $Fe_d^{(II)}$ (the reverse oxidation state assignment, $Fe_p^{(II)}$ and $Fe_d^{(I)}$, has also been proposed) coupled with a with +2 state of the $[4Fe4S]_H$ cluster.[43,44]

Treating **H_{ox}** state with 2 eq. of sodium dithionate (NaDT), a common reduction reagent ($E^{0'}$ = –660 mV *vs.* SHE at pH 7) causes generation of multiple spectroscopic signatures. They are explained by the formation different redox states of the H-cluster as discussed below.

H_{red}: $1e^-$ addition cause reduction of the $[4Fe4S]_H$ cluster and decreases the oxidation state of the $[4Fe4S]_H$ cluster from +2 to +1, while the overall charge of the $[2Fe]_H$ Fe ions remains +3. This state is called the "**H_{red}**" state.[45]

$H_{red}H^+$: Then a chemical event occurs, *i.e.* protonation of the bridgehead amine. This triggers a simultaneous rearrangement of the electron densities shifting $1e^-$ from the $[4Fe4S]_H$ cluster to the $[2Fe]_H$ active site, to give an overall charge of +2 for both the $[4Fe4S]_H$ cluster and the $[2Fe]_H$ Fe ions.[44]

$H_{sred}H^+$: Addition of the second e^- again results in reduction of the $[4Fe4S]_H$ cluster to +1, to form the **$H_{sred}H^+$** state.[43,44]

H_{hyd}: At this stage a second chemical event occurs. A proton bound to the bridgehead amine shifts to Fe_d to form a terminal hydride $Fe_d^{(II)}$–H^- and consequently the charge of both Fe ions of the $[2Fe]_H$ site increases to +2, while the $[4Fe4S]_H$ cluster remains at the +1 state.[44,46]

$H_{hyd}H^+$: Then a third chemical event occurs with the addition of another proton at the bridgehead amine to form the **$H_{hyd}H^+$** state. Then a reaction occurs between the $Fe_d^{(II)}$–H^- and a H^+ bound to the bridgehead nitrogen to form H_2. As a result, the redox state of the $[2Fe]_H$ active site return to its resting, or **H_{ox}**, state to complete the catalytic cycle.[47]

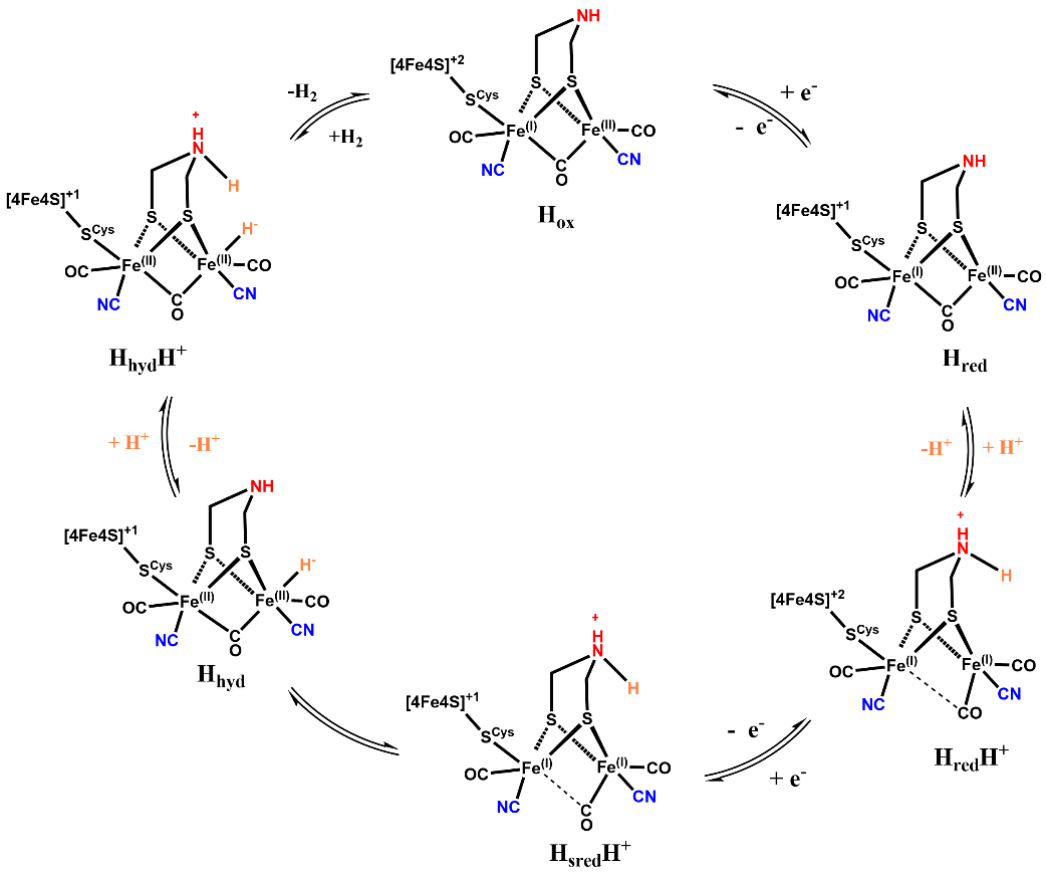

Figure 1.3: Proposed six intermediates model for the catalytic cycle of [FeFe] hydrogenase for H^+/H_2 conversion. The proposed intermediates are explained in **Section 1.5.1.3**. A transient state between **$H_{hyd}H^+$** and **H_{ox}** called **H_{ox}-H_2** was also proposed but has not been observed experimentally (**H_{ox}-H_2** is not shown here).

The spectroscopic support for the aforementioned states was not discussed here, but the interested reader is suggested to follow ref. [19]. It is important to note that the geometries of $\mathbf{H_{red}H^+}$ and $\mathbf{H_{sred}H^+}$ under ambient conditions are an ongoing debate, on the basis of the bridging nature of CO. The catalytic cycle shown in **Figure 1.3** displayed the bridging CO ligand becoming terminal or semi-bridging in the aforementioned reduced states, as suggested from crystallography[48] and infrared spectroscopy[43,44]. However, Ratzloff *et al.* and Birrell *et al.* recently proposed using cryo-FTIR study that both the $\mathbf{H_{red}H^+}$ and $\mathbf{H_{sred}H^+}$ states actually feature a bridging CO ligand.[39,49]

1.5.1.3 Sensitivity of [FeFe] hydrogenase

All [FeFe] hydrogenases characterized to-date are sensitive to O_2, CO and H_2S, resulting in reversible or irreversible enzyme inhibition.

[FeFe] hydrogenases are sensitive towards CO, resulting in reversible or irreversible inhibition depending on the oxidation state of the H-cluster.[50] Interestingly, the sensitivity varies between the different phylogenetic groups (*i.e.* Group A –D) [24] of [FeFe] hydrogenase. For example, putative sensory [FeFe] hydrogenases from Group C and D showed decreased sensitivity towards CO as compared to that from Group A.[51,52] The structural properties of this state has been investigated by X-ray crystallography, D*ensity-functional theory (DFT)* as well as *e.g*. EPR and FTIR spectroscopy. There is consensus on the binding of one additional (*i.e.* fourth) CO ligand in this state, but its exact position on the distal Fe ion is still debated.

[FeFe] hydrogenases are also sensitive to O_2 and irreversibly inactivate within seconds under atmospheric O_2.[53–56] The exact degradation route induced by O_2 is still under debate, but most probably, O_2 takes one electron from $[2Fe]_H$ side to form superoxide ($O2^{\bullet-}$) which is more reactive than neutral O_2. $O_2^{\bullet-}$ then attacks the $[4Fe4S]_H$ cluster and destroy the e^- transfer network.[57,58] However, recently the [FeFe] hydrogenase from *Clostridium beijerinckii* (CbA5H) was shown to display significantly improved resistance against O_2, and X-ray crystallography revealed that a nearby thiol group from cysteine serve as a safety cap against O_2.[59,60]

Hydrogen sulphide (H_2S) is also a reversible inhibitor of many [FeFe] hydrogenases. It has been shown that treating the enzyme with sulphide under oxidizing conditions cause hydrogen sulphide binding to the distal Fe ion, to yield an inactive state. Importantly, this form of the H-cluster is protected from O_2, and can be reactivated under reducing conditions.[53] This insight is important as H_2S treatment can be a potential solution for protecting the enzyme against O_2.

1.5.2 Applications of [FeFe] hydrogenase

1.5.2.1 Biohybrid device

Recent advancement in the bio-catalysis field,[61,62] allowed these impressive biomolecules to be studied extensively on electrode surfaces.[63–65] Several strategies have been employed including protecting redox polymers[66–68], optimized surface orientation[63], electrode nano-structuration etc.[69] Thus, research is progressing rapidly towards the development of [FeFe] hydrogenase based biohybrid devices.[63,64,69]

1.5.2.2 A blueprint for synthetic catalyst design

Due to their excellent catalytic properties [FeFe] hydrogenases have also been used as a blueprint to develop bioinspired catalyst for the last few decades in parallel.[19,70–75] Modifying specific sections of the protein scaffold or cofactor and analysing the resulting changes in activity, durability and/or sensitivity, is a powerful tool for understanding the exact chemistry that occurs inside of [FeFe] hydrogenase. For example, varying particular amino acids (through site-directed mutagenesis) and analysing the impact has yielded some fascinating results, *e.g.* determination of the proton transfer channel and the importance of the secondary coordination sphere **(**discussed in **Section 1.5.1.1**). Similar studies modifying selected components (ligands or metal ions) of the $[2Fe]_H$ active site could also allow to identify the crucial parts of the active site. Subsequently, the overall insights obtained from these studies could then be translated directly into the design of molecular catalysts.

Before moving to bioinspired catalysts, I wanted to briefly discuss “semisynthetic hydrogenases”. The idea is to provide a glimpse of how studies of semisynthetic hydrogenases give insights towards molecular catalyst design.

1.6 Semisynthetic hydrogenase

“Semisynthetic hydrogenase” can be defined as a hybrid hydrogenase enzyme, generated by introducing non-native cofactors inside the apo-enzyme.

As discussed in **Section 1.5.1.2**, *in vivo* maturation of [FeFe] hydrogenase proceeds through a complicated biosynthetic route, therefore modifications of $[2Fe]_H$ are difficult to execute. However, artificial maturation enables the apo-[FeFe] hydrogenase to become activated *in vitro*, using the synthetic $[2Fe]_H$ mimic $[Fe_2(\mu\text{-adt})(CO)_4(CN)_2]^{2-}$ following an hour of incubation at room temperature under inert condition. The resulting semi-synthetic holo-enzyme behaves exactly like wild type and retains 100% native activity.[28,38] The latter finding was remarkable as it opened the door for modifications of the $[2Fe]_H$ by varying the ligands or metal ions, and elucidating the importance of each part of $[2Fe]_H$. For example, in 2015, Lubitz *et al.* reported a series of semisynthetic hydrogenases replacing the CN and bridging (adt^{2-}) ligands of $[2Fe]_H$.[76] The authors concluded that the bridging adt^{2-} ligand is untouchable as modifying it caused more than 99% loss of residual activity. The authors also showed that replacing one CN (as accomplished with $[Fe_2(\mu\text{-adt})(CO)_5(CN)]^{1-}$, a mono-cyanide variant of the active site) generated a semi-synthetic hydrogenase displaying ~60% residual activity. We showed recently that this mono-cyanide variant of [FeFe] hydrogenase also displayed an improved O_2 and CO tolerance as compared to the native $[2Fe]_H$ site (see **Chapter 7**).[77] Kertess *et al.* showed that replacing the sulphur in the bridging adt^{2-} ligand of $[2Fe]_H$ with selenium results in ~1.3 fold increased activity, but the selenide variant is unstable even at -80^0 C conditions.[78] Sommer *et al.* reported a metal exchange study where the Fe ions of $[2Fe]_H$ were replaced with Ru, causing complete loss of activity.[79]

Thus, site directed mutagenesis and semisynthetic hydrogenase studies have revealed a number of key points including:

(i) The secondary coordination sphere created by the protein scaffold is crucial for activity.
(ii) The presence of a basic functionality close to the substrate binding site (like the pendant amine present in the adt^{2-} ligand of $[2Fe]_H$) is important.
(iii) Replacing one CN ligand is not critical for activity, but can reduce the sensitivity of the enzyme towards inhibitors like CO, O_2 as compared to the native enzymes.

1.7 Bioinspired family

Thus, [FeFe] hydrogenases not only could be used as catalysts, but have also served as an ideal blueprint for developing bioinspired catalyst for both the hydrogen evolution and oxidation reaction.[80–85] There are numerous examples of bioinspired catalyst based on Fe[19,86], Co[87,88], Ni[89] and Mo[90] reported for H_2 production till today. Therefore, it is a difficult task to cover all of them in detail within the scope of this thesis. Here we are thus only going to discuss selected bioinspired diiron catalysts, reported to be functional under aqueous condition for H_2 production.

1.7.1 Bioinspired diiron catalysts

Among diiron based bioinspired H_2 evolution catalysts, $\{Fe_2(\mu\text{-}S_2)(CO)_6\}$ based derivatives have been extensively studied during the past few decades.[19,86] In general both Fe ions are in a low spin +I oxidation state and the overall diiron core is diamagnetic, and the sulphur ligands commonly bridged by an alkyl or aromatic linker. More than 1500 catalysts have been reported till today based on the aforementioned diiron core, including:

(i) Modifications of the primary coordination sphere (*i.e.* CO and S) by replacing CO with different types of monodentate and bidentate ligands *i.e.* phosphine, CN etc. A number of studies were also reported replacing the sulphur with other chalcogens like selenium.

(ii) Metal exchange by replacing Fe with other metals like Mo and Ru, Os.

(iii) Introduction, or modification, of at the secondary coordination sphere by modifying the S-S linkage through different types of substitutions at the bridging position. For example, adt^{2-}, ethanedithiolate ($^{-}S(CH_2)_2S^{-}$, edt^{2-}), benzenedithiolate ($^{-}SC_6H_4S^{-}$, bdt^{2-}), propanedithiolate ($^{-}S(CH_2)_3S^{-}$, pdt^{2-}), oxadithiolate ($^{-}SCH_2OCH_2S^{-}$, odt^{2-}) etc.

Though a detailed discussion covering the aforementioned strategies is beyond the scope of this thesis, the interested reader is suggested to follow these references [19,91]. As mentioned above, I will only discuss {$Fe_2(\mu\text{-}S_2)(CO)_6$}based catalysts that were reported to be functional under aqueous conditions.

The majority of {$Fe_2(\mu\text{-}S_2)(CO)_6$}based catalysts are functional mainly under homogenous organic electrochemical and photochemical conditions due to their poor water solubility.[91] Several strategies have been employed to allow diiron catalysts to function in water, of particular relevance to my work is *e.g.* (i) their encapsulation inside water soluble scaffolds (*i.e.* polymers, small peptides, protein scaffolds); (ii) the immobilisation of the catalyst on conductive surfaces. Here, I will give a brief overview of these two approaches.

1.7.1.1 Bioinspired diiron complexes encapsulated inside water soluble scaffolds

One strategy to enable the diiron catalysts to function in aqueous media, is to encapsulate the active site inside water-soluble scaffold. The scaffold could be polymers[92], small peptides[93] or a protein scaffold[94]. I will discuss only the polymer one here as it is the most relevant to this thesis. For an overview on encapsulation inside biological supports (small peptides or protein scaffolds), see for example refs [93–95].

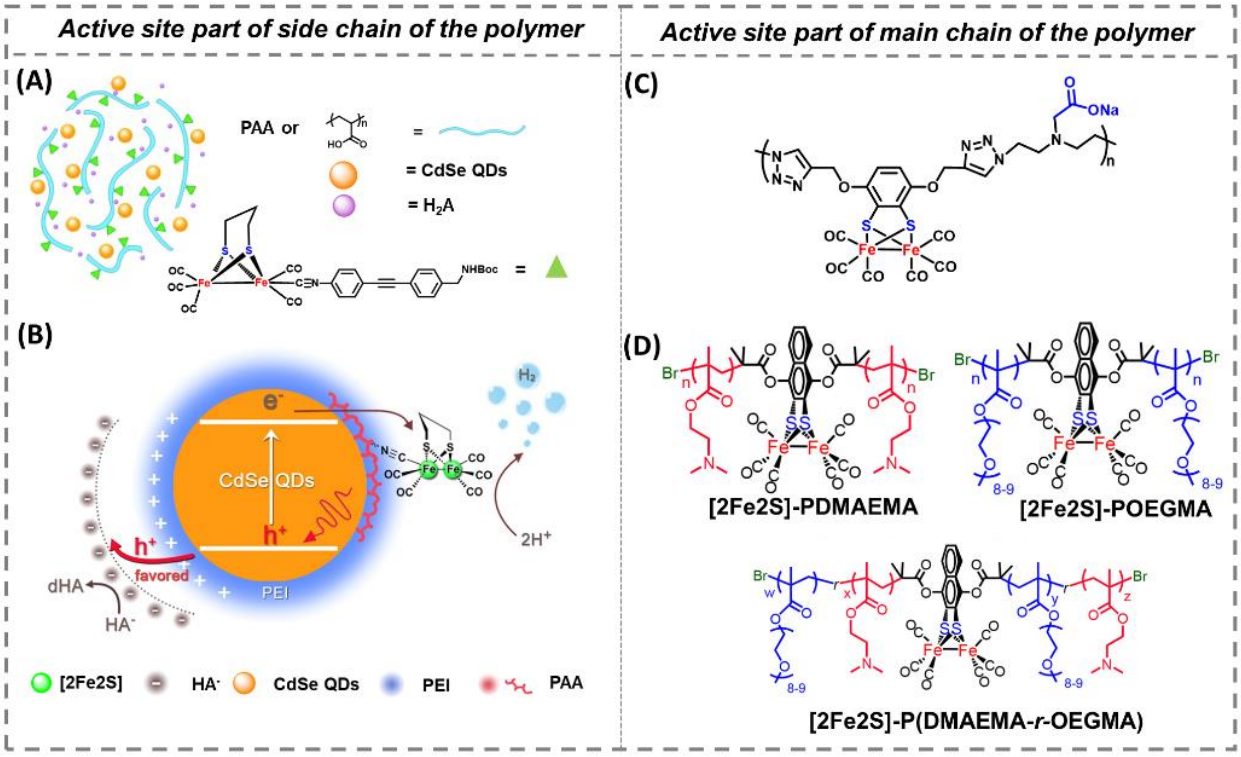

Figure 1.4: Schematic representation of previously reported {$Fe_2(\mu\text{-}S_2)(CO)_6$} based metallopolymers functional under aqueous conditions. The metallopolymers showed in (A) and (B) were reported to be functional under photocatalytic condition, and those showed in (C) and (D) were reported to be functional under electrocatalytic condition in aqueous media. PAA = polyacrylic acid, QDs = quantum dots, H_2A = ascorbic acid, PDMAEMA = poly(2-dimethylamino) ethyl methacrylate, POEGMA = poly(oligo(ethylene glycol) methacrylate). [2Fe2S] = diiron active site. Figures are adopted or reproduced from references [96–99] with permission from American Chemical Society, Springer Nature and WILEY-VCH Verlag GmbH.

The encapsulation strategy involves either embedding the active sites inside pre-made polymeric matrices or including the active site in the polymerisation reaction, resulting in the diiron site becoming part of the side chain or main chain of the polymer respectively.

1.7.1.1.1 Diiron complexes as a part of the side chain of the metallopolymer

Several research group, *i.e.* Picket *et al.*[100], Darensbourg *et al.* [101] and Liu *et al.*[102] reported the encapsulation of diiron sites inside various polymeric matrices *i.e*. poly-pyrrole, polystyrene and polyvinyl chloride (PVC). However, these systems suffered from rapid loss of activity either by degradation or loss of film from the electrode in organic media. Wu *et al.* showed a substantial improvement in the activity by incorporating a $\{Fe_2(\mu\text{-}S_2)(CO)_6\}$ derivative featuring an alkyl bridgehead inside a commercially available poly acrylic acid (PAA), and the assembly showed a turnover number for H_2 production (TON_{H2}) of ~27000 within 8 hours under photocatalytic condition in weakly acidic aqueous media (pH 4) **(Figure 1.4A)**.[96] The authors attributed this exceptional activity to the polymeric scaffold. More specifically, they argued that the negatively charged PAA creates a secondary coordination sphere around active site, stabilised the used CdSe quantum dots (QDs) and ensured a short distance between the catalyst and the QDs for better electron communication. However, the authors still reported a degradation of activity through homo association due to excess loading of catalyst in PAA. Later, the same group reported an improvement of their previously mentioned metallopolymers, combining both polyethyleneimine (PEI) and PAA as monomers and encapsulating the same diiron site as reported before.[96] The resulting assembly reached a TON_{H2} of 83,600 within 28 hours at pH 4.1, a record activity for [FeFe] hydrogenase mimics at that time **(Figure 1.4B)**.[97] These reports clearly demonstrates the possibility of improving catalysts with regards to activity and durability through encapsulation.

1.7.1.1.2 Diiron complex as a part of the main chain of the metallopolymer

Parallel efforts have also been made with the idea of metallopolymerisation using the catalyst, or active site, as part of the polymerisation, instead of encapsulating catalysts inside a premade polymeric bed. Here the diiron complex can be included as either a monomer or metal initiator. Several research groups reported metallopolymers based on this strategy using different free radical polymerisation reactions.[92] I will discuss a few of them here.

In 2010, Liu *et al*. first reported two alkenyl bridged $\{Fe_2(\mu\text{-}S_2)(CO)_6\}$ derivatives, incorporated inside polyene type polymers.[103,104] The polymers were subsequently immobilized on gold electrodes for electrochemical activity assessment, and the authors concluded that a suitable macromolecular scaffold can reduce the overpotential requirements significantly as compared to isolated small diiron hydrogenase mimics (up to 400 mV) and slow down the decomposition of catalytic sites.[103,104] However, the aforementioned metallopolymers were insoluble in water and their electrochemical responses were depleted after repetitive potential cycles. Later, the same group reported a metallopolymer containing a $\{Fe_2(\mu\text{-bdt})(CO)_6\}$based complex with carboxylate groups (COO^-) present at the side chain of the polymer.[98] The resulting metallopolymer provided both water solubility as well as better catalytic efficiency under both homogenous and heterogenous electrochemical conditions as compared to the previously mentioned systems (**Figure 1.4C**).[103,104] In 2019, Pyun *et al.* reported diiron sites with a napthaquinol bridged $\{Fe_2(\mu\text{-}S_2)(CO)_6\}$ active site, covalently encapsulated inside water soluble polymeric scaffolds prepared using an Atomic transfer radical polymerisation (ATRP) method.[99,105] To be specific, the authors reported a series of metallopolymers containing various functional groups like $-N(CH_3)_2$ (for "PDMAEMA" or poly(2-dimethylamino) ethyl methacrylate) or $-O(CH_2)O-$ (for "POEGMA" or poly(oligo(ethylene glycol) methacrylate) to generate different secondary coordination spheres around the active site **(Figure 1.4D)**. The authors demonstrated the importance of the composition of the polymer, as the polymer containing only $-N(CH_3)_2$ groups (abbreviated PDMAEMA) significantly outperformed the others. The latter system showed high catalytic rate (turnover frequency for hydrogen production, TOF_{H2} of 250,000 s^{-1}) with an onset potential of 0.23 V in 1 M Tris buffer at pH 7 in the presence of oxygen, under homogenous conditions. These remarkable properties were attributed to the highly basic tertiary amine peripheral groups ($-N(CH_3)_2$) which get protonated to a large extent (~ 90% at the studied pH 7.0), the authors further argued that the buffered medium avoid formation of reactive oxygenic species (ROS).[99,105]

1.7.1.2 Bioinspired diiron complexes immobilized on electrode

Apart from water insolubility, the majority of catalysts in the $Fe_2(\mu\text{-}S_2)(CO)_6$} family suffer from (i) poor diffusion rates[91]; and (ii) degradation via homo-association under homogenous condition[106–108], (iii) large overpotential requirements (*i.e.* poorly tuned electron density)[91] (iv) formation of bridging hydride during catalysis which was reported to be less active than terminal hydride[109] (v) oxygen sensitivity under catalytic condition[110]. These drawbacks resulted in poor activity (low TOF_{H2}) and substandard durability. Immobilisation of catalysts on electrode surfaces offers to address some of the aforementioned limitations, for example:

1. It offers a path around many of the limitations (diffusion, degradation, recyclability etc.), present under homogeneous condition.
2. It allows studies in aqueous media even for water insoluble catalysts (see **Chapter 4)**.
3. It can improve the electronic communication between the electrode and catalysts relative to homogenous conditions (see **Chapter 5**).
4. Finally, the immobilisation of catalysts is required in order to shift from basic science to real world applications (like devices).[87,111–113]

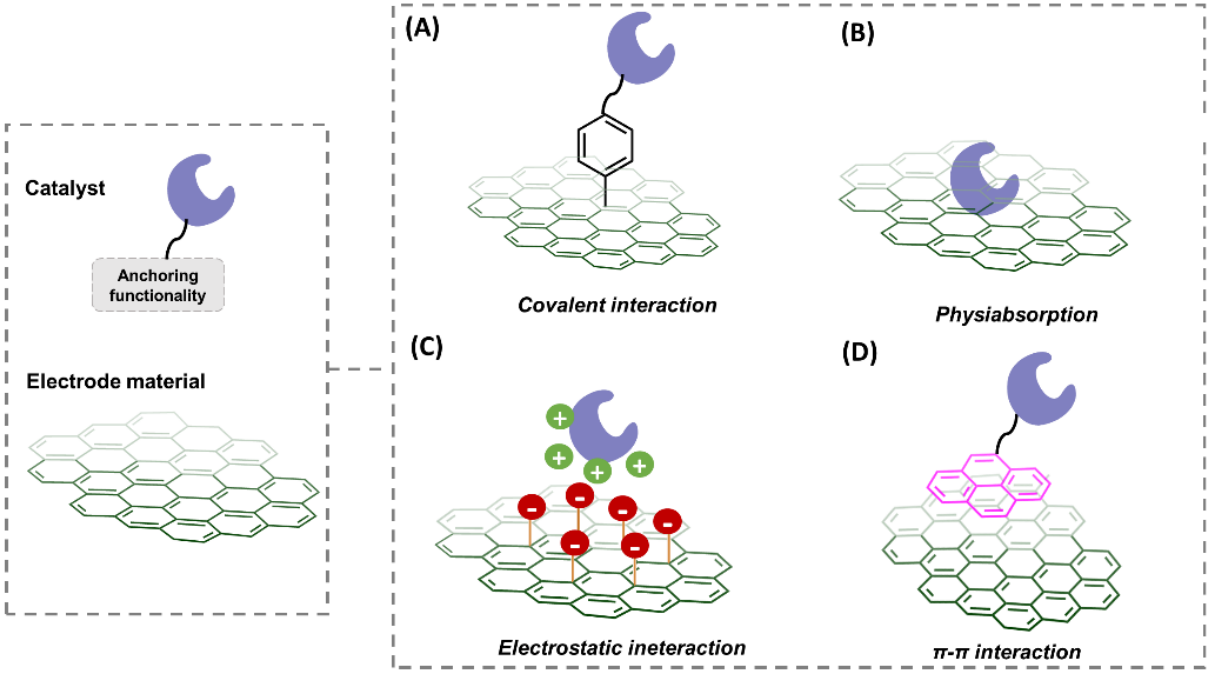

Figure 1.5: Different anchoring strategies used for grafting of molecular catalysts on electrode materials using (A) covalent interaction; (B) physisorption; (c) electrostatic interaction and; (D) π-π interaction.

The anchoring of catalysts on electrode surface could be successfully obtained using four types of interactions between the catalyst and electrode, *i.e.* (a) covalent binding, using *e.g.* click chemistry[103,114] or the diazonium ion reaction[112]; (b) physisorption[115]; (c) electrostatic interactions[116] ; (d) π-π interactions using functional groups present in the catalyst, like pyrene[117] **(Figure 1.5)**. Among them, catalysts from the $Fe_2(\mu\text{-}S_2)(CO)_6$} family have been reported to be immobilized on electrodes via covalent binding and physisorption as discussed below.

As compared to homogeneous studies, there are very few reports on $Fe_2(\mu\text{-}S_2)(CO)_6$} based systems studied under heterogeneous conditions. Between 2005–13, Talarmin *et al.*[118] and Darensbourg *et al.*[119] reported covalent grafting of $Fe_2(\mu\text{-}S_2)(CO)_6$} based complexes using amide linkage between such diiron complexes and functionalized carbon based electrodes. The authors revealed that this anchoring was unstable under electrocatalytic reduction conditions due to lability of the amide linkage, and consequently no catalytic current was observed under neither organic nor aqueous conditions. Fontecave *et al.* reinvestigated the amide linkage strategy between $Fe_2(\mu\text{-}S_2)(CO)_6$} based catalysts and carbon or gold electrodes. Here the authors reported that electrocatalytic wave was unstable due to elimination of CO ligands rather than hydrolysis of the amide linkage.[120] Picket *et al.*[100] and Liu *et al.*[102,121,122] reported covalent grafting

of various diiron carbonyl complexes on polymer functionalized platinum, gold and multi-walled carbon nanotube (MWNT) electrodes, and some of them were found to have remarkable stability under acidic aqueous conditions. Between 2013–22, Dey *et al.* reported some fascinating insights on the heterogenous activity of $\{Fe_2(\mu\text{-}SCH_2N(R)CH_2S\text{-})(CO)_6\}$ (R= aromatic substituents) functionalized electrodes under aqueous conditions. His team published several studies, in which such diiron complexes were immobilized on graphite based electrodes using physisorption[115,123,124] as well as through covalent bonding[114], and showed excellent electrochemical hydrogen evolution properties (TON_{H2}~10^8) under acidic aqueous condition, as well as oxygen tolerance[123] and bidirectionality (*i.e.* capacity for both H_2 production and oxidation)[124]. Lu *et al.* also recently reported covalent attachment of $\{Fe_2(\mu\text{-}SCH_2N(R)CH_2S)(CO)_6\}$ based catalysts on single walled carbon nanotubes as well.[125]

Among the previously reported grafting strategies discussed so far, immobilization relying on nonspecific physisorption often results in poor electron transfer rates combined with limited stability of the anchoring over long term electrolysis,[126] while covalent coupling typically leads to lower surface loadings (maximum ~0.24 nmol cm^{-2}),[114,118] and inhomogeneous catalyst distribution.[116] We recently showed that catalytic loading could be improved substantially (~9.5 nmol cm^{-2}) using π-π interactions between a designed $\{Fe_2(\mu\text{-}S_2)(CO)_6\}$ derivative containing pyrene rings and MWNT (See **Chapter 4** for details).[127]

1.7.2 Other metal containing catalysts

As mentioned above, there are equally extensive studies related to proton reduction catalysis going on in parallel to the "diiron chemistry", based on Ni, Co.[19,70–75,87] I will not discuss them here. Still, I have to mention one catalyst among them *i.e.* the Ni based catalyst called the "Dubois catalysts" or $[Ni^{(II)}(P_2^RN_2^{R'})_2]$ (R, R´= aromatic, aliphatic substituents).[128] This Ni based catalyst showed bidirectionality for H^+/H_2 conversion, with very low overpotential requirements and excellent catalytic rates (TOF_{H2} ~10^6 s^{-1}).[129] Recently, it was reported that this exceptional catalyst could reach striking current densities of 214 ± 20 mA cm^{-2} at 0.4 V overpotential for H_2 oxidation while immobilized on multiwalled carbon nanotubes (MWNT).[117]

1.8 Life Cycle Assessment

While the development of efficient, up-scalable catalysts and device is one of the primary steps to develop H_2 based economy, the environmental footprint of the proposed systems constitutes crucial practical aspect in parallel. Hence, an environmental evaluation to elucidate the sustainable performance of the proposed system is more than recommendable. Latter study will allow to identify main hotspots that cause highest environmental impact and permit to remodel the system by replacing the culprit with a relatively fewer demanding materials processes. In that sense, the Life Cycle Assessment (LCA) has been recognized as the most distinguished methodology to understand and quantify this environmental profiling.

1.8.1 Basic introduction to LCA

LCA is a methodology for assessing environmental impacts associated with all the stages of the life cycle (from cradle to grave) of a product, process, or service.[130,131] For instance, in the case of a manufactured product, environmental impacts are assessed from raw material extraction and processing (cradle), through the product's manufacture, distribution and use, to the recycling or final disposal of the materials composing it (grave).

According to the standard protocol mentioned in ISO 14040:2006 and ISO 14044:2006, LCA should be performed using mainly four steps as discussed below **(Scheme 1.1)**.

(i) Goal and Scope
(ii) Life cycle Invitatory
(iii) Life Cycle Impact
(iv) Interpretation

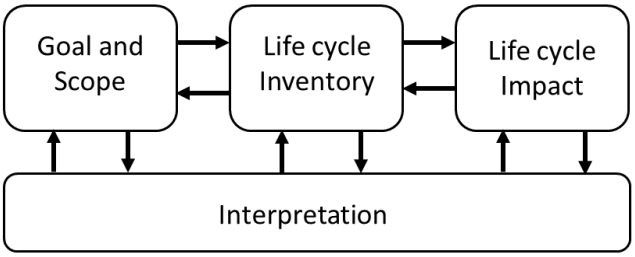

Scheme 1.1: Stepwise methodology of performing LCA of system, process or materials.

(i) Goal and scope

It is the first step of a LCA.[132] As explained in ISO 14040:2006 and ISO 14044:2006 , 'Goal and scope' can be defined as the objective and span of the analysis that has to be covered during the LCA, respectively. It outlines the depth of the study before the assessments initiate. It covers intended applications or results, limitations due to methods or assumptions during analysis and specify the targeted audience with whom the study will be primarily shared.

The scope of the research draws the boundary within which analysis should be carried out. Based on that, scope of the LCA study is subdivided into two parts.

System boundary

System boundary can be interpreted as the boundary within which the environmental impacts of the product or the system, are going to be evaluated. System boundaries is partly based on a subjective choice, made before analysis begins according to the objectives of the analysis.[133] Generally, it entails the processes that should be considered for the analysis. The processes include starting from extraction of raw materials, resources from nature to manufacture the product till the end of its life cycle with the waste management and recyclability (*i.e.* "cradle to grave").

Functional unit

Functional unit can be defined as the 'product or system' whose impact is going to be evaluated through LCA (for example, 1 kg of H_2 in our case). It provides a reference or parameter through which the inputs and outputs can be related and comparison between different systems or products could be accomplished. In a quantitative and qualitative way, results have to be referred to it.

(ii) Life cycle inventory (LCI)

LCI is a straight-forward step to prepare a repository of data which accounts all input and output flows of the product/service/system under study. It includes chemicals, energy consumed, waste generated during the process and all necessary materials and energy flows considered. This process attests the completeness and validity of the information for a particular process.

(iii) Life cycle impact

As discussed in ISO 14044:2006, life cycle impact defines the consequences on environment due to the analysed product or system. The impacts were assessed on selected impact categories. The choice of the categories should be comprehensive in a sense that it should cover all the environmental issues (*i.e.* air, water, soil and human health etc) related to the analysed product or system. The choice of category should be technically and scientifically valid. The selection of impact categories should be defined prior to the inventory analysis to ensure that all relevant data are collected for selected categories. In our case, Life cycle impact was assessed based on selected environmental categories as per the "RECIPE 2016 Midpoint (H) method"[134]. Impact categories selected to discuss the results in this thesis are explained in **Table 1.1**.

Table 1.1: The summary of the impact categories used in this thesis under "RECIPE 2016 Midpoint (H)" methods and their respective explanation and units. This table in adopted from ref. [135] or **Paper II**.

	Impact category	Description	Units
1	Global warming	Climate change due to greenhouse gas emission	kg CO_2 eq.
2	Terrestrial acidification	Release of inorganic acid in water	kg SO_2 eq.
3	Freshwater eutrophication	Accumulation of nutrients in water that overstimulate plant growth but reduces the level of O_2	kg P eq.
4	Terrestrial ecotoxicity	Hazard substances used in industry which are toxic for ecosystem	kg NO_x eq.
5	Human carcinogenic toxicity		kg 1,4-DB eq.
6	Mineral resource scarcity	Minerals and natural substances that produced via geological processes	kg Cu eq.
7	Fossil resource scarcity	Depletion of resources that contains hydrocarbon (methane, coal etc.)	kg oil eq.

DB = 1,4 dichlorobenzene; Kg P eq. = common unit of eutrophication effects.

(iv) Interpretation

Finally, the life cycle inventory aggregates all input (*i.e.* materials, energy, waster etc.) which allows to evaluate the impact in each selected impact categories with respect to the overall goal, scope of the analysis and yield the results of LCA. Interpretation could be showcased in two ways mainly. Firstly, impact of any individual system or material could be assessed in each category. Secondly, multiple systems (for example, different catalysts for H_2 production) could be compared in each category. As mentioned the analysis or comparison should always be accomplished using a pre-determined functional unit (*i.e.* 1 kg of H_2 production).

1.8.2 Advantage of LCA

LCA advantages some of the key aspects as followed,

(i) It encompasses a panoramic view about the environmental footprint of a product under multiple impact categories within the scope of analysis.
(ii) It allows to improve the environmental impact of a product by identifying the exact process or materials that contributes higher about a specified environmental concern and allow to optimize it with the view to mitigate the consequent negative effect.
(iii) It provides a crucial merit by having environmental profile of the product which is beneficial during marketing to authorized bodies (Government, Industry etc.).

1.9 Summary

The bioinspired catalyst family, discussed so far showed activities considerably lower than that of enzymes. In fact, only a few catalysts among them are reported to show substantial activity.[99,105,117] Therefore, improved catalyst design is still required.

Here, I summarize some of the key points to be considered in the design of diiron based catalyst, as these are a main component of the thesis:

(i) A durable catalyst: bioinspired diiron sites often decompose under catalytic condition (see **Section 1.7.1**). Therefore, a robust diiron core is compulsory.

(ii) A secondary coordination sphere: In addition, the catalyst should contain a proper secondary coordination sphere (*i.e.* basic or acidic periphery close to active site) for promoting the activity.[81]

(iii) Promotion of terminal hydride: The design of active site should be in a possible way that can promote terminal hydride which is more active than bridging hydride intermediate formed usually in $\{Fe_2(\mu\text{-}S_2)(CO)_6\}$ derivatives during catalysis. It could be obtained either by designing terminal [109,136] or bridging ligand[124].

(iv) Tuning of electron density: To balance between high electron density (*i.e.* difficult to reduce) at metal center and fast protonation, non-innocent ligand(s) should be part of the catalyst. Latter could allow to optimize the electron density at catalyst site during catalysis.[137]

(v) Immobilization on electrodes: Immobilization of catalyst will also allow to avoid limitations present under homogenous condition and use the catalyst in bioinspired devices for energy conversion (see **Section 1.7.1.2)**.[138]

Considering these guidelines, the metallopolymer approach could be an excellent choice, as latter allows to include multiple functionalities (secondary coordination sphere, anchoring group etc.) in a single platform (see **Section 1.7.1.1**).[92]

Chapter 2 : Overall goal of the project

2.1 eSCALED project and overall goal

As discussed in **Section 1.1** and **1.2**, producing fuels using solar electrolysis is a promising step towards reducing GHGs emissions and their detrimental consequences.[4,139] The eSCALED project accepted the challenge to develop a device (called "artificial leaf") to produce H_2 or a reduced CO_2 products using solar electrolysis **(Figure 2.1)**. The device works on the same principle as the leaf *i.e.* uses sunlight, water and CO_2, but generates a small "molecular energy carrier" (like H_2, CH_3OH, C_2H_5OH) instead of carbohydrates. The requirements setup in the project were that the device should be cheap or noble metal free, scalable and sustainable. Moreover, it should display significant activities and remain durable under catalytic condition. Finally, it should operate under aqueous condition at close to neutral pH.

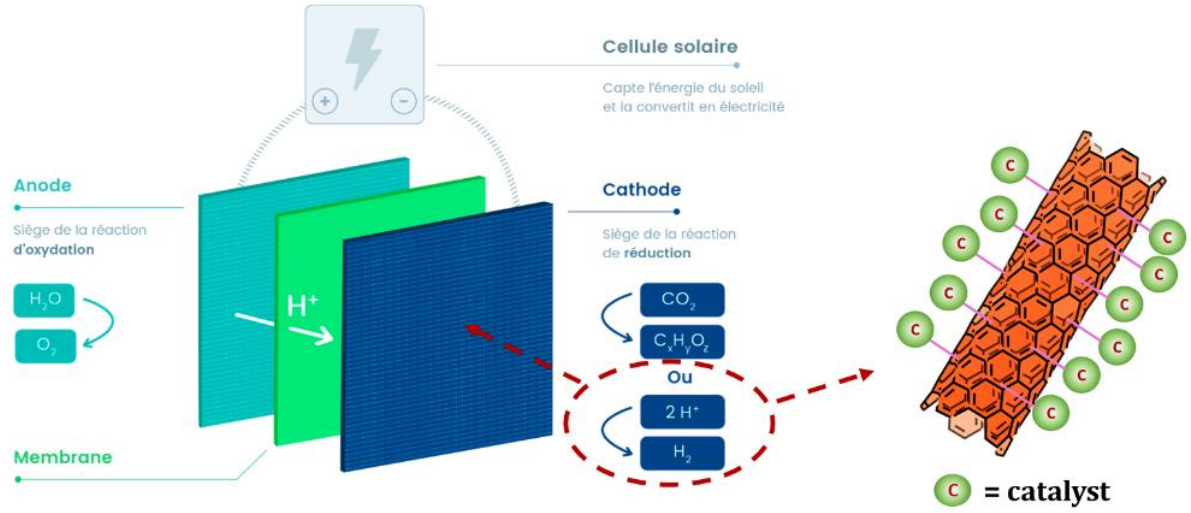

Figure 2.1: Schematic representation of the envisioned eSCALED device for producing H_2 and reduced CO_2-based chemicals using solar electrolysis and the proposed cathode materials for H_2 production. Copyright eSCALED project.

In principle, this kind of device comprises two compartments (cathode and anode) where the overall reactions (*i.e.* H^+ reduction or CO_2 reduction driven by solar electrolysis) takes place, separated by a membrane. Each compartment requires a catalyst for the respective half-cell reaction (*i.e.* anode for water oxidation and cathode for H^+ or CO_2 reduction).[140]

<u>Anode reaction</u>

The water is oxidized at the anode to produce O_2, H^+ and e^-.

$$2H_2O \longrightarrow O_2 + 4H^+ + 4\ e^-$$

<u>Cathode reaction</u>

The resulting H^+ passes through the membrane to the cathode compartment in order to form H_2 or CO_2 reduction-based products.

$$4H^+ + 4e^- \longrightarrow 2H_2$$

or,

$$CO_2 + nH^+ ne^- \longrightarrow CO, CH_3OH, HCOO^- \text{ etc.} \quad n= 2,4,6 \text{ etc.}$$

The catalyst should be immobilized on an electrode surface to enable device implementation. To complete the above-mentioned objectives, 14 early stage researchers (ESRs) from across the globe, were hired and instructed to develop different parts of the proposed device (*i.e.* cathode, anode, photovoltaic cell, membrane etc.) **(Figure 2.1)**.

2.2 Objective of this thesis

My responsibility was to developing cathode materials for H_2 production **(Figure 2.1)**. To be specific, I needed to develop a noble metal free, scalable, sustainable, substantially active and durable molecular catalyst, functioning under aqueous conditions. In addition, the catalyst should be feasibleto immobilize on electrodes. To achieve these goals the points taken under consideration were as followed:

a. *Develop an active and durable catalyst.*

A bioinspired $\{Fe_2(\mu\text{-}S_2)(CO)_6\}$ core was selected as a basic structure for the catalyst. Then a secondary coordination sphere was designed to provide anchoring ability on electrodes, water solubility, and also improving the activity of the catalysts.

b. *Develop an anchoring strategy ensuring long-term stability (stable at least a day with complete retention of activity, a difficult task from a molecular catalyst point of view), high catalyst loading (at least 10 times higher i.e. 10 nmol cm^{-2} than that reported before for diiron catalysts) and good electronic communication between catalyst and electrode.*

Pyrene was selected as an anchoring group due to its capacity to interact strongly with pi-conjugated nanostructured electrodes like MWNT via π–π interactions.

c. *Develop the resulting electrode materials in way that should be possible to use in water.*

The activity and durability of the electrode materials was planned to be assessed using electrochemistry and spectroscopy.

d. *Finally, evaluate the environmental footprint of the H_2 production by electrode materials.*

The environmental impact for H_2 production was planned to be assessed using Life cycle assessment (LCA).

Chapter 3 : Experimental tools, terms used in the thesis work

3.1 Experimental Tools

The experimental tools that we used to characterise the electrode materials in this study are as follows.

3.1.1 For characterisation of the catalyst(s)

a. NMR (^{1}H,^{13}C, DOSY): provides information about the composition, hydrodynamic radius and diffusion coefficient (for metallopolymers) of the catalyst.
b. Mass spectrometry and size exclusion chromatography (SEC): allows to estimate the molecular weight of the catalyst (polymer).
c. EPR spectroscopy: allow to understand the electronic structure of the active site.
d. X-ray crystallography: provides the molecular structure of the crystals, calculate bond lengths, bond angles etc. presents in the molecule.
e. X-ray photoelectronic spectroscopy (XPS): provides information regarding binding energies of the elements and their relative quantities present in the molecule/material.
f. UV-Vis spectroscopy: provides information to understand different metal-ligand and ligand-ligand interactions (intramolecular) based on absorption of light.
g. Fluorescence spectroscopy: provides information of ligand-ligand interactions (intra and intermolecular) based on fluorescence properties present in the molecules.
h. Infrared spectroscopy: provides information using stretching of ligands as proxy to asses' relevant properties of the catalysts. For example, the CO, CN ligands are an excellent probe of the diiron complexes used in this thesis.
i. Cyclic voltammetry (CV): provides information regarding the redox properties and electrocatalytic activities of the catalyst.

3.1.2 For characterisation of catalysts on the electrode surface

a. CV: estimates redox properties, catalytic activity, catalytic loading, *post operando* assessment.
b. Chronoamperometry (CA): to evaluate the durability of the electrode material during catalysis.
c. Gas chromatography (GC): to detect and quantify the product, and determine the efficiency of the catalysis during CA.
d. UV-Vis, Infrared spectroscopy: for *post operando* assessment to understand the fate of the catalyst during/after CA.
e. LCA: to assess the environmental footprint of the product formation by the electrode materials, and to identify the most demanding component(s) in the process.

3.2 Some key terms used throughout the thesis

$\mathbf{i_{p,c}}$ = peak current for reduction event.; $\mathbf{i_{p,a}}$ = peak current for oxidation event; $\mathbf{E_{p,c}}$ **=** potential (E) for $\mathbf{i_{p,c}}$; $\mathbf{E_{p,a}}$ **=** potential (E) for $\mathbf{i_{p,a}}$; $\mathbf{E_{1/2}}$ **=** half wave potential; $\mathbf{\Delta E_p}$ = peak separation between $\mathbf{E_{p,c}}$ and $\mathbf{E_{p,a}}$ or ($\mathbf{E_{p,c} - E_{p,a}}$) ; Q = charge under redox wave **(Figure 3.1)**.

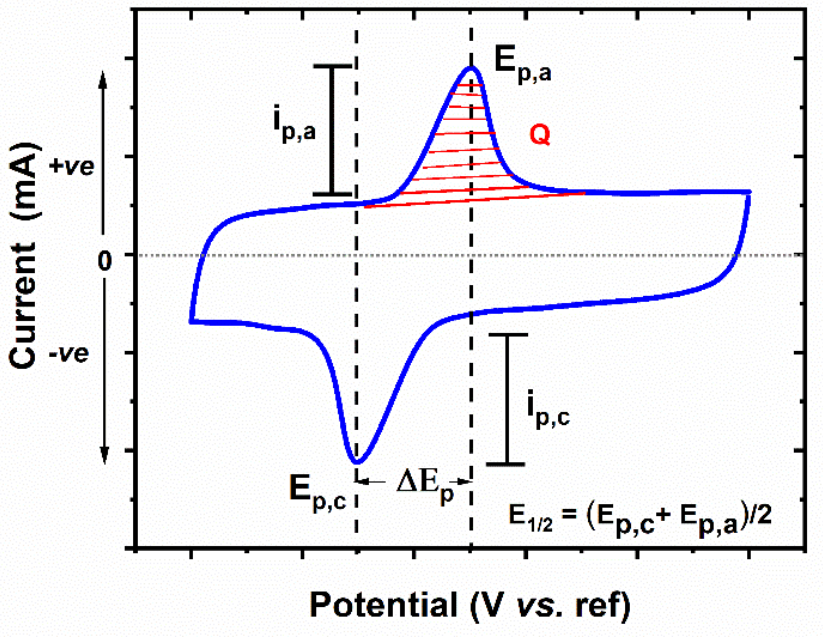

Figure 3.1: Graphic overview of the terms used for CV traces throughout the thesis. ref. = reference (*i.e.* $Fc^{+1/0}$ or RHE).

Other terms that are used in this thesis, can be explained as

Onset potential: Defined here as the potential at which the current trace deviates ~10% relative to the background capacitive current for the catalysis, an estimate of the onset of the catalytic current.

Overpotential: The additional thermodynamic force required (in V) to drive a specific reaction relative to the thermodynamic potential of the chemical reaction (for H_2, it is –0.413 V *vs.* SHE in pH 7 at 1 atm H_2 pressure).

Polydispersity index (PDI): Reflects inhomogeneity based on size or molecular weight of polymers. It is represented by "*Đ"* and calculated as M_w/M_n as shown in the next section. The value of *Đ* is 1 when the polymer is mono disperse or homogenous. Deviations from 1 represents inhomogeneity in the polymer. In practice, a polymer with *Đ* between ~1.2 to 1.5 is considered to have a narrow distribution of molecular weight or size.

Electronic communication: Is used here to describe the feasibility for e- transfer between two materials (*i.e.* electrode and catalysts), primarily with regards to the fraction of immobilized catalysts actually involved in catalysis.

3.3 Key calculations used in this thesis

(i) $D = K_bT/6\pi\eta R_h$

(ii) E (*vs.* RHE) = E (*vs.* Ag/AgCl; 3M KCl) + E_0 (Ag/AgCl; 3M KCl) + 0.059 x pH

(iii) E (*vs.* $Fc^{+1/0}$) = E (*vs.* Ag/AgCl; 3M KCl) **–** E ($Fc^{+1/0}$ *vs.* Ag/AgCl/KCl)

(iv) $\Gamma_{CV} = \frac{Q}{n \times F \times A}$

(v) $n_{H2} = n_{H2}$ (Cat/MWNT) – n_{H2}(bare MWNT)

(vi) $FE_{H2} = \frac{n_{H2} \times 2F}{\Delta Q_{CA}} \times 100$

(vii) $TON_{H2} = \frac{n_{H2}}{\Gamma_{CV} \times A}$

(viii) $PDI = M_w/M_n$

Here, D = diffusion coefficient (in $m^2\ s^{-1}$) obtained from DOSY NMR; K_b = Boltzmann constant (1.38×10^{-23} $J.K^{-1}$) ; η = viscosity of the solvent (in P s, η_{D2O} = 0.00109 P s) ; R_h = hydrodynamic radius; T = temperature (in K); E (V *vs.* RHE) = overpotential requirement of the reaction (in V) ; E (V *vs.* $Fc^{+/0}$) = potential against ferrocene/ferricenium references (in V) ; Γ_{CV} = loading of active

site on electrode (mol cm^{-2}) ; n_{H2}= amount H_2 production during CA (in mol) ; Q = charge under redox peak (in C, see **Figure 2.3)** ; n= number of moles of e^- involved for 1 mol of H_2 production *i.e.* 2 ; A= surface area of the electrode (cm^2); n_{H2} (**Cat**/MWNT) = n_{H2} produced by catalyst (Cat) immobilized on MWNT (mol) ; FE = Faradic efficiency(%); F= faradaic constant *i.e.* 96,485 C mol^{-1}; ΔQ_{CA} = charge consumed during CA (in C) ; TON_{H2} = turnover number for H_2 production; M_w = weight averaged molecular weight; M_n = the number averaged the molecular weight.

Chapter 4 : Paper I – Non-covalent integration of bioinspired [FeFe] complex on multiwalled carbon nanotubes for electrocatalytic H_2 production

4.1 Background and Motivation

In **Section 1.7.1**, $\{Fe_2(\mu\text{-}S_2)(CO)_6\}$ based [FeFe] hydrogenase mimics were introduced.[86] In **Section 1.7.1.2**, the advantages of heterogenous catalysis and a brief overview of immobilisation strategies employed with the $\{Fe_2(\mu\text{-}S_2)(CO)_6\}$catalyst family were discussed. The strategies employed for $\{Fe_2(\mu\text{-}S_2)(CO)_6\}$ derivatives so far are either covalent interactions or physisorption, which yielded either poor loading or weak anchoring strength. However, the immobilisation of $\{Fe_2(\mu\text{-}S_2)(CO)_6\}$ derivatives using π-π interaction was not reported previously.

4.2 Objective

Here, I will summarize my efforts to design and synthesise a $\{(Fe_2(\mu\text{-}S_2)(CO)_6\}$ derivative that includes pyrene functional units. Pyrene could allow to immobilize the catalyst on MWNT via π-π interaction (See **Figure 3.1**). Subsequently, the resulting functionalised electrode material was characterised via spectroscopy and electrochemistry to assess its electrocatalytic H_2 evolution at neutral pH as well as durability under catalytic conditions. The decided target compound was [μ-2,3-(naphthalene-1,4-diylbis(4-(pyren-1-yl) butanoate)-dithiolato]bistricarbonyliron (complex **2**, **Scheme 4.1**).

4.3 Synthesis

The synthetic precursor [μ-2,3-(naphthalene-1,4-diylbis(4-(pyren-1-yl)butanoate)-dithiolato]bistricarbonyliron (complex **1**) was synthesized starting from $Fe(CO)_5$ using a previously reported protocol.[141] Subsequently, complex **1** was reduced and allowed to react with pyrene-1-carboxylic acid succinimidyl ester (or pyrene NHS ester) in THF for 14 hours to yield complex **2** via a nucleophilic substitution reaction **(Scheme 4.1)**.

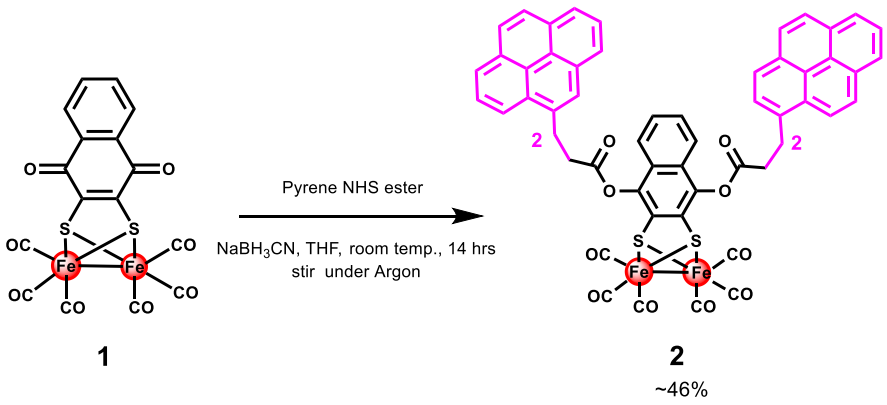

Scheme 4.1: Synthetic scheme for complex **2** from complex **1** and pyrene NHS ester.

4.4 Characterization

The X-ray crystal structure of complex **2** showed the presence of two pyrene rings per di-iron site orthogonal to each other **(Figure 4.1)**. The Fe-Fe, Fe-S, Fe-CO bond distances were similar to those of related $\{Fe_2(\mu\text{-}S_2)(CO)_6\}$ complexes[142] (see CCDC 2183292 in the Cambridge crystallographic database for more details).

^{1}H NMR spectroscopy revealed peaks characteristic of the bridging naphthalene group at 7.5 and 7.37 ppm. Comparing that with complex **1** (8.0 and 7.72 ppm) revealed an upfield shift for complex **2**, attributed to the conversion of the quinone carbonyls into ester functional groups. In addition, the pyrene units present in **2** showed peaks between 8.16 – 7.92 ppm (see ref.[127] or **Paper I** for more details). The presence of pyrene in complex **2** was also evident in the UV-Vis spectra, showing multiple signature peaks between 255 and 350 nm (see ref.[127] or **Paper I** for more details).

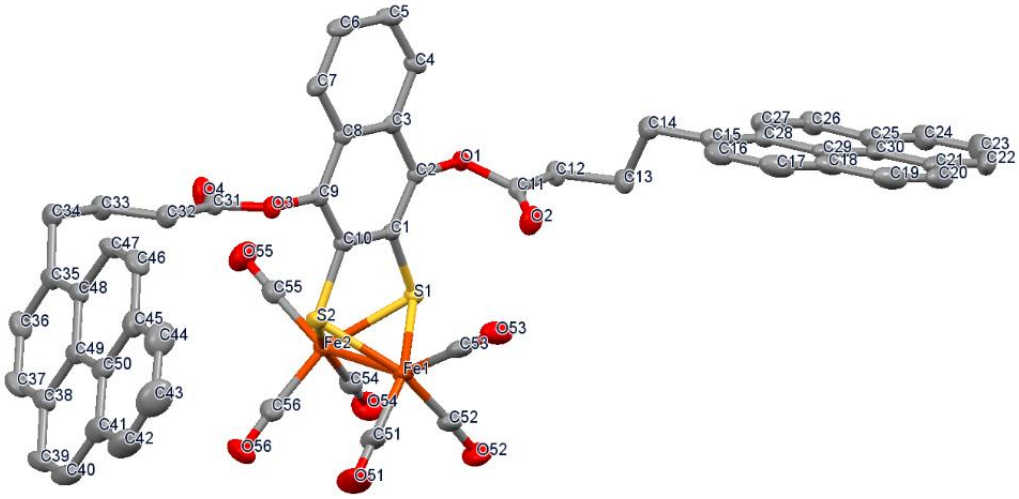

Figure 4.1: X-ray crystal structure of complex 2. Colour coding: Fe orange; S yellow; C grey; and O red. Hydrogen atoms are omitted for clarity. Thermal ellipsoids were set at 50% probability level. Selected bond distance (Å) and angles (0): Fe1–Fe2, 2.4802(5); Fe1–S1, 2.2598(8); Fe1–S2, 2.2776(8); Fe1–C51, 1.791(3); Fe1–C52, 1.789(3); Fe1–C53, 1.805(3); Fe2–S1, 2.2678(7); Fe2–S2, 2.2743(7); Fe2–C54, 1.793(3); Fe2–C55, 1.806(3); Fe1–C56, 1.796(3); S1–Fe1–S2, 81.24(3); S1–Fe2–S2, 81.13(3). CCDC 2183292 contains supplementary crystallographic data. The figure is adapted from ref. 127 or **Paper I** with permission from WILEY-VCH Verlag GmbH.

Infrared spectroscopy was employed to probe the CO ligands in **2**, bands reflecting the CO stretching frequencies were observed at 2081, 2049 and 2011 cm^{-1}. **(Figure 4.2)**.

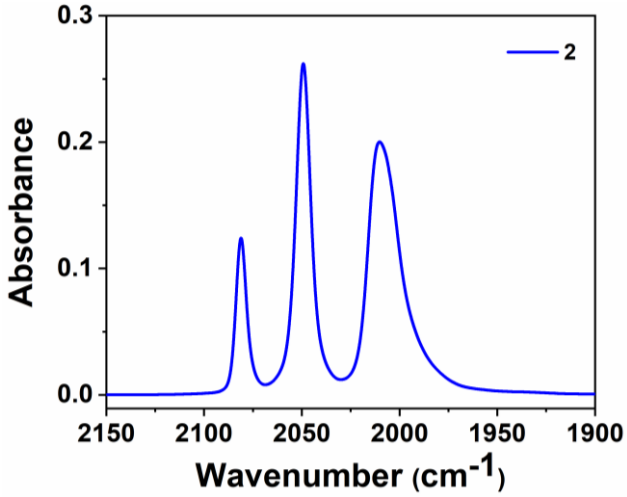

Figure 4.2: Infrared spectrum (transmission mode) of complex **2** (blue trace), in $CHCl_3$ (conc.~ 3mM).

4.5 Electrochemistry

4.5.1 Homogenous CV assay

To start with, the electrochemical characterization of complex **2** was performed in organic media (0.1 M tetrabutylammonium hexafluorophosphate or $TBAPF_6$ in DMF) using CV. 1 mM solutions of **2** showed a quasi-reversible process at $E_{1/2}$ = –1.26 V *vs.* $Fc^{+1/0}$(with a peak separation, $E_{p,c} - E_{p,a} = \Delta E_p$ = 60 mV). This redox event is tentatively attributed to a single step $2e^-$ ($Fe^{(I)}Fe^{(I)}/Fe^{(0)}Fe^{(0)}$) reduction due to potential inversion, as previously reported for complex **1**.[141] Scanning towards more negative potentials revealed an irreversible reduction followed by a quasi-reversible reduction event at $E_{p,c}$ = –2.44 V and –2.55 V (ΔE_p = 78 mV), respectively. The former process could not be characterised with confidence, and tentatively attributed to either metal or bridging ligand-based reduction. The latter event (at –2.55 V) was assigned to a pyrene based redox process **(Figure 4.3, red trace)**. Addition of 20 equivalent (or 20 mM) of trifluoroacetic acid (TFA) to a 1 mM solution of **2**, resulted in a complete loss of reversibility, and a concomitant anodic shift by 40 mV of the aforementioned $2e^-$ reduction event. In parallel, a large catalytic current evolved upon addition of acid, reaching up to 90 µA at –1.98 V (~45 times the current as compared to 0 mM TFA at same potential) **(Figure 4.3, green trace)**. The catalytic current was attributed to H_2 evolution based on previous reports for analogous [Fe_2(µ-bdt)CO_6] complexes[143–146].

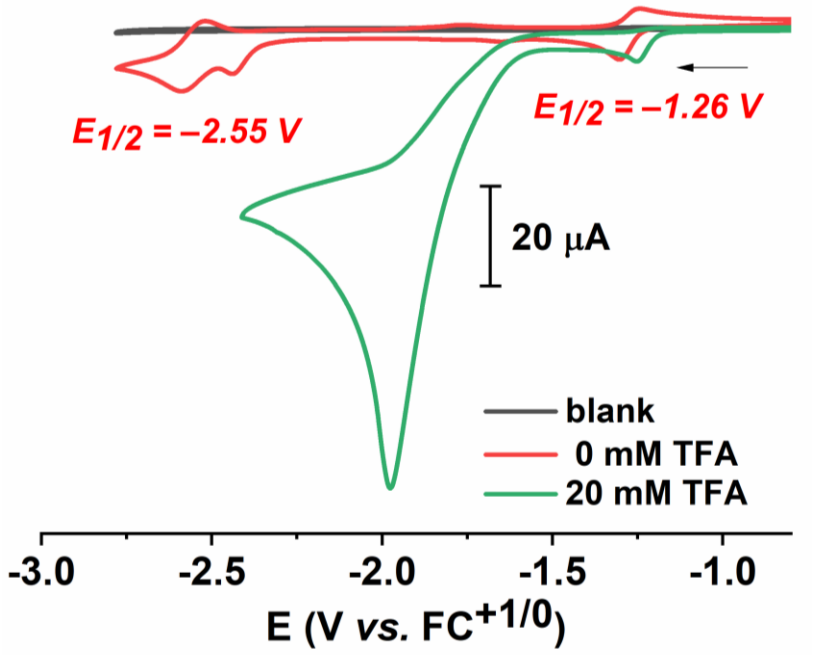

Figure 4.3: CV traces of a 1 mM solution of **2** under homogenous condition in organic media in the absence or presence of trifluoroacetic acid (red = 0 mM, green = 20 mM). Here, blank is defined as the CV trace of the glassy carbon electrode (d =1.6 nm) in same organic electrolyte deprived of **2** and TFA. All CV traces were recorded in DMF, with 0.1 M $TBAPF_6$, at room temperature, v = 100 mV s^{-1}. The figure is adapted from ref. [127] or **Paper I** with permission from WILEY-VCH Verlag GmbH.

Thus, CV assessments while titrating with acid indicates that complex **2** is active for H^+ reduction (see ref.[127] or **Paper I** for detailed discussion).

4.5.2 Heterogenous CV assay

Exploiting the pyrene groups, complex **2** was then immobilized on MWNT using π–π interactions (abbreviated as **2**/MWNT onwards). Complex **1** was instead physiosorbed to MWNT (abbreviated as **1**/MWNT onwards) in a similar fashion as a reported previously (see ref.[127] or **Paper I** for more details for immobilisation procedure).

The amount of catalysts immobilized on the electrode (or "loading") was estimated by performing CV studies of **1**/MWNT and **2**/MWNT in organic media (0.1 M $TBAPF_6$ in CH_3CN). The latter experiments allowed to estimate 7.6 ± 0.9 nmol cm^{-2} of electroactive sites at the electrode for complex **2**, 40% higher than that of complex **1** (4.5 ± 0.6 nmol cm^{-2}). Thus, integration of diiron species on MWNT using pyrene outperformed physisorption in term of loading capacity. Independently, a catalyst loading of 9.5 ± 0.1 nmol cm^{-2} was estimated by desorbing the catalyst from MWNT in DMF and performing UV-Vis spectroscopy. The characteristic peak of pyrene at 345 nm (ε_{345nm} = 1.95 x 10^5 M^{-1} cm^{-1} for complex **2**) was used to calculate the loading. Comparing the loading estimated from CV and UV-Vis data, suggests that about 80% of the total amount of grafted complex is redox active (see ref.[127] or **Paper I** for detailed discussion).

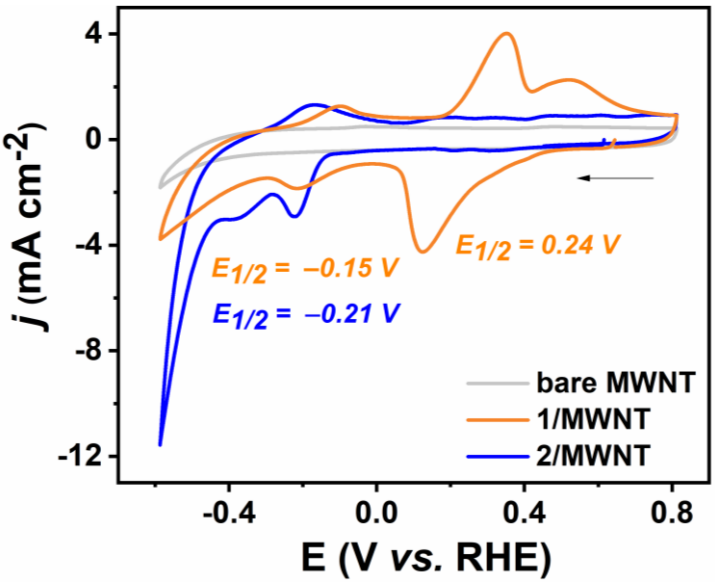

Figure 4.4: CV traces of **1** (orange trace) and **2** (blue trace) immobilized on MWNT in aqueous media. Trace of bare MWNT (grey trace) represent the CV of a blank MWNT electrode. All CVs were recorded in 0.2 M sodium phosphate buffer at pH 7. All CV traces were collected at room temperature, v = 100 mV s^{-1}. $E_{1/2}$ = half wave potential. The figure is adapted from ref.[127] or **Paper I** with permission from Wiley-VCH Verlag GmbH.

The electrochemical properties of **1**/MWNT and **2**/MWNT were further assessed under completely aqueous condition in 0.2 M sodium phosphate buffer, pH 7. The results showed contrasting behaviour between **1** and **2**. To start with, **2**/MWNT displayed a quasi-reversible peak at –0.21 V *vs.* RHE followed by an irreversible reduction event at $E_{p,c}$ = –0.36 V *vs.* RHE, tentatively attributed to the $Fe^{(I)}Fe^{(I)}$/ $Fe^{(I)}Fe^{(0)}$ and $Fe^{(I)}Fe^{(0)}$/ $Fe^{(0)}Fe^{(0)}$ redox couples respectively **(Figure 4.4, blue trace)**. The small separation between the reduction events was possibly due to stabilisation of reduced species via structural change(s) or protonation.

In comparison, **1**/MWNT showed $Fe^{(I)}Fe^{(I)}$/$Fe^{(I)}Fe^{(0)}$ signal at –0.15 V *vs.* RHE similar to **2**/MWNT whereas the $Fe^{(I)}Fe^{(I)}$/ $Fe^{(0)}Fe^{(0)}$ process could not be defined clearly. In addition, **1**/MWNT showed a quasi-reversible process at $E_{1/2}$ = 0.24 V *vs.* RHE, attributed to a quinone/quinol ($2e^-/2H^+$) redox event, which was not observed for **2**/MWNT **(Figure 4.4, orange trace)**. Sweeping towards more negative potential, a large catalytic wave was observed for **2**/MWNT. The onset potential of the process was estimated at –0.44 V *vs*. RHE, and the current amplitude reached –11.9 ± 0.9 mA cm^{-2} for **2**/MWNT, three times higher than that of **1**/MWNT (–3.9± 0.9 mA cm^{-2}) at –0.6 V *vs*. RHE **(Figure 4.4)**. The improved current density in case of complex **2** was tentatively attributed to better anchoring with MWNT, relative to the weak physisorption for the complex **1**.

4.5.3 Electrocatalytic H_2 evolution activity

In order to detect the product, estimate the efficiency and asses the robustness of **2**/MWNT during electrocatalytic conditions, chronoamperometry (CA) coupled with gas chromatography (GC) was

performed in 0.2 M sodium phosphate buffer, pH 7. The electrode was poised at –0.49 V *vs*. RHE in an attempt to balance between catalyst inactivation (observed upon repeated scan CV, see reference for more details) while still ensuring relatively large currents **(Figure 4.5)**.

As before, **1**/MWNT was studied similarly as a reference. At the start of the CA experiment, **2**/MWNT showed an initial current density of –0.7 ± 0.2 mA cm^{-2} (at t= 2 min) which gradually dropped within the first three hours to reach –0.3 ± 0.1 mA cm^{-2}. Afterwards, the current density remained reasonably stable for 20 hours, at which point the experiment was terminated (final current –0.25 ± 0.03 mA cm^{-2}). In comparison, CA of **1**/MWNT under equivalent condition showed an initial current density of –0.42 ± 0.09 mA cm^{-2} (at t = 2 min), which dropped to –0.22 ± 0.02 mA cm^{-2} and –0.18 ± 0.01 mA cm^{-2} after three and 20 hours respectively. Thus, on longer time-scales, the currents of **1**/MWNT were difficult to distinguish from those of bare MWNT, determined to about –0.175 mA cm^{-2} under these experimental conditions.

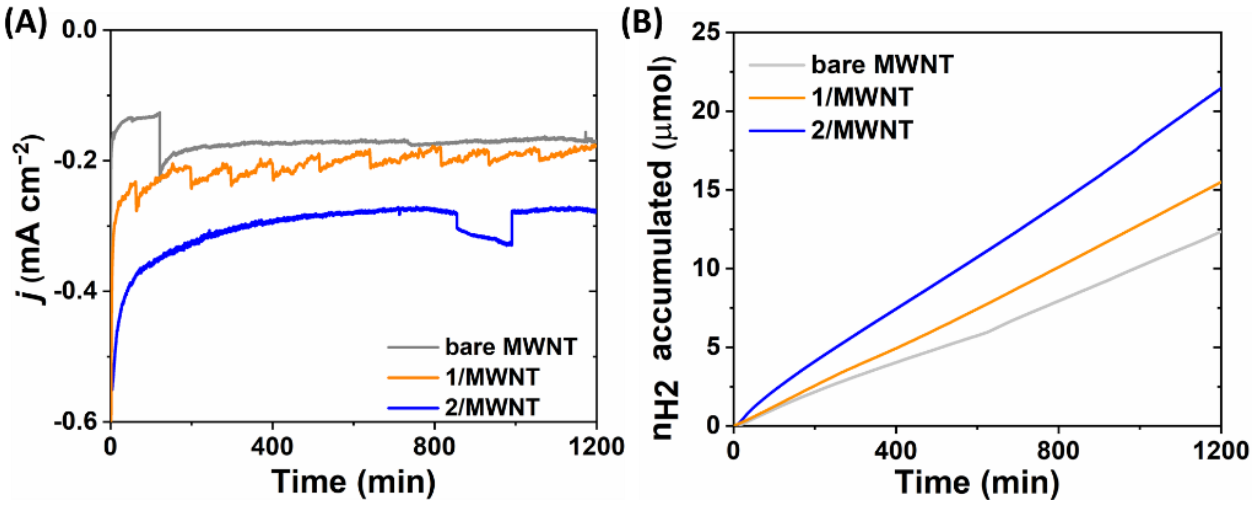

Figure 4.5: Electrocatalytic H_2 production by **1**(orange trace), **2** (blue trace) functionalized electrodes and bare MWNT (grey trace). (A) current density and (C) corresponding production of H_2, over 20 hours during CA. Electrodes poised at –0.49 V *vs*. RHE in 0.2 M sodium phosphate buffer of pH 7 under Argon at room temperature. The fluctuation of current in CA was attributable to bubble formation at the working electrode during electrolysis. The figures are adapted from ref. [127] or **Paper I** with permission from WILEY-VCH Verlag GmbH.

The Faradic efficiency (FE_{H2}) was ≈ 98–99% and 15 ± 1 and 19 ± 3 µmol of H_2 were quantified from **1**/MWNT and **2**/MWNT within the course of 20 hours of CA respectively.

Table 4.1: Quantitative analysis of CA by **1**/MWNT and **2**/MWNT showed in **Figure 4.5**. Here, blank = bare MWNT, ΔQ = Amount of charge consumed, *j* = current density; n_{H2} = mol of H_2 produced, FE_{H2} = faradic efficiency, TON_{H2} = turnover number for hydrogen production during CA. The table is adapted from ref.[127] or **Paper I** with permission from Wiley-VCH Verlag GmbH.

Catalyts	***j*** **(t= 2 min)** **(mA cm^{-2})**	***j*** **(t= 20 h)** **(mA cm^{-2})**	**n_{H2} produced** **(µmol)**	**ΔQ** **(C)**	**FE_{H2}** **%**	**loss of *j* during CA** **%**	**TON_{H2}**
Blank	–0.185	–0.17	12.67	2.45	99.96	8	
1	–0.42 ± 0.09	–0.18 ± 0.01	15 ± 1	2.89 ± 0.11	98.6 ± 0.4	58 ± 4	2 ± 1 × 10^3
2	– 0.71 ± 0.17	–0.25 ± 0.03	19 ± 3	3.8 ± 0.6	99.1 ± 0.4	64 ± 4	4 ± 2 × 10^3

This corresponds to 2.2 ± 0.6 and 7 ± 3 µmol of H_2 and to a TON_{H2} of 2 ± 1 × 10^3 and 4 ± 2 × 10^3 based on total catalyst loading of **1** and **2**, respectively, after subtraction of the H_2 produced by

bare MWNT **(Figure 4.5, Table 4.1)**. The latter values should be considered conservative as direct H_2 evolution at the MWNT surface might be lower when the electrode is modified with **1** or **2**, and the higher value for the surface concentration of **2** (from UV-Vis) was employed to calculate the TON_{H2} **(Figure 4.5, Table 4.1)**.

4.6 *Post operando* assessment

In order to understand the fate of the catalyst after CA, a *post operando* analysis of **2**/MWNT was performed using CV and spectroscopy *i.e.* UV-Vis, Infrared and XPS.

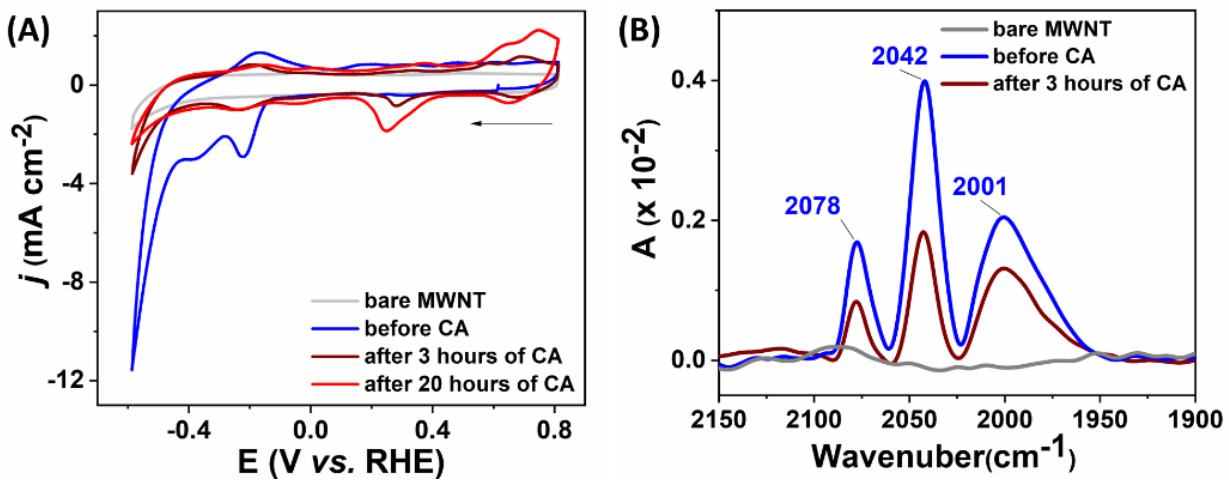

Figure 4.6: *Post operando* assessment of **2**/MWNT via electrochemistry and Infrared spectroscopy. (A) CV (v = 100 mV s^{-1}) of **2**/MWNT before (blue trace), after three hours (brown trace) and 20 hours (red trace) of CA. (B) Infrared spectra (ATR mode) of **2**/MWNT before (blue trace) and after 3 hours (brown trace) of CA. CA was performed poised at −0.49 V *vs*. RHE, in 0.2M sodium phosphate buffer of pH 7. The figure is adapted from ref.[127] or **Paper I** with permission from WILEY-VCH Verlag GmbH.

CV revealed 65–70% loss of current amplitude for the catalytic (at –0.49 V) as well as the stoichiometric processes (at –0.22 V) after three hours and further decreases were observed after 20 hours **(Figure 4.6 A)**. Interestingly, despite the loss in current, UV-Vis spectroscopy revealed negligible loss of pyrene from the MWNT film during 20 hours of CA (see ref. or **Paper I** for detailed discussion). In contrast, infrared spectroscopy showed between 35% and 55% loss of intensity of the characteristic CO peaks at 2001, 2042 and 2078 cm^{-1} after three hours of electrolysis **(Figure 3.6 B)**. Thus, while the Fe-CO core appears to degrade over the course of the electrolysis, the pyrene anchoring groups are retained at the surface of the electrode even after 20 hours of electrolysis. Finally, XPS of **2**/MWNT was collected at different intervals of CA (before, after one hour, three hours and 20 hours of CA). The latter study showed characteristic binding energies of the elements present on **2**/MWNT and allowed to quantify them. This revealed a gradual loss of Fe ions during CA while the relative quantity of the other elements (C, O, S) remained almost constant. In addition, the chemical environment of S (sulphur) was found to be modified substantially by formation of various to thiolate (RS^-) and sulphate species (*e.g.* RSO_n^- where n = 2, 3) during CA (See ref.[127] or **Paper I** for detailed discussion) . Thus, overall the *post operando* assessment hints towards a degradation of the catalyst during CA due to loss of Fe-S bonds.

4.7 Discussion

The immobilisation of the catalyst on MWNT allowed this water insoluble catalyst to function in aqueous media. This is an important aspect with respect to the objective of the eSCALED project discussed in **Section 2.1,** as the device should be functional under aqueous conditions, as a sustainability perspective. Electrolysis by the catalyst (**2**) functionalised electrode showed a

moderate activity as compared to related previously reported heterogeneous systems as shown in **Table 4.2**.

Table 4.2: List of electrochemical hydrogen evolution reaction (HER) for heterogeneous molecular catalyst-based systems, functional under aqueous conditions. The table is partially adapted from ref.[127] or **Paper I** with permission from WILEY-VCH Verlag GmbH.

Catalyst	support	electrolyte	Applied potential *vs.* RHE	TON	Ref.
(μ-$S_2(CH_2)_2NAr$) $[Fe(CO)_3]_2$	Pyrolytic graphite electrode	0.5 N H_2SO_4	–480 mV	$>10^8$	[115]
(μ-$S_2(CH_2)_2NAr$) $[Fe(CO)_3]_2$	Pyrolytic graphite electrode	0.2N H_2SO_4	–658 mV	$>10^7$	[114]
$Ni[P(CH_2)_2N^{Ar})]_4$	Carbon nanotube	0.5 M H_2SO_4	–280 mV	10^5	[147]
$Co(DO)(DOH)$ -$pnCl_2$	Carbon nanotube	pH 4.5	–590 mV	5.5×10^4	[148]
Complex **2**	Carbon nanotube	pH 7	–490 mV	$\sim 0.5 \times 10^4$	[This work]

Here, Ar = aromatic functional group, $((DOH)_2pn)$ = N_2, N_2-propanediylbis (2,3butanedione 2-imine 3-oxime).

The *post operando* assessment revealed that the loss of activity was not due to a poor anchoring strategy but rather due to degradation of the active site via loss of Fe-S bonds during long term electrolysis **(Scheme 4.2**). The notion of Fe-S bond cleavage was further supported by several reports on related immobilized and homogeneous systems. For example, an analogous degradation pattern was reported for the closely related complex $[Fe_2(\mu\text{-}SC_6H_4\text{-}p\text{-}OH)_2(CO)_6]$ under heterogeneous conditions.[149] In addition, computational studies of $[Fe_2(\mu\text{-}bdt)(CO)_6]$[146,150], $[Fe_2(\mu\text{-}edt)(CO)_6]$[151] and spectro-electrochemical analysis of $[Fe_2(\mu\text{-}pdt)(CO)_6]$[108] under homogenous conditions, revealed the lability of Fe–S bonds during reduction.

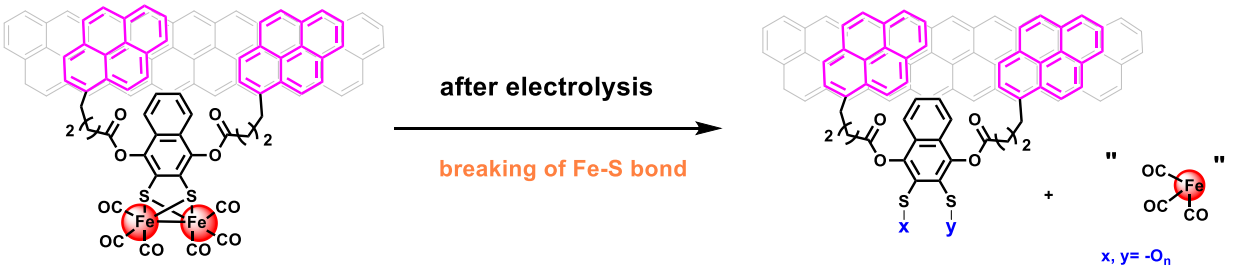

Scheme 4.2: Possible degradation route of immobilized complex **2** during the electrocatalytic process. The figure was adapted from ref.[127] or **Paper I** with permission from WILEY-VCH Verlag GmbH.

The exact reason for the fragility of the Fe-S bonds is not clear. During reduction, the valence electron count shift from 18 e^- (inert electronic configuration as per the 18e^- rule) to unstable 19 and 20 e^-. I speculate that e^- added during reduction enter into an σ* (antibonding) orbital of the Fe-S bond, weakening the bond **(Figure 4.7)**. Computational studies further support this assumption by showing a lengthening of one of the Fe-S bonds after one e^- reduction, causing structural changes from butterfly arrangement to a square arrangement followed by lengthening of the Fe-Fe bond.[151–153] Subsequent one e^- reduction strongly favours a complete depletion of a Fe-S bond which also forces one of the CO ligands from terminal to bridging position.[146,150] During long term electrolysis, the consequence of weakening the Fe-S bond becomes an issue, and resulted in complete loss of Fe ions from the active site.

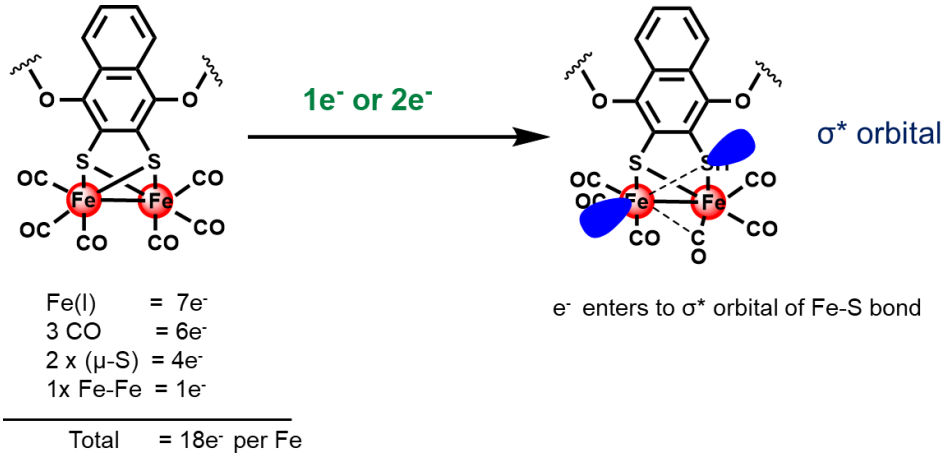

Figure 4.7: Possible reason for the lability of Fe-S bonds of complex **2** during electroreduction.

4.8 Summary

Altogether, the study discussed in this Chapter presents the first reported immobilization of a $\{Fe_2(\mu\text{-}S_2)(CO)_6\}$ based [FeFe] hydrogenase mimics using π-π interaction on MWNT.
Three key insights obtained from this study are as follows:

(i) The catalytic loading capacity was substantially improved using pyrene and π-π interaction as compared to physisorption.
(ii) The resulting electrode materials were functional at neutral pH, and the durability of the anchoring group *i.*e. pyrene on MWNT under catalytic condition was appreciable.
(iii) H_2 evolution activity was moderate and the active site suffers from degradation.

Thus, this study successfully meets two out of four objectives (objectives **a**, **b**, see **Section 2.2**) by synthesising a H_2 evolution catalyst and improving loading up to 9.5 nmol cm^{-2} with ~80% of the loaded sites participating in catalysis. The results clearly indicate the requirement of improving the catalyst to meet the rest of the objectives (objectives **c**, **d** see **Section 2.2**). This can potentially be achieved by engineering a proper secondary coordinator sphere around active site, and thereby enhancing activity and stability.

Chapter 5 : Paper II – Inclusion of naphthoquinone bridging {$Fe_2(\mu\text{-}S_2)(CO)_6$} based active site inside polymeric scaffold

5.1 Brief introduction & motivation

As summarised in **Chapter 4**, in parallel with the immobilisation strategy, the development of an efficient catalyst is necessary. The latter can potentially be achieved through re-designing of the catalyst by introducing a proper outer coordination sphere (OCS). Shaw *et al* nicely summarised the importance of OCS in the context of molecular catalysts for promoting activity towards energy transformations.[81] In that context, encapsulation of active sites inside suitable scaffolds has proven itself very promising in recent years as discussed in **Section 1.7.1.1**. One striking example of such macromolecular scaffolds was reported by Brezinski *et al.* back in 2019.[142,154] The authors demonstrated that incorporation of a water-insoluble and poorly active naphthoquinone bridged {$Fe_2S_2(CO)_6$} based active site,[141] inside a polymer called PDMAEMA containing a tertiary amine (-$N(CH_3)_2$) (referred as [2Fe2S]-[PDMAEMA]) showed remarkable improvement in electrochemical hydrogen evolution activity. To be specific, the authors claimed a remarkable TOF_{max} of 2.5 x 10^4 s^{-1} with a low onset potential (–0.2 V *vs.* RHE) under homogenous conditions in neutral 1M TRIS buffer, pH7.[142,154]

5.2 Objective

The objective was to adapt the metallopolymer design of Brezinski *et al.*[142] for surface immobilization, and explore its properties under more device like conditions. Thus, the aforementioned metallopolymer [2Fe2S]-PDMAEMA or **3a** was redesigned to include an anchoring group (*i.e.* pyrene) to generate metallopolymers called "[2Fe2S]-P[DMAEMA-*r*-PyBMA]" or **3b–e.** The resulting metallopolymers could then be grafted on MWNT for heterogeneous electrochemical H_2 production. For that a pyrene containing linker *i.e.* 4-(pyren-1-yl)-butyl methacrylate (PyBMA) was designed **(Scheme 5.1)**.

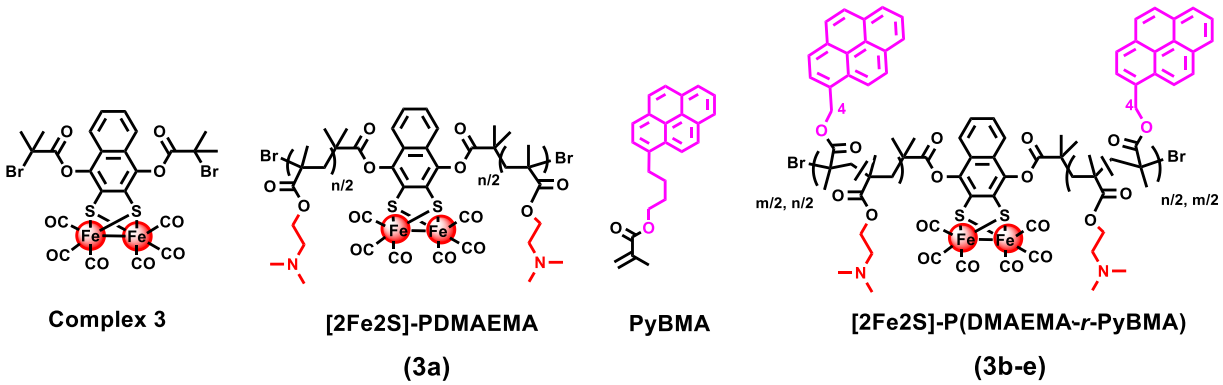

Scheme 5.1: Schematic representation of designed and synthesized molecules. The metal initiator, *i.e.* complex **3**, [2Fe2S]-(PDMAEMA) or **3a**, the pyrene linker or PyBMA and [2Fe2S]-P[DMAEMA-*r*-PyBMA] or **3b–e**. Here, [2Fe2S]: diiron containing subsite; DMAEMA: dimethylaminoethyl acrylate; PyBMA: 4-(pyren-1-yl)-butyl methacrylate. n and m are the number of DMAEMA and PyBMA per active site. It was assumed the polymer chain is equally distributed between each shoulder of the active site. The values of n and m for each metallopolymer is summarized in **Table 5.1**.

5.3 Synthesis

PyBMA was synthesized through an esterification reaction between 1-pyrenebutanol and Methacrolyl chloride. The polymers, [2Fe2S]-P[DMAEMA-r-PyBMA] (or **3b–e**), were subsequently synthesized using Atomic Transfer Radical Polymerization (ATRP) from a synthetically prepared metal initiator (**3**) as reported for [2Fe2S]-[PDMAEMA] (**3a**) previously.[142] Although, the addition of the pyrene containing monomer, PyBMA, during polymerization constitutes a key difference. The reported metallopolymer **3a** is hydrophilic[142], but introduction of pyrene could cause an increase in hydrophobicity. Therefore, a series of metallopolymers (***3b–e***) were synthesized by varying the mol% (with respect to DMAEMA) of pyrene in order to optimize between hydrophilicity and anchoring strength while also retaining high activity **(Scheme 4.1)**. To be specific 5 mol%, 10 mol%, 15 mol% and 20 mol% of PyBMA was used to synthesise, **3b**, **3c**, **3d** and **3e** respectively. Finally, metallopolymer **3a** (i.e. the metallopolymer deprived of pyrene) was also prepared to elucidate the influence of pyrene towards activity and durability on the electrode surface during catalysis (see ref. [135] or **Paper II** for more details).

5.4 Characterization

All synthesized materials were characterized by a range of spectroscopic techniques. ^{1}H NMR showed several characteristic peaks for each monomer *i.e.* signals between 8.4 –7.8 ppm, 7.64 –7.49 ppm and 4.06 – 2.19 ppm originated from PyBMA, **3** and DMAMEMA respectively (for more details, see ref.[135] or **Paper II**). Integrating the aforementioned respective characteristic peaks allowed to calculate the ratio between each monomer and thereby estimate the composition of each metallopolymer, as shown in **Table 5.1**. Thus, ^{1}H NMR analysis confirmed a gradual increase of pyrene from **3b** to **3e**, indicating the incorporation of ~3.8 (**3b**), ~7.8 (**3c**), ~10.5 (**3d**) and ~18.6 (**3e**) mol% of pyrene with respect to DMAEMA in the final metallopolymers **(Table 5.1,** For more details, see ref.[135] or **Paper II)**.

Table 5.1: Quantitative analysis of all metallopolymers **3a – e**. This table was adapted from ref. [135] or **Paper II** with permission from American Chemical Society.

Metallopolymers	Name	DMAEMA(n)/PyBMA(m)/diiron final molar ratio[a]	mol% of PyBMA	Fe content[b] (mg_{Fe}/g of polymer)	M_n[c] (g/mol)	Đ[c]
[2Fe2S]-PDMAEMA	**3a**	88/ 0 / 1	0	10.0	15,900	1.78
[2Fe2S]-P(DMAEMA-*r*-PyBMA)	**3b**	137 / 5.0 / 1	3.8	3.8	23,800	1.63
	3c	86 / 7.4 / 1	7.8	6.3	19,200	1.68
	3d	102/ 12 / 1	10.5	5.5	14,700	1.64
	3e	69/ 16 / 1	18.6	4.9	7,700	2.12

[a] calculated from ^{1}H NMR spectrum
[b] measured by ICP-OES
[c] measured by SEC

Size exclusion chromatography (SEC) showed a range of molecular weights (M_n) between 7,700 to 23,800 g mol^{-1} and a polydispersity index (*Đ*, see **Section 3.3** for the definition) between 1.6–2.2. The large value of *Đ* (*i.e.* greater than 1.5) could be due to the differential growth of the polymer chain on each side of active site. The exact molecular weights of metallopolymers are summarized in **Table 5.1**. ICP-OES measurements also confirmed the presence of Fe, with a content between 3.8–10 mg per g of metallopolymers **(Table 5.1)**. Infrared spectroscopy validated the presence of the intact di-iron core of **3** in each polymer by showing stretching bands of the Fe-CO ligands at 2081, 2049 and 2011 cm^{-1}, 1–2 cm^{-1} bathochromically shifted as compared to that of **3 (Figure 5.1)**.

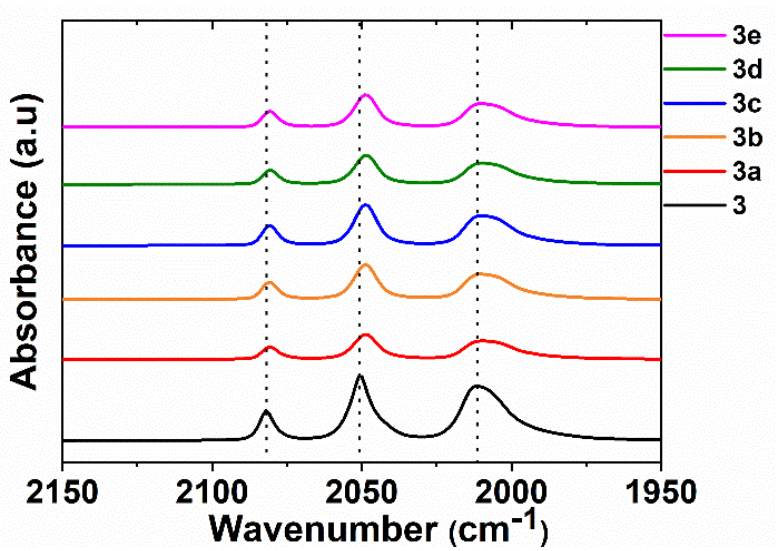

Figure 5.1: Infrared spectra (transmission mode) of the metal initiator **3** and metallopolymers **3a –e** in $CHCl_3$. The intensity of infrared traces for **3b–e** were multiplied by 10 times compared to that of **3** for better comparison. The dotted lines represent the peak position of CO bands. The traces for **3**, **3a**, **3b**, **3c**, **3d** and **3e** were represented by black, red, orange, blue, green and magenta colors respectively. The figure is adopted from ref.[135] or **Paper II** with permission from American Chemical Society.

Finally, it was found that introduction of hydrophobic pyrene units to the hydrophilic parent metallopolymer **3a** had a substantial impact on overall hydrophilicity of the metallopolymers, and only **3a**, **3b** and **3c** showed appreciable water solubility.

5.5 Electrochemistry

5.5.1 Homogenous CV assay

To simplify our discussion, I will only describe metallopolymers **3a**, **3c** and **3e** here (for details about **3b** and **3d**, see ref.[135] or **Paper II**). Among the three metallopolymers considered for the discussion (**3a**, **3c** and **3e)**, only **3a** and **3c** were water soluble. Hence, they were submitted to an electrochemical characterisation under homogeneous condition in aqueous buffer using CV. Both of these metallopolymers (**3a** and **3c**) showed a large catalytic current with an onset potential between –0.31 to –0.33 V *vs.* RHE. The currents reached between –11.6 to –13.2 mA cm^{-2} at –0.8 V *vs.* RHE, with maximum current density obtained from **3a (Figure 5.2, Table 5.2)**. These number matches well with the previous report of metallopolymer **3a** (maximum HER current of about 6 mA cm^{-2} in 0.1 M phosphate buffer + 0.1 M KCl, conc. of metallopolymer =100 µM)[142] attesting that the presence of pyrene did not alter the electrocatalytic properties significantly.[142]

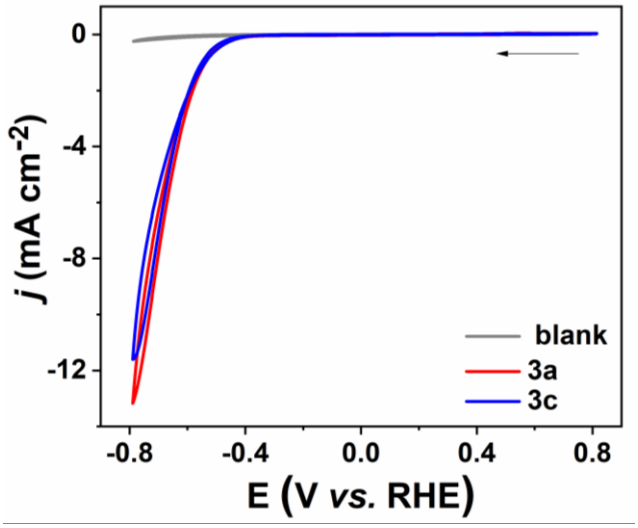

Figure 5.2: CV traces of dissolved metallopolymers **3a** and **3c** (100 µM). CVs were recorded in 0.2 M sodium phosphate buffer pH 7 at room temperature under argon (v = 100 mV s^{-1}). Here, traces for the blank (no metallopolymer added), **3a** and **3c** were represented by grey, red and blue colours respectively. The working electrode was a glassy carbon electrode (d=1.6 mm). The figure is adopted from ref.[135] or **Paper II** with permission from American Chemical Society.

5.5.2 Heterogeneous CV assay

Metallopolymers **3c** and **3e** were then immobilized on MWNT (referred to as **3c**/MWNT and **3e**/MWNT for the rest of the discussion). In order to understand the influence of the anchoring group (*i.e.* PyBMA), the metallopolymer deprived of pyrene (*i.e.* **3a**) was also grafted on MWNT (**3a**/MWNT), *via* physisorption. The electrochemical properties of the aforementioned functionalized electrodes were initially tested in organic media (0.1 M $TBAPF_6$ in CH_3CN) in order to estimate the loading of active sites (similar to what was performed with complex **2**, discussed in **Chapter 3**). A catalytic loading of 1.1 ± 0.1, 1.6 ± 0.1 and 1.5 ± 0.1 nmol cm^{-2} were estimated for **3a, 3c** and **3e**, respectively. As expected considering the size of the metallopolymers (hydrodynamic radius between 28 – 30 Å), the loading was 5 – 6 times lower than that of **2**, **(Table 5.2**, for more details, see ref.[135] or **Paper II)**. The electrochemical properties of the metallopolymer–functionalized electrodes were then explored under aqueous conditions. Both **3a**/MWNT and **3c**/MWNT showed a large catalytic current with an onset potential of –0.22 to –0.23 V *vs.* RHE, and the currents reached up to 14.8 – 15.3 mA cm^{-2} at –0.6 V *vs.* RHE **(Figure 5.3A)**. Thus, **3a** and **3c** showed substantial improvements in activity following surface immobilization, with a positive shift of the catalytic response by 90 – 100 mV as compared to their CV traces in solution **(Table 5.2)**. The relatively low activity under homogenous condition could

be attributed to the poor diffusion rate of the metallopolymers (diffusion coefficient in water, D = 6.4 – 6.7 $\times 10^{-11}$ m^2 s^{-1}, for more details, see ref.[135] or **Paper II**).
A marginal loss of current density was noticed while switching from **3a** to **3c** despite of an improvement in loading **(Table 5.2)**. This loss of activity can be correlated with increment of hydrophobicity in **3c** due to presence of pyrene. The impact of pyrene on activity was more pronounced for **3e** discussed below.
The CV study of **3e**/MWNT displayed a negative shift of the onset potential by 40 – 50 mV (or – 0.27 V *vs.* RHE) with respect to that of the water soluble metallopolymers (**3a** and **3b)**. CV traces of **3e**/MWNT also displayed a decrease of catalytic current density by about 25% as compared to the water-soluble polymers (**3a** and **3c**), reaching –10.9 ± 0.3 mA cm^{-2} at –0.6 V *vs.* RHE **(Figure 5.3A)**. Such a loss of activity could not be rationalized by low active site loading. Rather, it correlated with the poor water solubility of **3e**, which could affect the interaction between buffer and catalyst as discussed earlier.

Table 5.2: Quantitative analysis of CV analysis of metallopolymers under homogenous and heterogeneous conditions. All CVs were performed in 0.2 M phosphate buffer, pH 7. The table is partially adopted from ref.[135] of **Paper II** with permission from American Chemical Society.

Catalyst	Homogenous condition		Heterogenous condition[a]		
	Onset potential (V *vs.* RHE)	Current density at –0.8 V *vs.* RHE* (mA cm^{-2})	Onset potential (V *vs.* RHE)	Current density at –0.6 V *vs.* RHE (mA cm^{-2})	Active site loading (nmol cm^{-2})
3a	–0.31	–13.2	–0.22	–15.3 ± 0.2	1.1 ± 0.1
3c	–0.33	–11.6	–0.23	–14.8 ± 0.2	1.6 ± 0.1
3e	n.a.	n.a.	–0.27	–10.9 ± 0.3	1.5 ± 0.1
2	n.a.	n.a.	–0.44	–11.9 ± 0.9	7.6 ± 0.9

a = when catalysts were immobilized on MWNT
* : the standard deviations under homogenous condition were marginal.
**na: not applicable

Interestingly, comparing the CV data of the aforementioned metallopolymer functionalized MWNT systems with **2**/MWNT revealed that metallopolymeric approach causes a significant anodic shift of the onset potential by 170 – 220 mV for catalysis. In addition, the current densities at –0.6 V *vs*. RHE for the metallopolymer functionalised electrodes were ~20% (at least for **3a** and **3c**) higher, despite a 5 to 7-fold lower active site loading as compared to **2 (Figure 5.3B, Table 5.2)**. These results clearly illustrate the critical role of the polymeric scaffold towards improving catalytic rates and lowering overpotential requirements.[155]

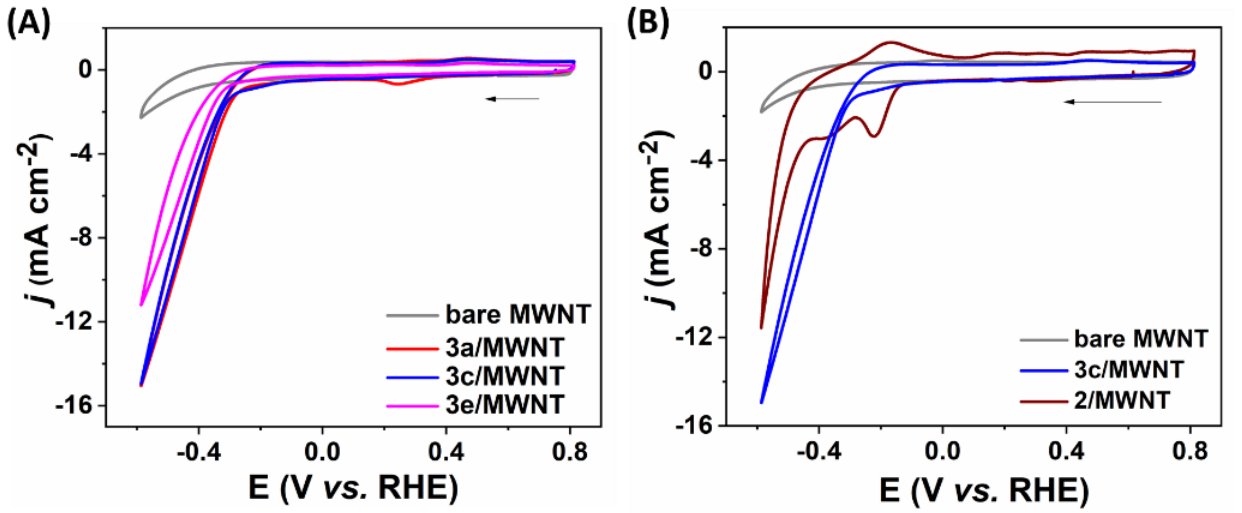

Figure 5.3: CV traces of the metallopolymer-modified MWNT with **3a, 3c** and **3e**. Comparison of CV traces for (A) **3a, 3c** and **3e** and; (B) that for **3c** and **2**, immobilized on MWNT. All CV traces were recorded in 0.2 M sodium phosphate buffer, pH 7 at room temperature under argon (v = 100 mV s^{-1}). Here, traces for blank MWNT, **3a**/MWNT, **3c**/MWNT, **3e**/MWNT and **2**/MWNT were represented by grey, red, blue, magenta and brown colours, respectively. The figures are adopted from ref.[135] or **Paper II** with permission from American Chemical Society.

5.5.3 Electrochemical H_2 evolution activity

The robustness of the metallopolymers functionalized electrodes and the effect of pyrene content on long-term performance were evaluated using CA. The potential was set to –0.39 V *vs.* RHE, and the cell was coupled with in-line gas GC **(Figure 5.4)**. The choice of applied potential was based on the mid-wave potential of the catalytic current observed by CV, in order to balance between maximum current density and rapid inactivation of catalysts at more negative potential (for more details, see ref.[135] or **Paper II**).

CA of **3a**/MWNT showed an initial current density of –2.0 ± 0.2 mA cm^{-2} (at t = 1 min) **(Figure 5.4A red trace)**. This value was relatively lower than the current density obtained at –0.39 V *vs* RHE during first scan of CV (~5.5 mA cm^{-2}), showed in **Figure 5.3A**. There could be few possible reasons contributing this loss of current between CV and CA. Firstly, CA data was always collected after running first scan of CV. Repetitive scans during CV revealed that the current density lost between 30 to 35% (5.5 mA cm^{-2} to 3.7 mA cm^{-2}) between first two scans (data not shown here). Therefore, direct comparison between the initial current density obtained in CA with that at first scan of CV is unfair. Secondly, CV collects currents from both faradic and non-faradic processes (like, increase in capitative current via polarisation of electrode due to potential switch during CV) whereas CA collects currents from faradic processes only. Continuing CA of **3a**/MWNT revealed a gradual decline in current density over time, resulting in a loss of ~95% of its initial current density within ~15 hours to reach –0.11 ± 0.02 mA cm^{-2}. The latter current was very close to that of blank MWNT, *i.e.* 0.04 mA cm^{-2}. Introduction of ~7.8% of pyrene caused substantial improvement in the stability. **3c**/MWNT showed an initial current density of –3.6 ± 0.4 mA cm^{-2} (at t = 1 min). Comparison that with initial current density of **3a**/MWNT was found interesting. Despite both (*i.e.* **3a** and **3c** on MWNT) having similar CV responses, CA showed substantially higher current density for **3c**/MWNT than that of **3a**. It was due to the additional durability of catalyst on electrode, originated with the presence of pyrene. Latter fact was supported by showing a better retention of current density between first two scans at –0.39V for **3c** (~20% loss *i.e.* 4.7 mA cm^{-2} to 3.8 mA cm^{-2}) compared to **3a** discussed earlier (for details, see ref.[135] or **Paper II**). This improvement of durability on increasing pyrene percentage was further validated by CA as the current density of **3c**/MWNT retained almost 25% of the initial current density after ~15 hours. This allowed to extend the electrolysis up to 20 hours, at which point a final current density of 0.6 ± 0.1 mA cm^{-2}, *i.e.* a retention of 19.4 ± 2.6% of the initial current density was observed **(Figure 5.4A blue trace)**. For both **3a**/MWNT and **3c**/MWNT the Faradic efficiency was 99 – 100%, and the resulting H_2 production was 19.1 ± 3.3 and 100 ± 14 µmol for **3a**/MWNT and **3c**/MWNT after

~15 and 20 hours of electrolysis, respectively. This corresponds to a TON_{H2} of 0.8 ± 0.1 ×10^5 and 3.1 ± 0.4 ×10^5 (TON_{H2} were calculated after subtracting with H_2 production by bare MWNT, see **Section 3.3** for calculation) for **3a** and **3c**, while immobilized on MWNT during CA, respectively **(Figure 5.4B, Table 5.3)**.

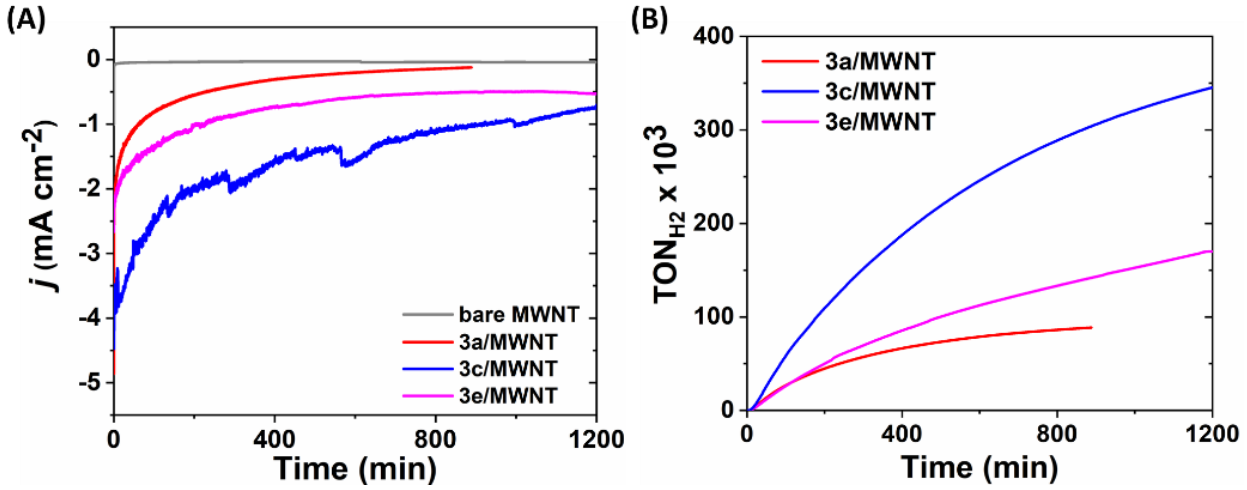

Figure 5.4: Bulk electrolysis and corresponding TON_{H2} of synthesized **catalyst**/MWNT. (A) CA traces; (B) corresponding traces of TON_{H2} for **3a**, **3c** and **3e** when immobilized on MWNT. CA traces were obtained by setting the working electrode potential at –0.39 V in 0.2 M sodium phosphate buffer at pH 7, at room temperature and under argon. Here, traces for bare MWNT, **3a**, **3c** and **3e** were represented by grey, red, blue and magenta colours respectively. The fluctuation in CA traces are due to bubble formation near the electrode during the measurements. TON_{H2} was calculated by subtracting H_2 produced by blank MWNT under equivalent condition. The figures are adopted from ref.[135] or **Paper II** with permission from American Chemical Society.

Increasing the pyrene content further to reach about 18.6% (as in **3e**/MWNT), resulted in a drop of activity. **3e**/MWNT displayed an initial current density of –2.0 ± 0.2 mA cm^{-2} (at t = 1 min), and retained 18.6 ± 5.2% of the initial current density (–0.4 ± 0.1mA cm^{-2}) after 20 hours of electrolysis. In total, **3e**/MWNT produced 45 ± 10 µmol of H_2, representing a TON_{H2} of 1.4 ± 0.3 ×10^5 after 20 hours **(Figure 5.4 magenta traces, Table 5.3)**. The loss of activity on increasing the pyrene percentage above ~7.8% was likely due to the increased hydrophobicity of **3e** as compared to **3c** as explained earlier. Hence, about 7.8% pyrene with respect to DMAEMA was found to be an ideal composition for maximum activity, while retaining considerable durability under catalytic conditions. This trend was further complemented by performing the same experiments for **3b** (containing about 3.8% pyrene) and **3d** (containing about 10.5% pyrene) to obtain an approximately bell-shaped plot of TON_{H2} *vs.* %pyrene with a peak TON_{H2} reached by **3c** (~7.8% pyrene) **(Figure 5.5A** , see ref. [135] or **Paper II** for details about **3b** and **3d)**.

Table 5.3: Quantitative analysis of bulk electrolysis of metallopolymers immobilized on MWNT, CA data shown in **Figure 5.4** and **4.5**. The CA were performed at –0.39 V vs RHE in 0.2 M phosphate buffer, pH 7. The standard deviation was calculated based on replicates (at least three times with same batch of metallopolymers) of each experiment. Replicates are not shown here. Loading of metallopolymers were shown **Table 5.2**. This Table is adopted from ref.[135] or **Paper II.**

Catalysts	*j* at t =1 min of CA (mA cm^{-2})	*j* at t = 20 hours of CA (mA cm^{-2})	n_{H2} produced during CA (µmol)	Retention of current after CA %	TON_{H2} × 10^5
Blank*	–0.1	–0.04	2.9		
3a	–2.0 ± 0.2	–0.11 ± 0.02	19.1 ± 3.3	5 ± 0.4	0.8 ± 0.1
3c	–3.6 ± 0.4	–0.6 ± 0.1	100 ± 14	16.6 ± 1.8	3.1 ± 0.4
3e	–2.0 ± 0.2	–0.4 ± 0.1	45 ± 10	18.6 ± 5.2	1.4 ± 0.3
2**	– 0.7 ± 0.1	–0.25 ± 0.03	19.3 ± 3	36 ± 4	0.04 ± 0.02

*blank = bare MWNT.
CA of **2/MWNT was performed at –0.49 V *vs.* RHE.

Interestingly, comparing the performance of the metallopolymers to **2**/MWNT revealed that the latter assembly could produce relatively poor initial catalytic currents (–0.7 ± 0.1 mA cm^{-2}), despite applying 100 mV more negative potential (–0.49 V *vs*. RHE). As a result, the isolated diiron site **2** could only reach a TON_{H2} of about 4 ± 2 ×10^3 (discussed in **Chapter 4**), two orders of magnitude lower than that of the best metallopolymer **3c (Figure 5.5B)**. Although, **2**/MWNT appeared to retain about 36% of its initial current density after 20 hours of electrolysis, this is likely an overestimate of the stability of **2**. Indeed, in the case of **2**/MWNT ~60 –70% of the current density recorded at the end of CA (*i.e.* at t = 20 hours), was potentially attributable to background current density of the bare MWNT (see **Chapter 4**). Thus, encapsulation of the diiron centre in a macromolecular scaffold enhanced the (electro) catalytic rate and stability of the catalyst functionalized electrode substantially under catalytic condition.

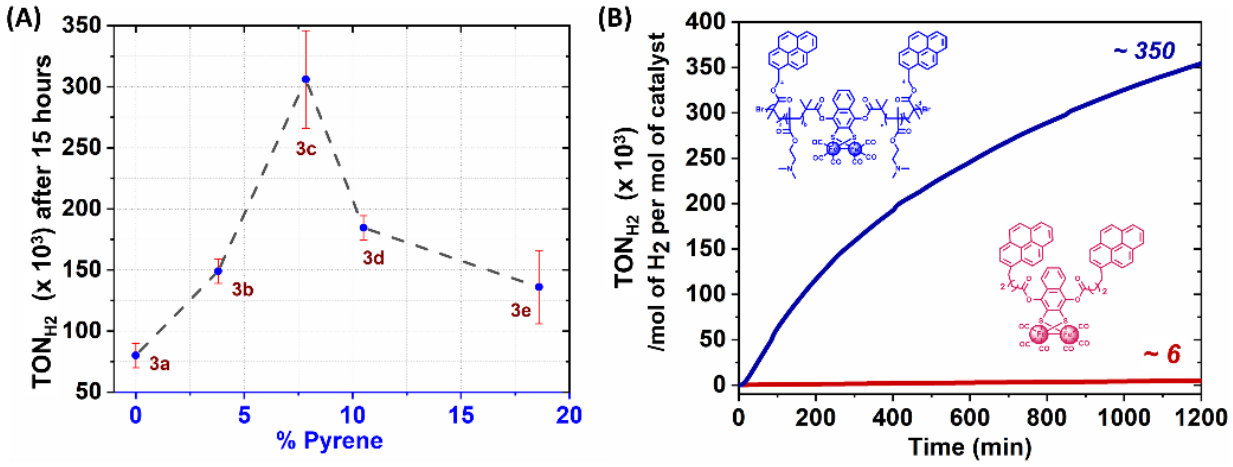

Figure 5.5: (A) Analysis for TON_{H2} of electrochemical hydrogen production (black, y axis) after 15 hours of CA *vs.* %Pyrene (blue, y axis) for metallopolymers **3a–e** while immobilized on MWNT. (B) Comparison of TON_{H2} for **3c** (blue trace) and **2** (brown trace) while immobilized MWNT during CA. CA were performed at –0.39 V *vs.* RHE and –0.49 V *vs.* RHE in 0.2 M sodium phosphate buffer of pH 7 at room temperature under argon for **3a–e** and **2** respectively. % of pyrene was calculated with respect to mol% of other monomers (see **Table 5.1**). The figures are partially adopted from ref.[135] or **Paper II** with permission from American Chemical Society.

5.6 *Post operando* assessment

For all metallopolymer functionalized electrodes (**3a–e**/MWNT), at least ~80% of the initial current density was lost during extended electrolysis **(Figure 5.4, Table 5.3,** for more details see ref.[135] or **Paper II)**. In order to understand the fate of the catalysts during catalysis, a *post operando* assessment was performed. As outlined in **Chapter 3**, this included CV and spectroscopy. Comparing CV traces recorded before and after CA showed a considerable loss of catalytic currents for all metallopolymer functionalized electrodes (**3a–e**/MWNT) **(Figure 5.6A,** for other metallopolymers, see ref.[135] or **Paper II)**. The loss of currents in both CA and CV clearly shows that the catalyst is degrading over time. However, it is positive to note that no new potentially catalytic processes are discernible, as that could imply the formation of catalytically active degradation products. In parallel, UV-Vis spectroscopy of **3b–e** revealed negligible loss of pyrene from the electrodes over the course of CA. In addition, an increase in background current was noticed ~300 nm which could not be explained with clarity **(Figure 5.6B**, see ref. [135]or **Paper II** for plots for other metallopolymers**)**.

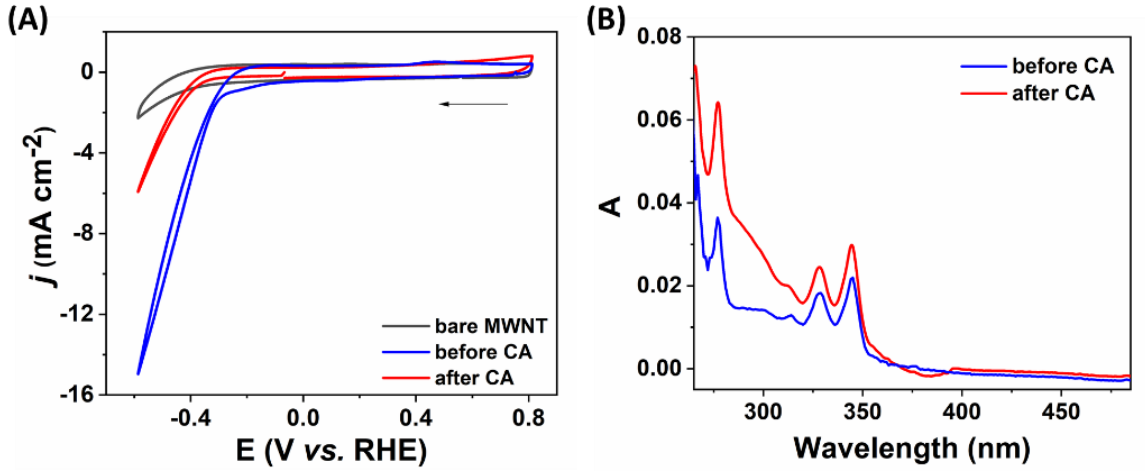

Figure 5.6: *Post operando* analysis of **3c**/MWNT using CV and UV-Vis spectroscopy. (A) CV traces (v =100 mV s^{-1}); and (B) UV-Vis spectra, before (blue trace) and after (red trace) CA. CV and CA were performed at in 0.2 M sodium phosphate buffer, pH 7 at room temperature. UV-Vis spectra were performed after desorbing the metallopolymer from the electrodes in 3 mL DMF. The figures are adapted from ref. [135] or **Paper II** with permission from American Chemical Society.

Finally, XPS measurements on **3c**/MWNT were recorded before and after two hours of CA. XPS spectra revealed a substantial loss of Fe ions while the quantity of the other elements from the metallopolymers (C, N, O, S) remained constant during CA. A similar trend with loss of Fe ions was also noticed when the XPS analysis was performed after repetitive CV scans (for more details, see ref.[135] or **Paper II**).

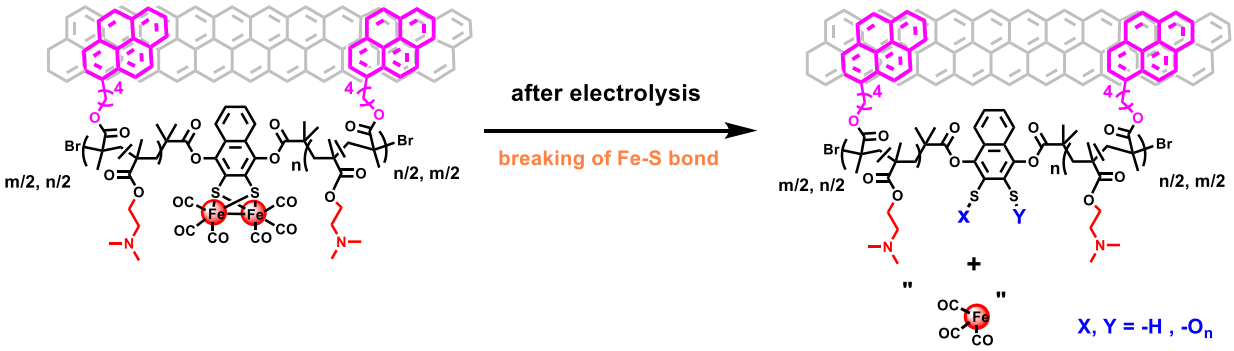

Scheme 5.2: Possible degradation route of polymers during electrolysis. The figure is adopted from ref.[135] or **Paper II** with permission from American Chemical Society.

Thus, the *post operando* assessments support the loss of catalysis due to the loss of the Fe ions and bound CO ligands **(Scheme 5.2)**. This is in good (or rather unfortunate) agreement with what was observed also for **2**/MWNT mentioned in **Chapter 4**, and earlier literature reports on related systems.[108,146,149–151]

5.7 Discussion

Inclusion of pyrene in the polymer composition enabled the resulting metallopolymers (**3b–e**) to be immobilize on electrode surfaces via π-π interactions. Comparing the CV data between homogenous and heterogenous condition revealed that immobilization of the metallopolymers causes improvement in current density and a decrease in overpotential requirements. These improvements highlight the better electronic communication between the electrode and metallopolymers under heterogenous conditions. In addition, immobilization of the metallopolymers via π-π interactions offers better loading as well as higher activities and durability of the metallopolymers under catalytic conditions, compared to physisorption. Thus, pyrene remain an important factor for promoting catalytic performances of the electrode materials. Nevertheless, exceeding ~7.8 mol % of pyrene caused a drop in activity, as pyrene bring hydrophobicity to the polymer as a drawback. In general, a certain degree of water solubility of the catalyst is necessary in order promote the interaction between substrate (proton in buffer) and catalyst. Therefore, optimizing between pyrene ratio and activity is important to achieve maximum activity while retaining substantial durability of discussed functionalised electrode materials.

In addition to the issue of pyrene and hydrophobicity, a second challenge associated with the encapsulation strategy is the increased foot-print of the catalyst. Indeed, the advantages of the polymeric scaffolds comes at expense of 5 – 6 times lower loading than that of the isolated diiron site **2** (deprived of polymeric scaffold). Finally, the metallopolymeric approach could not prevent the degradation of the active site. Therefore, the active site remains the weak link of the assembly and improvements are still required to obtain a robust catalyst.

5.8 Summary

To summarize, I have designed and synthesized a series of metallopolymers, denoted [2Fe2S]-P(DMAEMA-*r*-PyBMA), by varying the pyrene content between 5 to 20 mol % during the synthesis. The basic design was derived from a reported metallopolymer called [2Fe2S]-(PDMAEMA).[142] The work outlined in this Chapter illustrates five key aspects of developing efficient bioinspired catalysts for H_2 production as follows:

1. Encapsulation of the active site inside a properly engineered macromolecular scaffold offers substantial improvements in activity.
2. Immobilisation of metallopolymers on electrode surfaces (using both physisorption and π-π interaction) resulted in substantial improvement of activity, and lowering overpotential requirements.
3. Immobilisation of metallopolymers using π-π interactions could improve the catalyst loading, durability of catalysis and consequently overall catalytic performance under catalytic condition.
4. Tuning the hydrophilicity of the metallopolymers is one of the key parameters to control as it can alter the catalytic efficiency significantly.
5. The metallopolymer approach could not prevent degradation of the active sites during catalysis.

Thus, the metallopolymer strategy allowed to partially meet the targeted objective **c** (or promotion of H_2 evolution activity and durability under catalytic conditions) mentioned in **Section 3.2**. Therefore, encapsulation of more robust active sites inside a polymeric scaffold should be a reasonable approach to achieve better durability during catalysis and efforts related to this will be the topic of the next Chapter.

Chapter 6 : Paper III – Inclusion of styrene-based amine bridgehead [FeFe] hydrogenase mimic inside polymeric scaffold

6.1 Brief introduction and motivation

As discussed in **Chapter 5**, the activity of our first metallopolymers was limited by degradation of their active sites via breakage of Fe-S bonds and a more robust active site is required. The lability of the Fe-S bond during reduction, is an intrinsic property for $\{Fe_2(\mu\text{-}S_2)(CO)_6\}$ derivatives with aromatic and some aliphatic (*i.e.* edt, pdt)[108] bridges. As discussed in **Section 1.7.1.2**, Dey *et al.* showed the that presence of an amine group at the bridgehead position could add several benefits to the complex with regards to catalysis, *i.e.* oxygen tolerance,[123] stability in protic media under reducing conditions[115] and bidirectionality[124]. Therefore, it would be interesting to replace the fragile naphthoquinone-dithiol bridging ligand of the $\{Fe_2(\mu\text{-}S_2)(CO)_6$ active site by a potentially more robust $\{Fe(\mu\text{-adt})(CO)_6\}$ based active site.

Weigand *et al.* tried to introduce such a $\{Fe(\mu\text{-adt}')(CO)_6\}$ (adt´= $SCH_2N(R)CH_2S$-, R= aromatic substituents) based complex inside a polymeric scaffold using Reversible addition−fragmentation chain-transfer (RAFT) polymerization, previously. However, the authors reported that the synthesis remained unsuccessful due to poor stability of the diiron site under the reaction conditions.[156]

6.2 Objective

Here, the objective was to redesign the first generation metallopolymers (**3a–e**) by replacing the active site with a styrene substituted $\{Fe(\mu\text{-adt}')(CO)_6\}$ complex (complex **4**), and to synthesize metallopolymers $[2Fe2S]_k$ $[DMAEMA]_l$ $[PyBMA]_m$. Three different metallopolymers were synthesized, denoted **4a–c**, by varying the pyrene ratio between 1 to 10 mol% with respect to DMAEMA **(Scheme 6.1)**.

6.3 Synthesis

Synthesis of complex **4** was performed via a multistep synthetic route starting from $Fe(CO)_5$, following a previously reported protocol.[156] Unlike the synthesis of **3a–e,** the diiron complex was then treated as a monomer rather than metal initiator along with DMAEMA and PyBMA during the polymer synthesis. The synthesis of the new metallopolymers was performed via free radical polymerization between complex **4**, DMAMEMA, PyBMA using azobisisobutyronitrile (AIBN) as initiator. During the polymerization, the mol% of PyBMA was varied as 1%, 5% and 10% to obtain **4a**, **4b** and **4c** respectively **(Scheme 6.1)**.

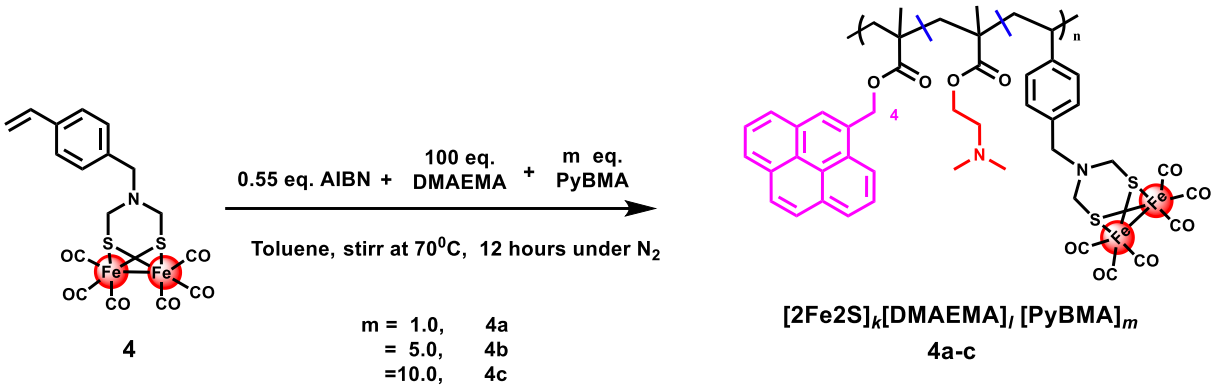

Scheme 6.1: Synthesis route for the metallopolymer **4a–c** using AIBN as an initiator. Here k:l:m represents the molar ratio between **4**, DMAEMA and PyBMA in the metallopolymers respectively. The exact composition ratios for metallopolymers **4a –c** were shown in **Table 6.1**. The figure is adapted from ref. [157] or **Paper III**).

6.4 Characterization

^{1}H NMR spectra of metallopolymers **4a–c** exhibited characteristic peaks at 8.4 – 7.8 ppm, 7.3 – 7.1 ppm and 4.06 – 2.19 ppm attributed to PyBMA, diiron sites derived from **4** and DMAEMA, respectively. Integration of these signals allowed to estimate the composition of the metallopolymers's backbone by calculating the ratio between each monomer. This analysis indicated ~0.9 mol%, ~2.3 mol% and ~6.6 mol% of pyrene present in **4a**, **4b** and **4c** respectively **(Table 6.1)**.[157] UV–Vis spectroscopy further attested the increased pyrene ratio going from **4a** to **4b** and **4c** as the typical characteristic peaks of pyrene between 255 – 355 nm increased along the series (for details, see ref. [157] or **Paper III**). ICP–OES analysis estimated ~ 4 – 9.55 mg of Fe per g of the metallopolymers. SEC of metallopolymers **4a–c** showed molecular weights between 14,200–17,300 g mol^{-1} with $Đ^c$ between 2.2 to 2.7. These large values of $Đ^c$ reflect inhomogeneity in the metallopolymers, possibly due to the non-controlled nature of the applied free radical polymerization **(Table 6.1)**.

Table 6.1: Quantitative analysis of metallopolymers **4a –c.** The table is adopted from ref. [157] or **Paper III**).

Polymers	Name	DMAEMA(l)/PyBMA(m) /diiron site (k) final molar ratio[a]	mol% of PyBMA	Fe content[b] (mg_{Fe}/g of polymer)	M_n[c] (g/mol)	$Đ^c$
$[2Fe2S]_k$ $[DMAEMA]_l$ $[PyBMA]_m$	**4a**	37/ 0.35/1	0.9	9.55	14,200	2.7
	4b	62/ 1.5/ 1	2.3	4.07	16,650	2.2
	4c	53/ 3.8/ 1	6.6	4.0	17,300	2.3

[a] calculated from ^{1}H NMR spectrum
[b] measured by ICP-OES
[c] measured by SEC

Infrared spectroscopy validated the presence of intact active sites inside **4a–c**, by showing peaks at 2074, 2036 and 2001 cm^{-1} which correspond to the stretching of CO ligands bound to the Fe ions **(Figure 5.1)**. A comparison to the spectra observed for metallopolymers **3a –e** (2081, 2049 and 2011 cm^{-1}, see **Section 4.4**), revealed that newly designed metallopolymers **4a–c** showed a 7 to 13 cm^{-1} bathochromic shift. This suggests a relatively higher electron density at the metal centre in **4a–c**.

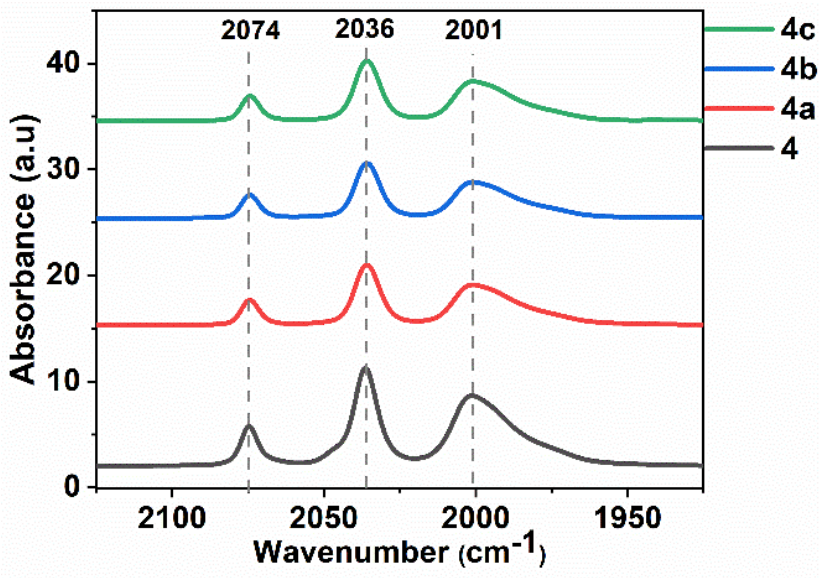

Figure 6.1: Infrared spectra (transmission mode) of **4** and **4a –c** in $CHCl_3$.The intensity of traces are multiplied by three times for **4a** and 10 times for both **4b**, **4c** as compare to **4** for better comparison. The figure is adapted from ref. [157] or **Paper III**).

The SEC study in combination with infrared spectroscopy and ICP–OES analysis showed the presence of 1.2 to 1.6 active sites per mol of **4a** and 0.6 to 1 active site per mol of both **4b** and **4c** (for details, see ref. [157] or **Paper III**). Finally, all three metallopolymers (**4a–c)** showed appreciable solubility (at least 15 mg mL^{-1}) in water.

6.5 Electrochemistry

The electrochemical assessment was initially performed under homogenous conditions in organic and aqueous media.

6.5.1 Homogenous CV assay

The synthetic precursor complex **4** , showed a quasi-reversible peak at –1.54 V *vs*. $Fc^{+1/0}$ (ΔE_p = 116 mV, $i_{p,a}/i_{c,a}$ ~0.92) which is attributed to a $1e^-$ reduction ($Fe^{(I)}Fe^{(I)}/Fe^{(I)}Fe^{(0)}$) as reported for analogous diiron complexes.[115,123,158] Switching towards more oxidizing conditions, the complex showed an irreversible oxidation event at $E_{p,a}$ = 0.56 V *vs*. $Fc^{+1/0}$ which is attributed to a $1e^-$ oxidation ($Fe^{(I)}Fe^{(I)}/Fe^{(I)}Fe^{(II)}$) event **(Figure 6.2A)**.

Introducing the active sites inside polymeric scaffold caused slight loss in reversibility as shown in one of the metallopolymers here. More specifically, metallopolymer **4b** showed a quasi-reversible $1e^-$ (reduction and an irreversible $1e^-$ oxidation events at $E_{1/2}$= –1.56 V *vs.* $Fc^{+1/0}$ (ΔE_p = 160 mV, $i_{p,a}/i_{c,a}$ ~0.65) and $E_{p,a}$ = 0.44 V *vs*. $Fc^{+1/0}$, respectively **(Figure 6.2B)**. Very similar observation was also noticed for **4a** and **4c** here (see ref. [157] or **Paper III** for more details).

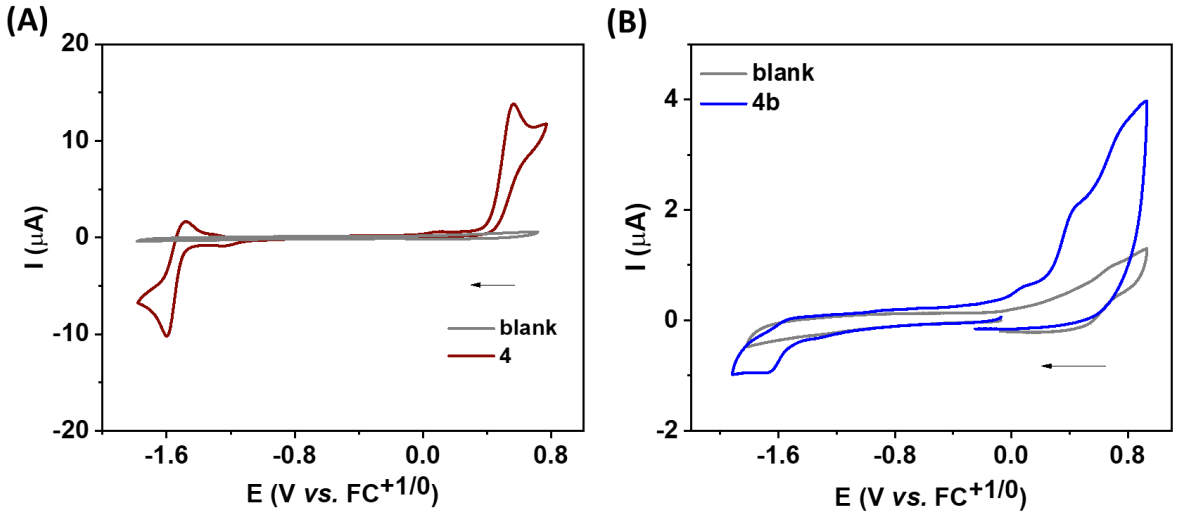

Figure 6.2: CV traces of (A) 1 mM complex **4**; and (B) 0.5 mM metallopolymer **4b** in 0.1 M $TBAPF_6$ in CH_3CN under argon (v = 100 mV s^{-1}). A glassy carbon (d =1.6 mm) was used as working electrode. Blank is defined as CV traces of a glassy carbon electrode at 0.1 M $TBAPF_6$ in CH_3CN under argon.

Taking advantage of their water solubility, **4a–c** were characterized electrochemically also under aqueous condition in 0.2 M sodium phosphate buffer, pH 7. All three metallopolymers (conc. =100 μM) showed a noticeable catalytic current with an onset potential between –0.34 to –0.36 V *vs.* RHE, reaching maximum a current density between –1.2 to –2.4 mA cm^{-2} at –0.65 V *vs.* RHE with maximum activity (with respect concentration of the metallopolymers) displayed by **4a (Figure 6.3A, Table 6.2)**.

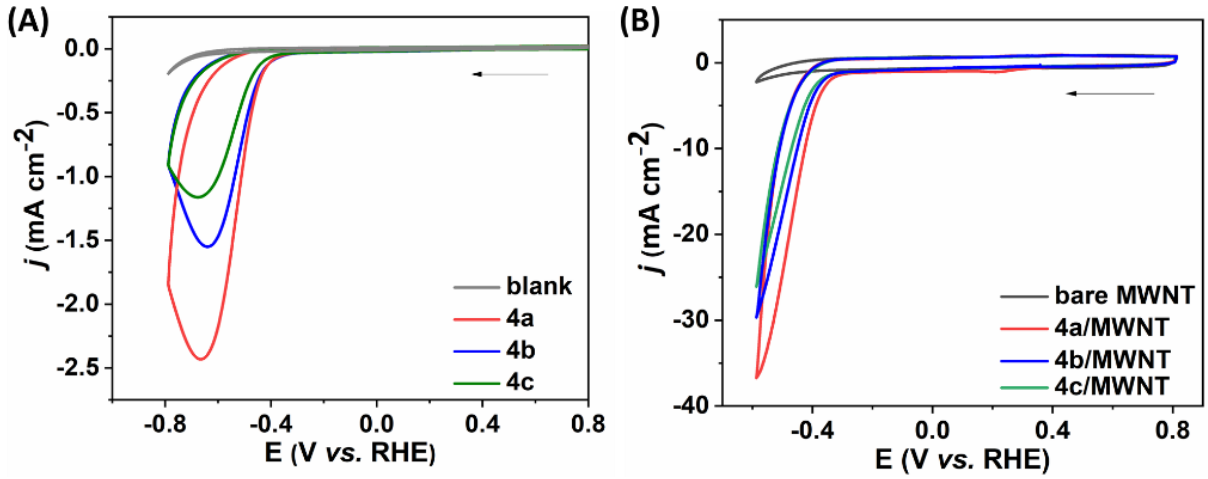

Figure 6.3: CV traces of metallopolymers **4a–c** in aqueous media. (A) homogenous conditions with a concentration of 100 μM catalyst; (B) while immobilized on MWNT. The experiments were recorded in 0.2 M sodium phosphate buffer, pH 7 under argon (v = 100 mV s^{-1}). Both CVs were performed under ohmic drop compensated condition. Blank trace in panel A, was represented for CV of glassy carbon electrode (d = 1.6 nm) in applied buffer. Here, bare MWNT, **4a**, **4b** and **4c** were represented by grey, red, blue and green colours respectively. The figures are adapted from ref. [157] or **Paper III.**

6.5.2 Heterogeneous CV assay

Exploiting the presence of pyrene, the metallopolymers **4a–c** were then immobilized on MWNT (to give **4a–c**/MWNT). Subsequently, their electrochemical activities were assessed starting with CV under aqueous conditions in 0.2 M sodium phosphate buffer, pH 7. It was again found that the electrochemical activities were substantially improved under heterogeneous conditions. More specifically, **4a–c**/MWNT showed 20–30 mV anodic shifts of the onset potential (*i.e.* –0.32 to –0.33 V), as compared to what was observed under homogenous conditions (**Figure 6.3B**). The current densities were also enhanced to reach between –24 to –37 mA cm^{-2} at –0.6 V *vs*. RHE.

The relatively poor activity under homogenous conditions is again tentatively attributed to poor diffusion rates of the macromolecules, which could be circumvented by immobilizing the catalysts on the electrode.

The loading of active sites on MWNT was estimated through a CV study in organic media (0.1 M $TBAPF_6$ in CH_3CN). As observed under homogenous conditions, the metallopolymers showed a quasi-reversible event at ~ $E_{1/2}$ = –1.55 V (ΔE_p ~22 –28 mV) which allowed to quantify the active sites loading to 3.45 ± 0.1, 2.09 ± 0.04 and 2.63 ± 0.67 nmol cm^{-2} for **4a**, **4b** and **4c**, respectively (see ref. [157] or **Paper III** for more details). The difference in loading of diiron sites between metallopolymers were due to combined effect of both the difference in Fe concentration and size of metallopolymers **(Table 6.1)**.

Table 6.2: Quantitative analysis of CV analysis of **4a-c** under homogenous and heterogeneous conditions, CV traces were shown in **Figure 6.3**.

Catalyst	Homogenous conditions		Heterogeneous conditions[a]		
	Onset potential under homogenous condition (V *vs.* RHE)	Current density at –0.65 V *vs.* RHE* (mA cm^{-2})	Onset potential under homogenous condition (V *vs.* RHE)	Current density at –0.6 V *vs.* RHE (mA cm^{-2})	Loading as per electrochemistry (nmol cm^{-2})
4a	–0.34	–2.42	–0.32	–36 ± 1	3.45 ± 0.1
4b	–0.35	–1.55	–0.33	–28 ± 1	2.09 ± 0.04
4c	–0.36	–1.17	–0.33	–24 ± 2	2.63 ± 0.67

a= when catalysts were immobilized on MWNT
* : standard deviations for currents under homogenous condition were marginal

6.5.3 Electrochemical H_2 evolution activity

To assess the robustness of the metallopolymer functionalized electrodes, CA experiments were performed at –0.49 V *vs.* RHE in 0.2 M sodium phosphate buffer, pH 7. The choice of applied potential was based on the mid-wave potential of the CV traces showed in **Figure 6.3B**, like I discussed for metallopolymers **3a –e**.

CA of **4a**/MWNT (~0.9% of pyrene) commenced with a current density of –2.89 ± 0.05 mA cm^{-2} (at t =1 min). Again, the current density was much lesser than that at –0.49 V *vs.* RHE during CV (~20 mA cm^{-2}). The possible reasons behind the loss of current density between CA and CV were the same as explained for **3a-e** in previous Chapter (**Section 5.5.3)**. In addition to that, for **4a–c**, CVs were performed with ohmic drop compensated condition, resulted in substantial increment in current density which was not applicable for CA. Extending the CA of **4a**/MWNT showed gradual loss of current density over the first six hours to reach –0.3 ± 0.1 mA cm^{-2}. Afterwards, the current density remains almost stable until the end of the 20 hours long CA experiment, at which point it had reached – 0.20 ± 0.06 mA cm^{-2} (very close to that of blank MWNT *i.e*. –0.17 mA cm^{-2}). This corresponds to a retention of 6.7 ± 2 % of the initial current density (likely largely attributable to the bare MWNT) after 20 hours. Increasing the pyrene content to about 2.3 % (*i.e.* **4b**) resulted in substantial improvements in performance. CA of **4b**/MWNT showed a very similar initial current density to that of **4a** with −2.72 ± 0.05 mA cm^{-2} at t=1 min, but retained 24.1 ± 2.6% of the initial current density after 20 hours of CA (−0.65 ± 0.08 mA cm^{-2}) **(Figure 6.4A)**. However, increasing the pyrene percentage further, up to ~6.6% (*i.e.* **4c**), caused an instant drop in activity. CA using **4c**/MWNT displayed an initial current density of −0.93 ± 0.1 mA cm^{-2} (at t =1 min), which dropped to −0.44 ± 0.01 mA cm^{-2} after 20 hours of CA **(Figure 6.4 A)**. It is important to note that all metallopolymers showed a continues loss of current density in first three hours (except **4a** which was six hours) of CA and afterwards, the current density remain remarkably stable till end of CA unlike metallopolymers **3a–e** discussed in previous Chapter (see ref. [157] or **Paper III** for more details).

During the CA, the Faradic efficiency for all functionalised electrodes was 98 –100%, and consequently **4a**, **4b** and **4c** could reach TON_{H2} (calculated by subtracting with H_2 production by bare MWNT) of 2.53 ± 0.04 ×10^4, 9.8 ± 0.4 ×10^4 and 4.3 ± 0.4 ×10^4 in 20 hours while immobilized on MWNT **(Figure 6.4B)**. Thus, these metallopolymers appear to follow the same trend as previously noticed for **3a–e** (discussed in **Chapter 5**). In other words, for both metallopolymer series, **3a–e** and **4a–c**, increasing pyrene ratio only up to certain percentage resulted in promotion in activity. In addition to strong anchoring, optimized pyrene ration could also able to create a balanced local hydrophobic environment around active site (similar to that found in enzymes) to elevate the activity. However, latter hypothesis could not be supported experimentally at this stage.

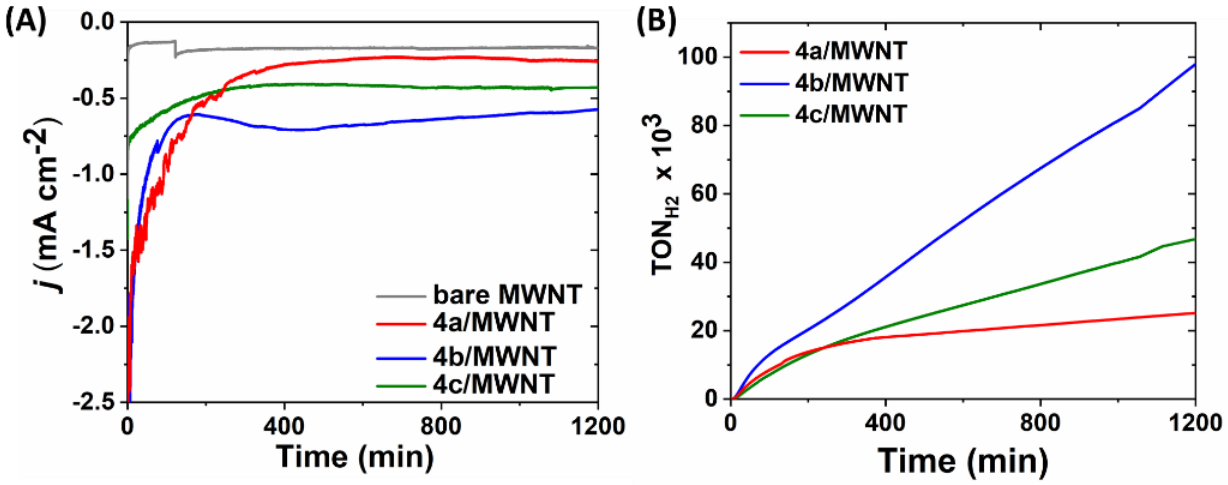

Figure 6.4: CA of metallopolymers **4a–c** immobilized on MWNT. (A) current density (*j*) vs. time; (B) TON_{H2} *vs.* time, recorded during CA. The experiments were recorded by setting the working electrode at a potential of –0.49 V *vs.* RHE, in 0.2 M sodium phosphate buffer, pH 7. Here, bare MWNT, **4a**/MWNT, **4b**/MWNT and **4c**/MWNT were represented by grey, red, blue and green colours respectively. The figures are adapted from ref. [157] or **Paper III.**

6.6 *Post operando* assessments

For all metallopolymer functionalised electrodes, at least a 50% drop of activity was observed during CA. In order to assess the state of the metallopolymer functionalized films, *post operando* assessments were performed using CV and spectroscopy (very similar to what was described in **Chapters 4** and **5**) at 20 hours of CA.

The CV analysis showed a 70 – 90% drop of current density at –0.49 V *vs.* RHE for all metallopolymers (**Figure 6.5A,** for other metallopolymers**,** see ref. [157] or **Paper III** for more details). In parallel, UV-Vis spectra of the functionalized film showed the constant concentration of pyrene on the MWNT film for all metallopolymers (**Figure 6.5B ,** for other metallopolymers**,** see ref. [157] or **Paper III** for more details**)**. These observations were very similar to that of metallopolymers **3a–e** discussed in **Chapter 5**. The loss of current density strongly suggests that the diiron active sites are decomposed, while the UV-Vis spectroscopy revealed that the pyrene groups were retained on the electrode during CA. In short, this again demonstrated that active site remains the weak link for these metallopolymer functionalised electrode materials.

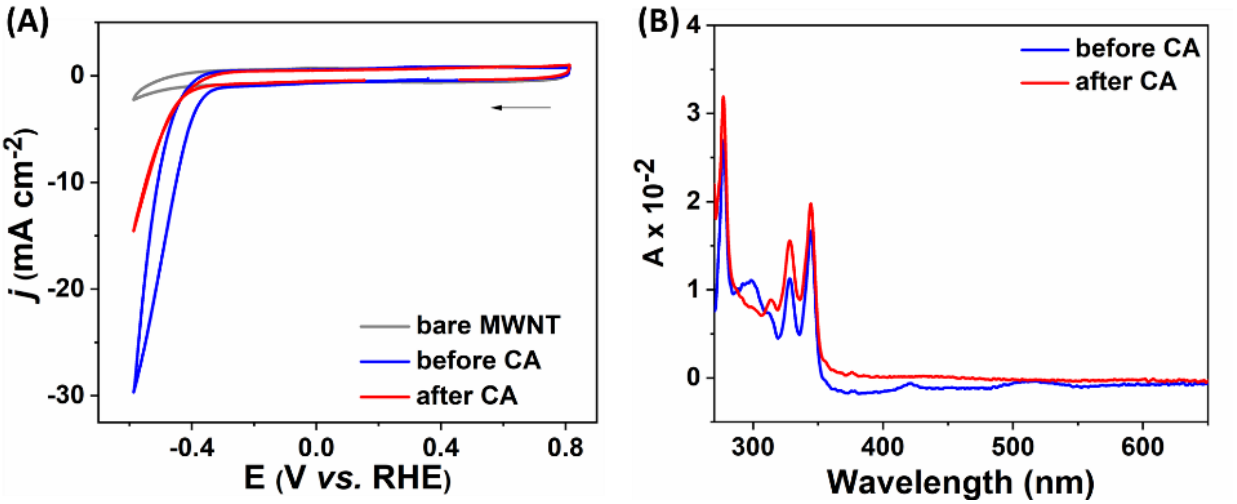

Figure 6.5: *Post operando* analysis of **4b**/MWNT using CV and UV-Visible spectroscopic analysis. (A) CV (v =100 mV s^{-1}); and (B) UV-Vis spectra, before (blue trace) and after CA (red trace). CV and CA were performed at in 0.2 M sodium phosphate buffer, pH 7 at room temperature. UV-Vis spectra were performed after desorbing the catalyst from the electrode in 3 mL DMF. The figures are adapted from ref. [157] or **Paper III.**

6.7 Discussion

The replacement of the naphthoquinone bridged $\{Fe_2(\mu\text{-}S_2)(CO)_6\}$ active site with a styrene based $\{Fe_2(\mu\text{-adt}')(CO)_6\}$ active site was successfully achieved. CV studies of **4a–c**/MWNT under aqueous condition showed impressive current densities. The CA of **4a–c/**MWNT showed that **4b** was the most active metallopolymer, reaching a TON_{H2} of ~10^5 with ~24% retention of initial current density. This was a marginal improvement in durability as compared to ~18% retention by the previously discussed metallopolymer, **3c** (see **Chapter 5)** after 20 hours of CA. The improved durability for **4b** was achieved at the expense of higher overpotential requirements (–0.39 V *vs.* RHE for **3a–e** *vs.*–0.49 V *vs*. RHE for **4a–c**) and about three times lower activity (TON_{H2} ~3.5 × 10^5 for **3c** and ~10^5 for **4b**) compared to metallopolymer **3c**. However, the current density achieved by metallopolymers **4b** and **4c** were found declining only during the first three hours of CA and became reasonably stable afterwards till the end of the experiments.

On a related note, the structurally similar $\{Fe_2(\mu\text{-adt}')(CO)_6\}$ (here, R = C_6H_4Br) complex immobilized in isolation on a graphite electrode was previously reported by Dey *et al.* to achieve a TON_{H2} of ~10^8 within 8 hours of CA at an overpotential of 480 mV.[115] In comparison, this implies that the polymer encapsulation might actually be detrimental to activity. However, Dey *et al.* used strong acidic condition (0.5 N H_2SO_4) as compared to the neutral pH employed by us, which complicates a direct comparison.

The reason for the initial loss of activity for **4a–c** during CA was most probably the decomposition of the diiron active site, although the exact degradation route was not identified in this study. Therefore, further studies and improvements of the metallopolymeric design are still necessary.

6.8 Summary

The work described in this Chapter, showed for the first time that an $\{Fe_2(\mu\text{-adt}')(CO)_6\}$ derivative could be successfully encapsulated inside a polymeric scaffold. The resulting metallopolymers were characterized using spectroscopy and electrochemistry. Two key insights obtained from this study are mentioned below:

1. The presence of a styrene group on the bridging ligand of the active site complex offers to use the diiron complexes as a monomer, and multiple active sites per polymer chain, unlike the metallopolymers **3a–e**.

2. Replacing the active site present in **3a –e** with a {Fe_2(μ-adt´)$(CO)_6$} derivative resulted in a small improvement in overall durability, combined with a substantial loss of activity and a requirement for higher overpotentials during CA.

Therefore, the objectives **c** mentioned in **Section 3.2** still remained to be fully accomplished. However, the metallopolymer approach remain a promising strategy as it offers to control the water solubility (by varying the ratio between DMAEMA and PyBMA), the active site density in the chain (by varying the active site ratio) and the immobilisation capability etc.

Chapter 7 : Paper IV – Synthesis and characterization of a semisynthetic [FeFe] hydrogenase

7.1 Brief introduction and motivation

So far, we have discussed isolated diiron complexes and their encapsulation inside polymeric scaffolds. Now it will be interesting to see the impact on a diiron complex when integrating it inside a protein scaffold. For that purpose, the protein scaffold of [FeFe] hydrogenase is an ideal choice as the latter was already engineered by Mother Nature. However, here I rather wanted to discuss the chemistry from a different perspective, and focus on the impact on [FeFe] hydrogenase (see **Section 1.5.1** for structural details) when modifying its active site. [FeFe] hydrogenases incorporating synthetic cofactors are often referred to as "Semisynthetic hydrogenases", as discussed in **Section 1.6**. As mentioned in the previously mentioned section, Lubitz *et al.* used the artificial maturation technique to activate the apo-HydA1 [FeFe] hydrogenase enzyme from *Cr* using a synthetic mono-cyanide variant of the native active site, *i.e.* $[Fe_2(\mu\text{-adt})(CO)_5(CN)]^-$ (complex **6**, **Figure 7.1B**). The authors demonstrated that replacing one CN ligand of the native cofactor present in [FeFe] hydrogenase yielded a semisynthetic hydrogenase that retained ~60% of wild type activity. However, a detailed characterization of the semisynthetic hydrogenase was not reported.[159]

When introducing a mono-cyanide variant of $[2Fe]_H$ (or $[2Fe]_H^{monoCN}$), several few key points remain to be understood. Firstly, incorporation of an asymmetric $[2Fe]_H^{monoCN}$ into the protein pocket can result in two different isomers (Isomer I and II, **Figure 7.1C**). To be specific, in Isomer I, the CN binding iron may reside at the distal position (Fe_d) relative to $[4Fe4S]_H$; while in Isomer II the CN binding iron resides at the proximal position (Fe_p) relative to $[4Fe4S]_H$. If one isomer forms predominantly inside the enzyme, and in that case which one was unknown. Secondly, the $[2Fe]_H^{monoCN}$ variant should have different electronic density at the diiron center compared to its native counterpart $[2Fe]_H$, and this should impact H^+/H_2 conversion activity and sensitivity towards gas inhibitors, *e.g.* CO and O_2. Thirdly, the initial report by Lubitz *et al.*[159] explored $[2Fe]_H^{monoCN}$ only in one protein scaffold, *i.e. Cr*hydA1. *Cr*HydA1 only contains the "H-cluster", but many [FeFe] hydrogenases, like *Dd*HyDAB, also features additional iron sulphur clusters ("F-cluster") and domains.[22] If the choice of scaffold protein influences the activity was also unknown.

7.2 Objective

The aforementioned possibilities motivated us to perform a detailed investigation on this mono-cyanide variant of native [FeFe] hydrogenases. For that, complex **6** was incorporated in two different [FeFe] hydrogenase scaffolds, *Cr*HydA1 and *Dd*HydAB (which contains two additional "F-clusters"). The resulting semisynthetic hydrogenases were characterised using solution assays, protein film electrochemistry, spectroscopy (infrared and EPR) and site directed mutagenesis. As a positive control, native *Cr*HydA1 and *Dd*HydAB were also produced through artificial maturation using $[Fe_2(\mu\text{-adt})(CO)_4(CN)_2]^{2-}$ (complex **5**, **Figure 7.1B**).

7.3 Synthesis

The synthesis of **5** and **6** were performed using previously reported protocols.[160,161] The apo forms of *Cr*HydA1 and *Dd*HydAB were isolated following heterologous expression in *E. coli*.[77] Subsequently, both apo-enzymes were activated using complex **5** and **6** through "artificial

maturation" [38] (see ref. [77] or **Paper IV** for more details), to give **5**-HydA1, **5**-HydAB, **6**-HydA1 and **6**-HydAB.

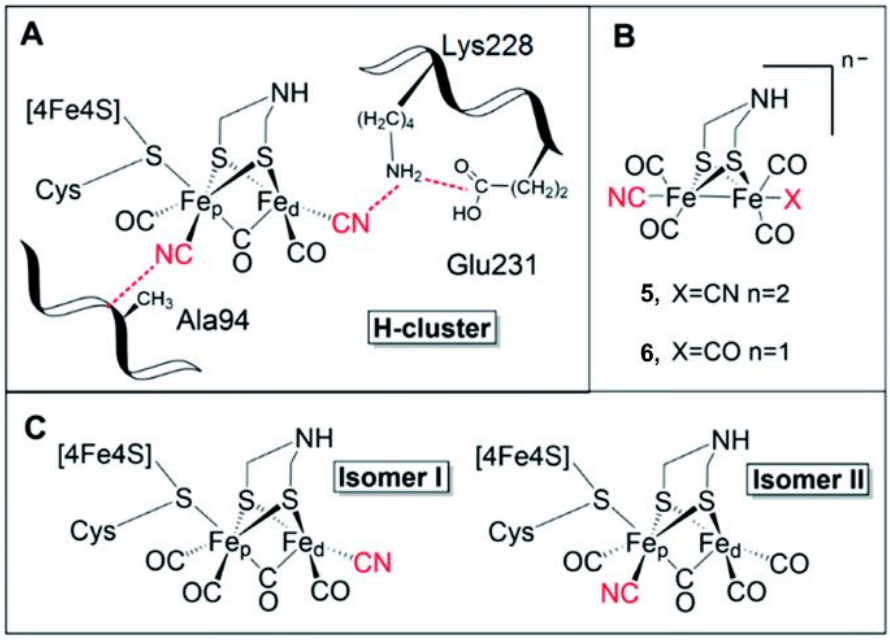

Figure 7.1: Schematic representation of (A) the active site of *Cr*HydA1 and its interaction with selected surrounding amino acid residues; (B) $[Fe_2(\mu\text{-adt})(CO)_4(CN)_2]^{2-}$ or complex **5** and $[Fe_2(\mu\text{-adt})(CO)_5(CN)]^{1-}$ or complex **6**; (C) possible isomers formed during maturation with complex **6** inside protein scaffold. This figure is adapted from ref. [77] or **Paper IV** with permission from Royal Society of Chemistry.

7.4 Characterisation

7.4.1 State of the active site inside host enzymes

The activated holo-enzymes *i.e.* **6**-HydA1 and **6**-HydAB were first characterized using infrared spectroscopy. **6**-HydAB showed one high energy band at 2057 cm^{-1} due to the CN ligand and four distinct bands at 1969, 1923,1903 and 1835 cm^{-1} due to the CO ligands present in the active site. The low energy CO band at 1835 cm^{-1} is most likely reflecting a CO ligand in a semi-bridging binding mode **(Figure 7.2A)**, as it is relatively higher in energy as compared to previously observed μCO bands for the native enzyme.[44]

The infrared spectrum of **6**-HydA1 displayed a similar shape, but the peak position of the low and high energy bands was found shifted up to 60 cm^{-1}, with bands at 2080, 1953, 1922, 1843, 1778 cm^{-1} **(Figure 7.2B)**. Two additional peaks were also detected at 2044 and 2013 cm^{-1} which are attributed to diiron complex nonspecifically bound to the enzyme scaffold (see ref. [77] or **Paper IV** for more details). The latter peaks were found light sensitive as they were selectively degraded while treating the enzyme with white light. Nevertheless, the spectrum of **6**-HydA1 was also in good agreement with the previous results reported by Lubitz *et al.*[159] Thus, infrared spectroscopy validated the successful incorporation of the $[2Fe]_H^{monoCN}$ into the enzymes with clear identification of the diatomic ligands bounds to the active site, forming a single isomer. These signatures represented the "as prepared state" of both host enzymes. A difference of 5-10 cm^{-1} for the low and high energy bands has previously been observed between the native counterparts (**5**–HydA1 and **5**–HydAB) in the same redox state.[44] Thus, the large difference in peak positions between **6**–HydA1 and **6**–HydAB indicates accumulation of two different redox states in their "as prepared states".

Treating the "as prepared" form of **6**-HydA1 and **6**-HydAB with a reductant (10 mM sodium dithionate, NaDT, E^0 = –660 mV *vs.* SHE at pH 7) revealed contrasting behavior. **6**-HydA1 showed an unexpected hypsochromic shift between 1–12 cm^{-1}. **6**-HydAB appeared rather unreactive under equivalent reducing conditions, and partially reduced to show a bathochromic shift with

additional features appearing at 1956, 1928 and 1884 cm^{-1} **(Figure7)**. Treating **6**-HydAB with a stronger reducing agents Eu-DTPA (E^0 = –1.09 V *vs.* SHE at pH 7, DTPA = diethylenetriaminepentaacetic acid) still only resulted in a partial reaction of the "as prepared state", but caused a hypochromic shift like **6**-HydA1 (see ref. [77] or **Paper IV** for more details). Such unusual behavior could not be explained yet with clarity, but may point towards a singly or doubly reduced state in the "as prepared state", which would be consistent with the low energy CN (2057 cm^{-1}) and bridging CO (1778 cm^{-1}) bands in **6**-HydAB and **6**-HyDA1 respectively.

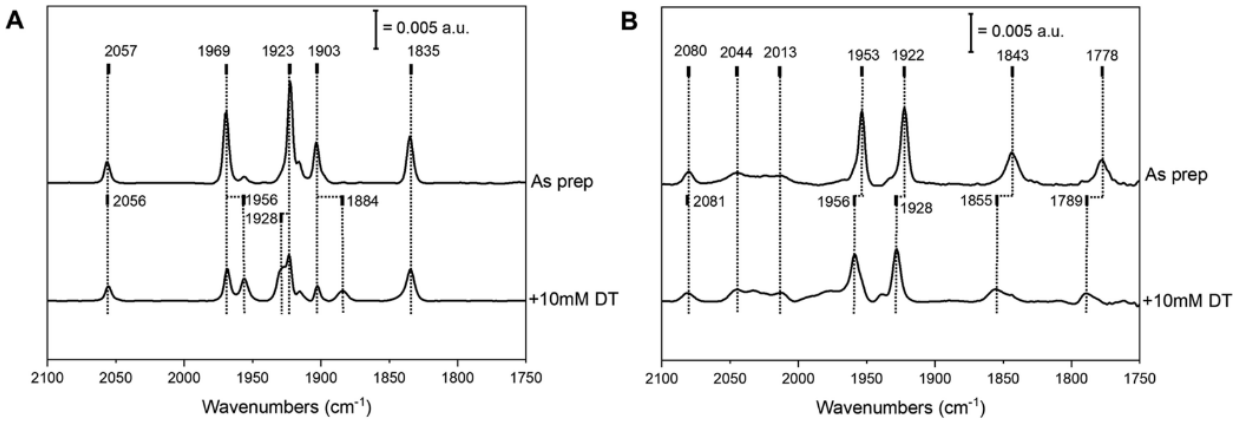

Figure 7.2: Infrared spectra of semisynthetic hydrogenases in the as prepared state (top) and after treating with reducing reagent, *i.e.* 10 mM sodium dithionate (NaDT), in a transmission cell in pH 8 buffer. (A) **6**-HyDAB (B) **6**-HyDA1. The trace for the as prepared state of **6**-HyDA1 was obtained by white light treatment. The dotted line marks the most prominent bands. The spectra were recorded at room temperature. The figure is adapted from ref. [77] or **Paper IV** with permission from Royal Society of Chemistry.

Hence, EPR spectroscopy was employed to characterise the oxidation state of the active site inside the host enzymes under cryogenic conditions (temp. =10 K). EPR spectra of **6**-HydA1 in its "as prepared state" showed two rhombic signals which indicates the presence of two different states. Based on the properties of the signals, they likely arise from "super reduced states" (sred) of the "H-cluster", *i.e.* $[4Fe4S]_H^{1+}$- $[Fe^{(I)}Fe^{(I)}]_H$. The observation of two states at low temperature, while infrared spectroscopy only indicates one, hints at the possible stabilization of different rotamers under cryogenic condition (see below). In contrast, as prepared **6**-HydAB was EPR silent which could be explained by accumulation of an $\mathbf{H_{red}H^+}$ like state *i.e*. $[4Fe4S]_H^{2+}$- $[Fe^{(I)}Fe^{(I)}]_H$. This is also in line with the low energy CN band (2057 cm^{-1}) observed in infrared spectroscopy discussed earlier (see ref. [77] or **Paper IV** for more details).

7.4.2 Identification of possible isomers

Infrared spectroscopy of both semisynthetic hydrogenases (**6**-HydA1 and **6**-HydAB) clearly indicates the formation of a single (dominant) product or isomer despite at least two possibilities **(Figure 7.1C)**. To identify the isomer formed, site directed mutagenesis was employed targeting A94S (alanine at the 94th position was replaced by serine) in *Cr*HydA1 (called $HydA1^{A94S}$). The choice of amino acid variant was motivated by the fact that the A94 residue (in *Cr*HydA1) is known to interact with pCN (CN bound to Fe_p). Replacing amino acid A94 should consequently cause an interruption in that interaction only if Isomer II forms predominantly **(Figure 6.1 A)**. Indeed, as prepared **6**-$HydA1^{A94S}$ showed distinct changes in its infrared signatures, relative to **6**-HydA1, with red shifts of the CN band by 20 cm^{-1} and CO bands by 3 – 5 cm^{-1} **(Figure 7.3).** A similar observation was reported for the same A94S variant of the native counterpart or **5**-HydA1.[162] Thus, site directed mutagenesis coupled with infrared spectroscopy strongly support Isomer II as the predominant form of the active site **(Figure 7.1C)**.

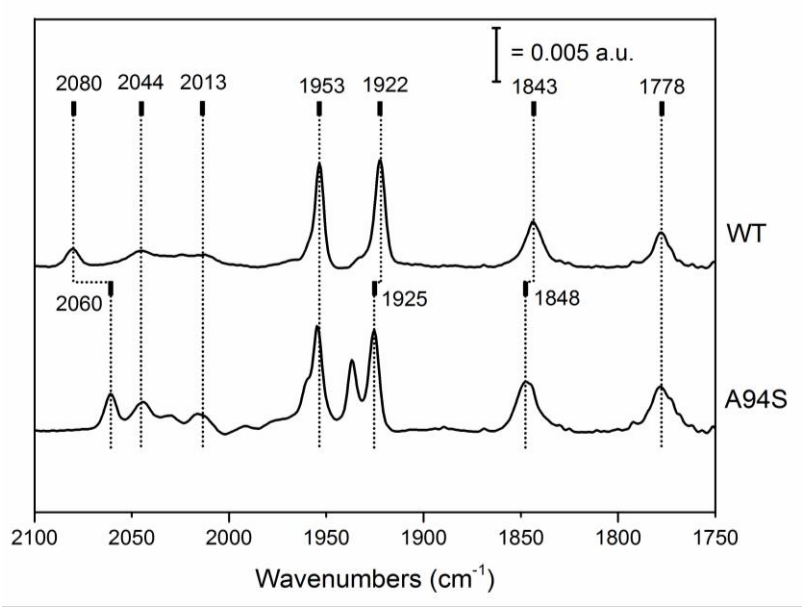

Figure 7.3: Effect of A94S mutation on infrared spectra (ATR mode) of **6**-HydA1. The dotted line represents most prominent bands. The spectra were recorded at room temperature. The figure is adopted from ref. [77] or **Paper IV** with permission from Royal Society of Chemistry.

7.4.3 Activity

The mono-cyanide variant or complex **6** contain less over all charge and electron density at the diiron centres than the dicyanide active site or complex **5** present in native hydrogenase.[160] These changes in electronic properties should be reflected in the redox potential and catalytic activity of the semisynthetic hydrogenase. Solution assays of **6**-HydA1 for H_2 evolution was performed, showing a specific activity of 223± 25 µmol of H_2 mg protein^{-1} min^{-1}, corresponding to ~60% residual activity relative to **5**-HydA1. The observed specific activity matches well with the results reported by Lubitz *et al.*[76] In contrast, **6**-HydAB displayed very poor activity, retaining ~2% of the specific activity compared to **5**-HydAB.

CV traces recorded of protein films of **6**-HydA1 on a rotating disc pyrolytic graphite electrode showed a bidirectional signature with low overpotential requirements like native *Cr*HydA1 **(Figure 7.4)**. The ratio of the oxidative and reductive currents at 100 mV overpotential (i_{ox}/i_{red} ~1.6) suggest that **6**-HydA1 has a slight bias towards H_2 oxidation over H_2 production, similar to what has previously been reported for the native enzyme (**5**-HydA1) (see ref. [77] or **Paper IV** for more details).

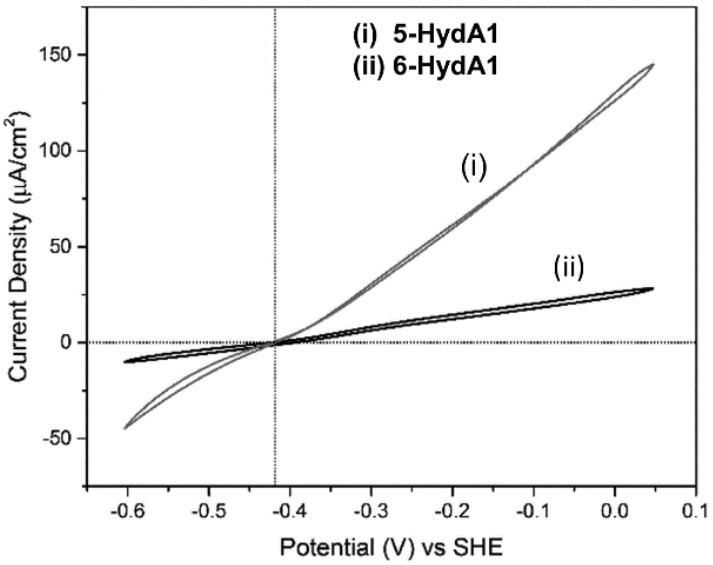

Figure 7.4: CV using Protein film electrochemistry (PFE) of **5**–HydA1 and **6**–HydA1 drop casted on rotating disc pyrolytic graphite electrodes in pH 7 buffer under 1 atm of H_2 gas. (v = 10 mV s^{-1}, temp. = 303 K, rotation rate = 3000 rpm). The vertical line represents the thermodynamic potential for H^+/H_2 conversion in pH 7. The figure is reproduced from ref. [77] or **Paper IV** with permission from Royal Society of Chemistry.

7.4.4 Sensitivity against O_2 and CO

Both **6**-HydA1and **6**-HydAB showed remarkable tolerance against CO. These results are striking as CO is well known as a competitive inhibitor of native [FeFe] hydrogenases and reacts to yield **H_{ox}-CO** state (see **Section 1.5.1.3**).[163] The possibility of the "as prepared state" already being accumulated with **H_{ox}-CO** state during preparation, was ruled out by monitoring the evolution of CO gas during maturation. Additionally, flushing **6**-HydAB with N_2 for 48 hours caused no changes in the infrared spectrum, as would be expected if the active site released an extra CO ligand (see ref. [77] or **Paper IV** for more details).

In addition to being unusually CO tolerant, the semisynthetic hydrogenase **6**-HydAB showed considerable tolerance against atmospheric oxygen as compared to the native enzyme (**5**-HydAB). This oxygen tolerance was validated by infrared spectroscopy showing ~45% retention of IR peak intensity after 30 min of incubation under air, as compared ~16% retention after 5 min for **5**-HydAB. In contrast, **6**-HydA1 was found O_2 sensitive as it loses all infrared signatures, present in the "as prepared state" within 5 min of exposure to atmospheric O_2 and showed appearance of three new bands (2097, 2024, 1985 cm^{-1}) correlated to an air-induced state called **H_{air}-ox** [51] (see ref. [77] or **Paper IV** for more details). Thus, the protein scaffolds around the active sites have considerable impacts on O_2 tolerance.

7.5 Discussion

Integration of a mono-cyanide variant of the native [FeFe] hydrogenase cofactor gave rise to semi-synthetic enzymes with very different properties depending on the hydrogenase scaffold. As **6**-HydA1 and **6**-HydAB appeared to stabilise different redox states and had distinctly different activities.

The unsymmetrical nature of the mono-cyanide complex could potentially give rise to different isomers of the "H-cluster". EPR spectra, collected at cryogenic temperature clearly showcased two different "H-cluster" species in **6**-HydA1. In contrast, infrared spectroscopy suggested the presence of one form or state of the "H-cluster" in the "as prepared" samples of **6**-HydA1. We proposed that the different results between the two methods is attributable to the temperature at which the data is collected. The EPR spectra were recorded at cryogenic temperatures, while the infrared spectroscopy was performed with room temperature samples. Thus, we could possibly have different rotamers of the diiron complex present, and the interconversion between them is then rapid enough to average out the signal(s) at room temperature, while the EPR temperatures

ensures “rotation lock” conditions for **6**-HydA1. As the as prepared **6**-HydAB samples were EPR silent we do not know if the same type of chemistry occurs also in this scaffold. Infrared spectroscopy coupled with site directed mutagenesis validated a predominant formation of Isomer II in **6**-HydA1, which results in a loss of the K228-dCN interaction (Lysine 228, *Cr*HydA1 numbering, see ref. [77] or **Paper IV** for more details). The contrasting observations between EPR and infrared spectra could be explained by the fact that at room temperature Fe_d from **6**-HydA1 (and possibly **6**-HydAB) achieve more rotational freedom with loss of the K228-dCN interaction and thus show a single signal or averaged signal.
K228 has been proposed to play an important role in forcing the Fe_d to rotate and create an open coordination at Fe_d in the apical position, via a K228 –dCN interaction **(Figure 7.1A)**.[164] This could explain the activity for **6**-HydAB. The loss of the corresponding K228-dCN interaction in **6**-HyDAB causes the shift of one of the bound CO ligands to the apical position, thus blocking the open coordination site at Fe_d. Therefore **6**-HydAB displayed limited reactivity towards CO, H_2 or H^+ and O_2. On the other hand, **6**–HydA1 still showed decent activities despite loss of the K228-dCN interaction, which proves that the latter interaction is in fact not crucial for *Cr*HydA1. Such differences in results for two different protein scaffolds activated with the same cofactor indicates that the protein scaffold has substantial influence on the activity and sensitivity.

In addition to the structural factors discussed above, the decreased sensitivity towards CO and O_2 in these semisynthetic hydrogenases could be partially attributed to the decreased electron density at the Fe centre on switching from complex **5** to **6**. This is due to the fact that replacement of a relatively strong σ donating and poor π accepting CN ligand with a relatively poor σ donating and strong π accepting CO ligand cause a relative electron deficiency at the metal centre in complex **6**. Still, a particularly striking finding in this study, was the observation that **6**-HydA1 retained the capacity for catalysis at small overpotential, despite the change of a CN to CO ligand.

7.6 Summary

In summary, the work presented in this Chapter outlines that the active site pocket of [FeFe] hydrogenase enzyme is capable of promoting high activities also from non-native cofactors. A few key insights achieved from the study are as a follow:

1. Varying the primary coordination sphere of $[2Fe]_H$ does not necessarily result in a lost capacity for reversible catalysis.
2. The protein scaffold around the active site has substantial impact on activity and sensitivity of the semi-synthetic hydrogenases.
3. Introducing asymmetry by replacing one CN ligand of $[2Fe]_H$ with a CO ligand, results predominantly in the formation of the isomer with a CN ligand on Fe_p.
4. Varying the primary coordination sphere turned out to be a possible tool for improving resistance towards potential inhibitors like O_2 and CO with an expense of substantial loss in activity.

This study identifies a possible parameter that could be tuned to make oxygen tolerant semisynthetic hydrogenase. From a catalyst design perspective, this study is fascinating. It showed that replacing CN with CO has a substantial impact on activity, but at least one semisynthetic hydrogenase could still show decent bidirectional catalysis rates with negligible overpotential requirements. Both semi-synthetic hydrogenases were also less sensitive towards CO inhibition, and one particular protein scaffold also had a positive impact on oxygen tolerance. The latter point that highly specific interactions between active site and secondary coordination sphere are necessary to convert an oxygen sensitive material into oxygen tolerant.

Chapter 8 : Part of Paper II – Life Cycle Assessments of the bioinspired electrode materials for H_2 production

8.1 Brief introduction and motivation

In eSCALED project, the overall goal of the project was not only to develop a device and evaluate its efficiency for generation of fuel or chemicals (H_2 or reduced CO_2–based product) but also to define its environmental footprint as mentioned in **Section 2.1**. As mentioned in **Section 1.8**, Life Cycle Assessment (LCA) has been recognized as the most distinguished methodology to understand and quantify the environmental profile of a product, material, process or system.

This study was split among ESRs (early stage researchers) based on different part of the devices (see **Section 2.1** for the details of the device), proposed under eSCALED project. For example, the LCA studies of the anode (for water oxidation), cathode (for CO_2 reduction), photo-voltaic cell (converting solar energy into electricity), proton exchanging membrane (for transferring H^+ selectively from anode to cathode) were performed by Andrew Howe (ESR 1), Domenico Grammatico (ESR 6), Olivera Vukovic(ESR 9) and Karell Bosson (ESR 7), respectively. The cathode material for H_2 production was studied by myself (ESR 4). Finally, the LCA of overall device should be studied by Bruno Branco (ESR 12).

As discussed in **Chapter 4, 5** and **6**, metallopolymer **3c** ranked first place among the synthesised catalysts (**2**, **3a-e**, **4a-c**) for electrochemical H_2 evolution while immobilized onto MWNT. It is now important to evaluate the sustainability of aforementioned catalysts functionalised electrode. Analysing the environmental profile allowed to understanding the balance between the environmental impact and the H_2 generation by the system (electrode material).

8.2 Objective

Thus, the objective of this study was to study the LCA of synthesised electrode materials for hydrogen evolution reaction (HER). For that, three synthesised catalysts *i.e.* **2** (contains pyrene deprived of polymeric scaffold), **3a** (contains polymeric scaffold deprived of pyrene) **3c** (contains polymeric scaffold with pyrene) were chosen based on their structural distinction **(Figure 8.1)**. Their LCA were assessed at two stages towards H_2 production *i.e.* (i) synthesis and (ii)electrocatalytic H_2 evolution while immobilized on MWNT. Finally, the best system among the previously mentioned three electrode materials was chosen on the merit of environments footprint and identified. Subsequently, the culprit that cause most contribution towards environmental impact during H_2 production was identified.

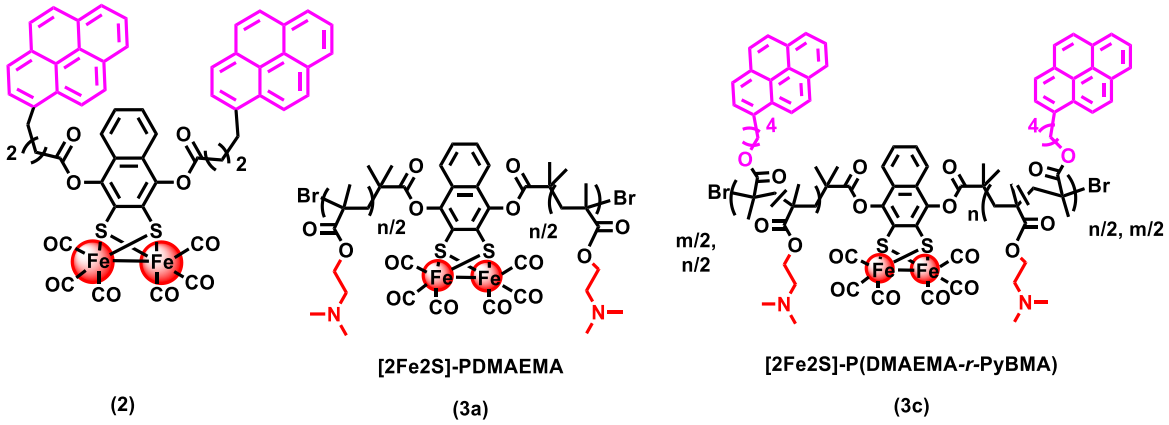

Figure 8.1: Schematic representation of catalysts studied under LCA. Catalysts are complex **2** (left), metallopolymers **3a** (middle) and **3c** (right).

8.3 Characterization

As explained in ISO 14040:2006 and ISO 14044:2006 (discussed in **Section 1.8**), LCA involves step by step process *i.e.* (i) Goal and scope;(ii) Life cycle inventory (LCI); (iii) Impact categories; and (iv) Interpretation, to meet objective. The details of each step and their respective importance were also explained in **Section 1.8**. Here, the exact implementation of previously mentioned steps to meet the objective were discussed.

8.3.1 Goal, scope and targeted audience

8.3.1.1 Goal and scope

As discussed in **Section 8.2**, the goal or objective of the analysis was to compare environmental footprint for hydrogen production by three of the synthesised catalysts **(2**, **3a,** and **3c**) while immobilised on electrode and finally the material (*i.e.* electrode, catalyst, electrolyte) causing highest environmental demands during H_2 production would be identified.

(a) System boundary

As we know, ´system boundary´ covers the all steps starting from the extraction of raw materials and usage of energy from nature and finish with end of life cycle of product with waste management and recyclability and this entire journey is called “cradle to grave”. However, in this study, a “cradle to gate” approach which excluded “application phase of produced electrode material in the device and their recycling after use” as this study was done at early stage of project and device was under preparation by then. Instead, an electrochemical H_2 production was considered as “application phase” as a proof of concept and LCA was analysed accordingly **(Figure 8.2)**.

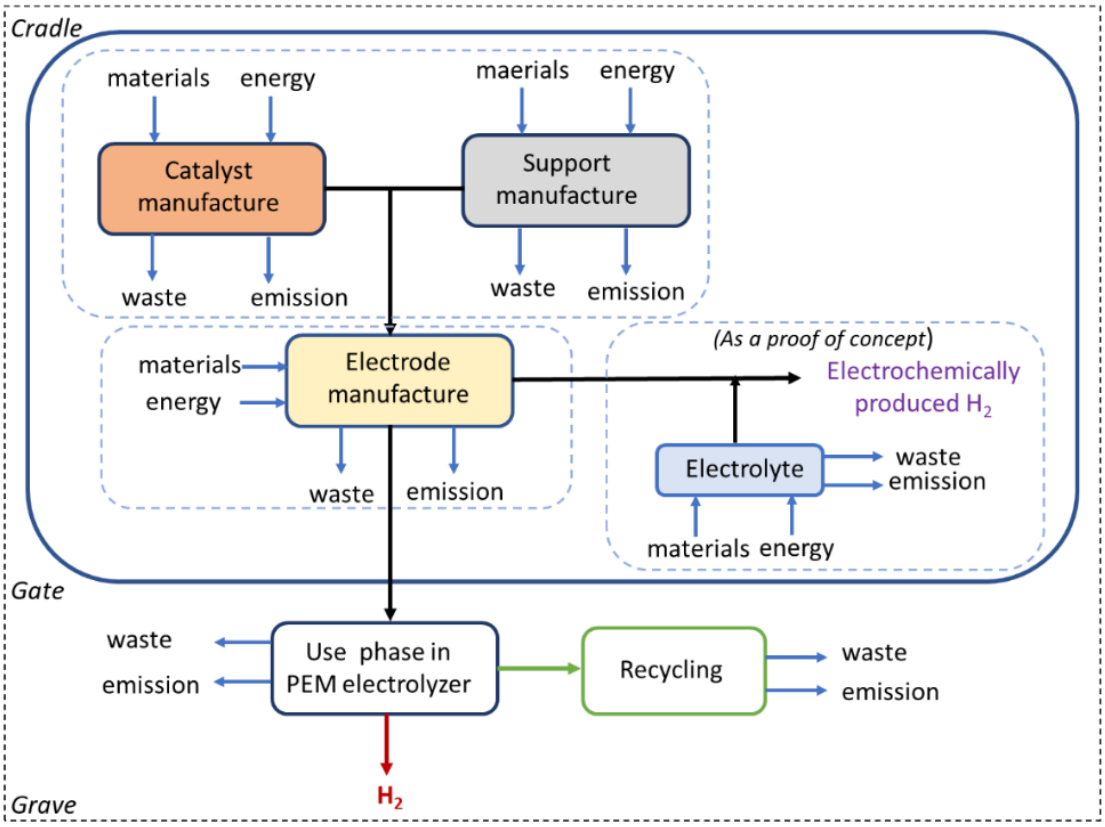

Figure 8.2: System boundary for life cycle assessment for all catalysts. The figure is adopted from ref.[135] or **Paper II** with permission from American Chemical Society.

(b) Functional Unit

LCA was planned to be performed at two different stages in process of electrochemical hydrogen production, *i.e*. (i) manufacture of catalysts (**3a**, **3c** and **2**) and (ii) electrochemical H_2 production by electrodes functionalized with prepared catalysts. Therefore, ´Functional unit´ for aforementioned systems were defined as 1 kg of catalyst production and 1 kg of H_2 production by **catalyst**/MWNT (surface area, A = 0.2 cm^2) for stage (i) and (ii) respectively **(Figure 8.3)**.'

(a) Targeted audience

LCA also allowed to specify the range of audience with whom the study intended to be shared. The targeted audience should be primarily the in the eSCALED project, governmental and legislative bodies such as the European Commission (EC), academic partners and private commercial beneficiaries that are involved with the eSCALED consortium, scientific community associated with renewable energy followed the general non-scientific audience across the Europe.

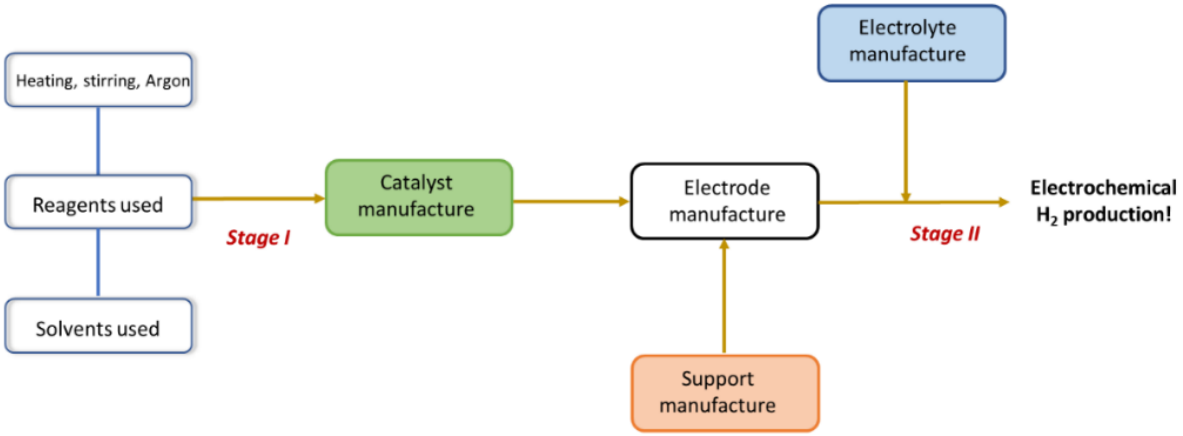

Figure 8.3: Flow chart of LCA towards electrochemical H_2 production by synthesised cathode materials. The figure is adopted from ref [135] **Paper II** with permission from American Chemical Society.

8.3.2 Life cycle inventory (LCI)

LCI includes chemicals, energy consumed and waste generated during the synthesis of each catalysts (**2**, **3a** and **3c**). The primary data for LCI was collected from experimental details (synthesis, electrochemical H_2 production) of the catalysts discussed in **Chapter 4** and **5** and **Table 8.1**. (for more details see ref. [135] or **Paper II**).

8.3.2.1 Quality of the data

The used reagents throughout synthesis and application stage of the catalysts were included to inventory using secondary database called "Ecoinvent database version 3.0.1.0". Since some of the used reagents were not present in previous mentioned database, they were manually included to the database followed by inventory based on reported literatures and patents for respective reagents. For example, CuBr[165], Sodium cyanoborohydride ($NaBH_3CN$),[166] Methacrolyl chloride,[167] Superhydride solution,[168] DMAEMA,[169] Iron pentacarbonyl[170], and MWNT[171] (for more details see ref. [135] or **Paper II**).

8.3.2.2 Cut-off criteria

This LCA study did not develop any cut-off based on mass or energy, or environmental relevance except the energy consumption for spectroscopic characterization steps of each synthetically produced material throughout the analysis.

8.3.2.3 Allocation procedures

All of the data were collected and included in the inventory analysis are allocated by mass (for more details see **Table 8.1** and ref. [135] or **Paper II**).

Table 8.1: Inventory used for performing LCA for MWNT synthesis and electrochemical H_2 production by **catalyst/MWNT** (A =0.2 cm^2). The table was adopted from ref. [135] or **Paper II** with permission from American Chemical Society.

System	Chemical/process used	Mass or volume or energy consumed	unit	Product (H_2 or MWNT) yield (µg)
3a/MWNT	MWNT suspension	0.06	mg	45.2[a]
	3a	0.3	mg	
	DMF	37.76	mg	
	Buffer	20	mL	
	Stirring plate	0.0018	kWh	
3c/MWNT	MWNT suspension	0.06	mg	229.8[a]
	3c	0.3	mg	
	DMF	37.76	mg	
	Buffer	20	mL	
	Stirring plate	0.0024	kWh	
2/MWNT	MWNT suspension	0.06	mg	40.2[a]
	2	0.075	mg	
	DMF	37.76	mg	
	Buffer	20	mL	
	Stirring plate	0.0024	kWh	
MWNT	Molybdenum hexacarbonyl	0.01	g	22500[b]
	Ferrocene	0.02	g	
	Quartz sheet	0.32	g	
	Oxygen	298.08	g	
	H_2	35.95	g	
	Methane	1839.6	g	
	Energy	16.87	kWh	

N_2 or Argon used throughout the processes are assumed to recycled during industrial system and energy consumes for recycling is included. Buffer = 0.2 M sodium phosphate buff pH 7, [a]H_2, [b]MWNT.

8.3.3 Impact categories

Life cycle impact was assessed based on selected environmental categories as per the ReCIPE 2016 Midpoint (H) method[134]. For the total energy demand quantification (*i.e.* total energy consumed during entire life cycle), the cumulative energy demand (CED) method (2018, v1.10.) was also used.[133] Within this method, seven categories mentioned are selected in way that it covers environment impact for air, soil, waters and human health. The categories are (i) Global warming; (ii) Terrestrial acidification; (iii) Freshwater eutrophication; (iv) Terrestrial ecotoxicity; (v) Human carcinogenic toxicity; (vi) Mineral resource scarcity; and (vii) Fossil resource scarcity. For the exact definition were each impact category, see **Section 1.8**.

8.3.4 Interpretation

Once inventories for synthesized materials (catalysts or H_2) were included to "Simapro software", they were scaled up to the functional unit (1 kg of catalyst and 1 kg of H_2 production by catalyst functionalized electrode of A= 0.2 cm^2, in our case) and subsequently their respective impacts were analysed by the same software and shown in **Figure 8.4** and **8.5**. For the readers that do not have a LCA background, the simplest way to read the aforementioned figures is that – in each

category, the maximum impact contributing system is considered as 100% and the rest of system is compared relative to that.

8.3.4.1 LCA for 1kg of catalysts (2, 3a and 3c) production

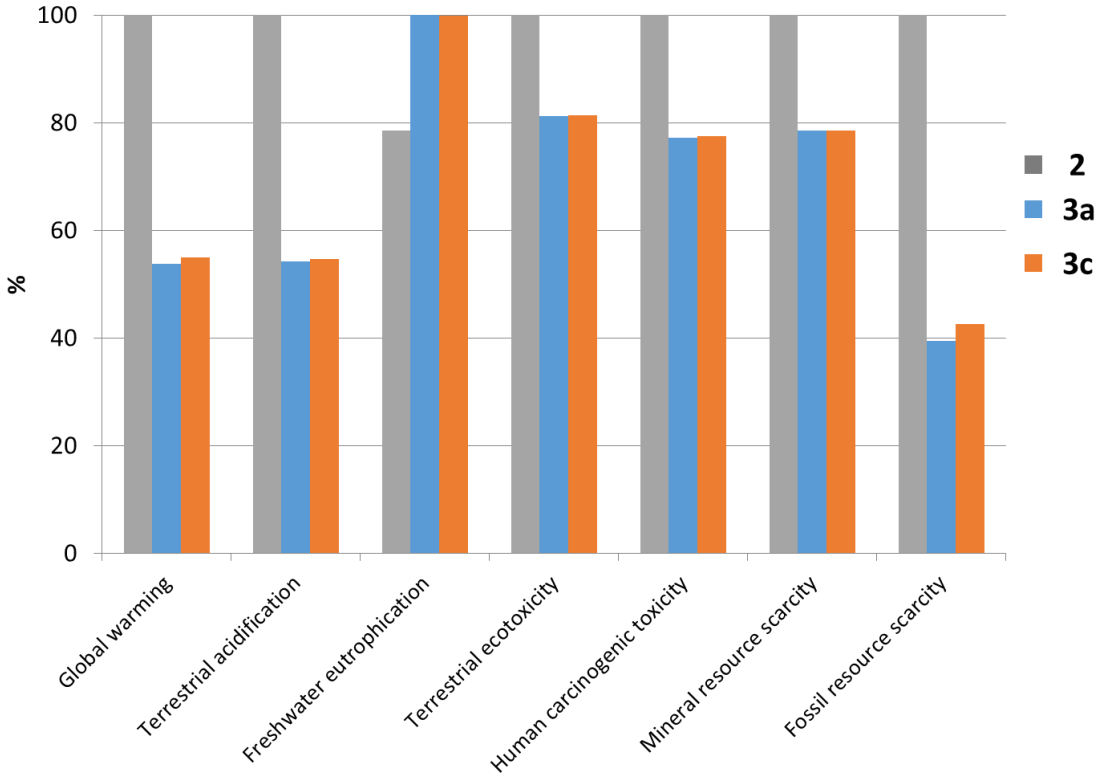

Figure 8.4: Comparison of life cycle assessment (LCA) for 1 kg of catalyst **(2, 3a** and **3c**) production using "RECIPE 2016 Midpoint (H) method". Here, **2, 3a** and **3c** were marked by grey, blue and orange colours respectively. The figure is adopted from ref [135] or **Paper II** with permission from American Chemical Society.

Comparative assessment for 1 kg of catalyst production for **3a**, **3c** and **2**, revealed both metallopolymers (**3a** and **3c**) showed about 25 –90% lesser impacts than that of for **2** in six out of the seven selected categories **(Figure 8.4)**. Detailed interpretation for the each individual catalyst revealed that relatively high amount of complex **1** and solvents used during production of **2** causes such high demands for complex **2** (for details, follow ref [135] or **Paper II)**. For both metallopolymers *i.e.* **3a** and **3c**, amine containing monomer DMAEMA was the most demanding.[135] Thus, metallopolymers (**3a**, **3c**) outperformed the complex **2**, in term of environmental demand at manufacturing stage.

8.3.4.2 LCA of 1 kg of electrochemical H_2 production

Similarly, Comparative assessment for 1 kg of H_2 production by functionalised electrode materials (A = 0.2 cm^2) demonstrated that, **3c**/MWNT and **3a**/MWNT showed ~80% and ~10% lesser environmental demand than that of complex **2**/MWNT in all categories, respectively **(Figure 8.5)**. These results were expected as both metallopolymers outperformed diiron complex **2**, both in production (discussed in previous section) and application (~18 and ~70 times higher TON_{H2} by **3a** and **3c,** see **Chapter 3 –5** for more details) stages.

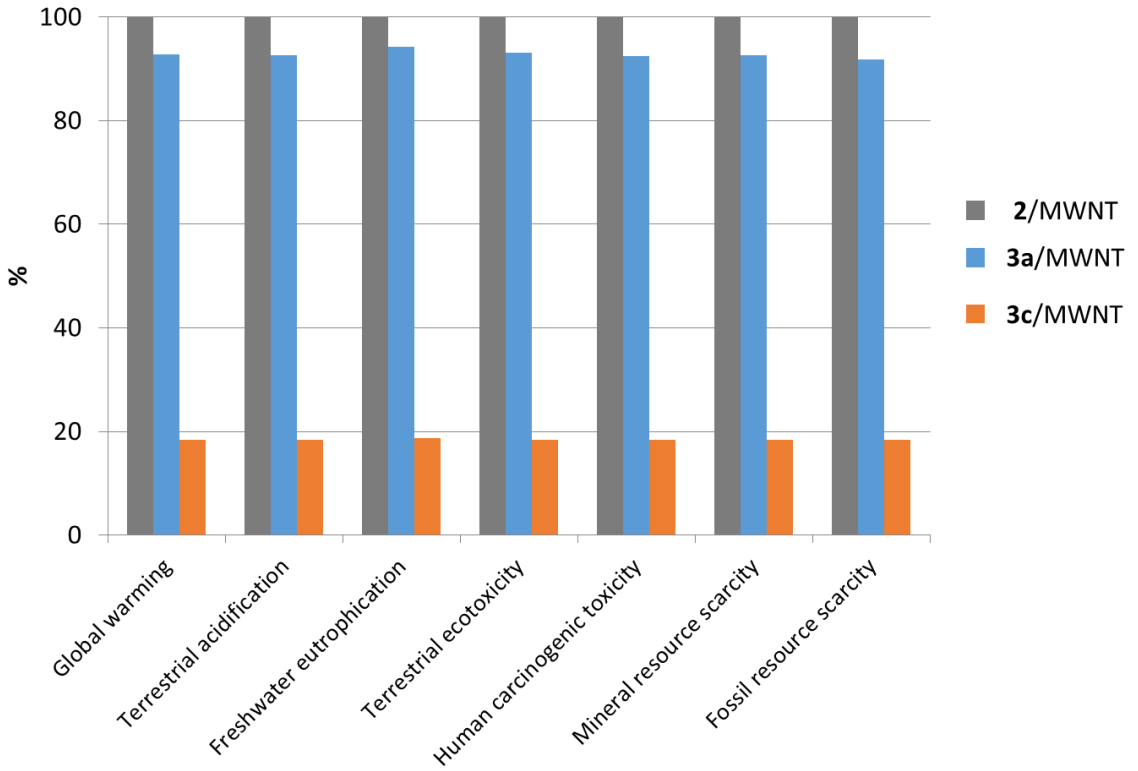

Figure 8.5: Comparison of LCA for 1kg of H_2 production for catalysts **(2, 3a** and **3c**) functionalised MWNT of 0.2 cm^2 of surface area using "RECIPE 2016 Midpoint (H) method"[134]. Here, **2**/MWNT, **3a**/MWNT**, 3c**/MWNT were marked by grey, blue and orange colours respectively. The figure is adopted from ref [135] or **Paper II** with permission from American Chemical Society.

Individual interpretation for each functionalised electrode material revealed that the main and common culprit was MWNT as latter causes more than ~95% environmental impact during hydrogen production.[135] Further detailed assessments for MWNT, revealed that latter consumes extremely high amount of energy due to heating and inert gases (it is converted into energy used during recycling of inert gas, for inventory) during synthesis[171] considering impact accounted for small quantity of product (for LCA details of MWNT, see ref. [135] or **Paper II**).[171] Thus the polymer-based catalyst **3c** stands out to be the best catalysts among them both in term of activities and respective environmental demand for synthesis and application stage.

8.4 Discussion

Electrochemical assessments showed the "metallopolymer approach" is superior than isolated active site by a clear margin (see **Chapter 4, 5**). Now, LCA put a "cherry on top" by revealing that "metallopolymeric approach" is more sustainable for catalysis than that with sole complex. Among metallopolymers, inclusion of pyrene (*i.e.* **3c**) added a positive environmental footprint as **3c** was much more durable on MWNT and consequently productive than **3a** (metallopolymer deprived of pyrene) during catalysis. Though LCA was performed at laboratory scale which might underestimate the assessment, it is still a promising aspect to give a completeness to the characterisation of a materials.

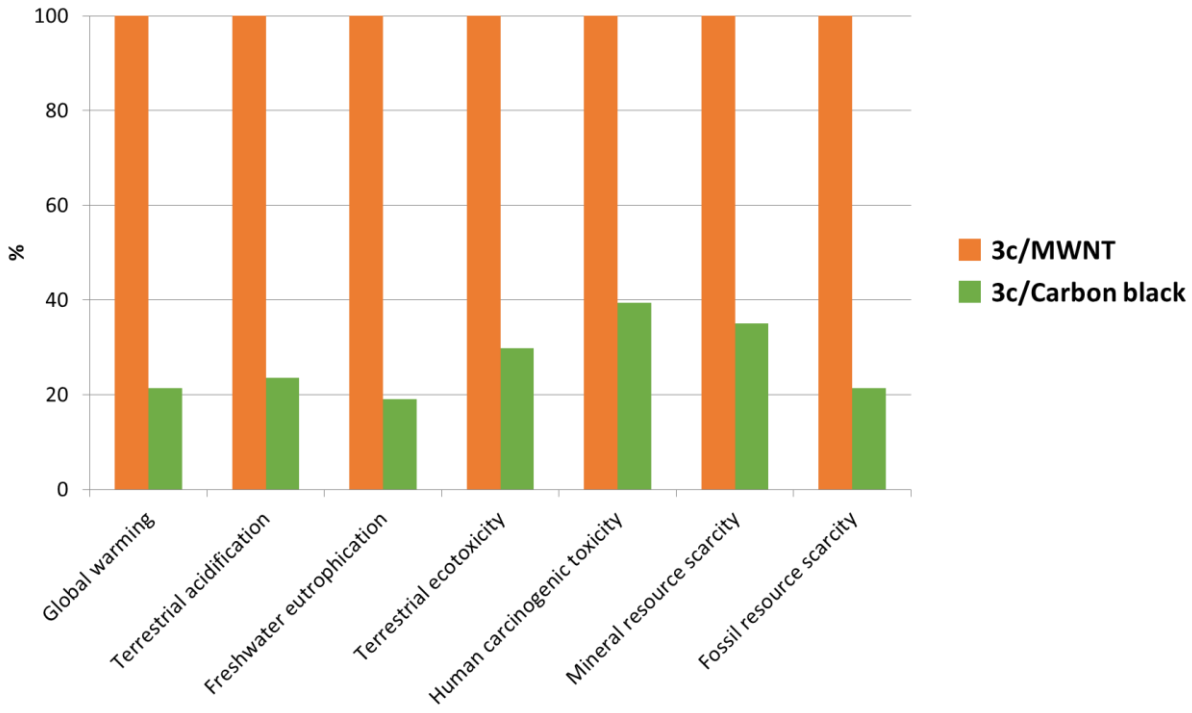

Figure 8.6: Comparison of LCA for 1 kg of H_2 production by **3c** functionalised MWNT (orange trace) and carbon black (green trace) (A= 0.2 cm^2) using "RECIPE 2016 Midpoint (H) method"[134]. The figure is adopted from ref [135] or **Paper II** with permission from American Chemical Society.

In addition, the common culprit *i.e.* MWNT revealed through LCA, should be replaced with equivalent electrode ink having low impact in order to minimize the environmental demand. For that LCA was performed hypothetically by replacing MWNT with carbon black[172], a well-known allotrope of carbon and used as an electrode ink as well. The experimental data (ink preparation, catalyst loading, H_2 production properties) for **catalyst**/carbon black (catalysts immobilized on carbon black) was not available. Therefore, it was postulated that the same amount of carbon black as MWNT, should be required to obtain equal amount of hydrogen production by immobilizing catalyst onto it. The assumption could be supported by the fact that both MWNT (density, d ~1.7–2.2 g cm^{-3}, specific surface areas, SSA =22 –1670 m^2 g^{-1})[173] and carbon black (d ~1.8 – 2.18 g cm^{-3}, SSA= 8 –1000 m^2 g^{-1})[172] have analogues density, specific surface area (SSA depends on quality of the pigment grade). Interestingly, nearly 60 to 80% drop in the impact for equivalent amount of H_2 production was noticed, when using carbon black as electrode material **(Figure 8.6)**. The drop of environmental demand on switching from MWNT to carbon black is attributed to relatively low impact (< 5%) of carbon black compared to MWNT. It is noteworthy to mention that the catalysis depends on loading or quantum of π-π interactions between electrode and catalysts. MWNT is superior than carbon black in term of capacity of π-π interactions which makes this assumption weaker.

8.5 Summary

Over all, LCA of prepared bioinspired cathode materials were analysed. Despite the fact that the LCA study was performed at laboratory scale in a very low TRL, prospective way to perform it has allowed to identify two key aspects:

1. Encapsulation of active sites macromolecular scaffolds was synthetically and catalytically more sustainable than isolated active sites.
2. MWNT were identified as common drawback for the catalysts functionalised electrode materials as they demand a high amount of energy consumption for their production and should be replaced with equivalent electrode ink having a low demand (*i.e.* carbon black).

Thus, LCA allowed to identify the environmental hotspots and ways to improve the synthesised materials at this early stage of development. This also allowed to meet the last objective (*i.e.* objective **d** or evaluation environmental footprint) mentioned in **Section 3.1**. Overall, the LCA study remains highly promising and important for improvising a method or system in order to balance between its catalytic turnover and environmental demand. I believe, it will be a compulsory assessment for developing any materials in near future.

Chapter 9: Overall Summary and outlook

Hydrogenase enzymes were first discovered in the 1930s.[18] The synthesis of $\{Fe_2(\mu\text{-}S_2)(CO)_6\}$ was first reported in 1928 without any information of [FeFe] hydrogenases.[174] The first crystal structure of [FeFe] hydrogenases was reported in 1990s[20] which triggered the development of bioinspired catalysis based on the $\{Fe_2(\mu\text{-}S_2)(CO)_6\}$ core due to its structural similarities with the $[2Fe]_H$ cofactor.[19,91] Yet, it remains a highly active research field with continued efforts to find the optimum balance between activity, durability, sustainability and cost of the catalysts. This always motivates me to look for a better catalytic system, and also resulted in this thesis. In the eSCALED project, our objective was to develop a noble metal free bioinspired device for H_2 production or CO_2 reduction using solar electrolysis. I was responsible for developing cathode materials for H_2 production. Therefore, my aim was to always look for materials applicable to device like condition. Considering that objective and my personal motivation, my overall doctoral journey is summarised in the following manner.

In **Paper I**, we aimed straight towards an immobilisation strategy for a bioinspired $\{Fe_2(\mu\text{-}S_2)(CO)_6\}$ based active sites, as this constitutes a key step for molecular based electrode materials for device applications. The anchoring method we settled for was π-π interactions, utilizing pyrene. We showed an improvement in loading capacity on the electrode as compared to previous reports, and an appreciable electronic communication between electrodes and catalysts. Finally, and importantly, the anchoring group appeared highly stable during catalysis. Still, the activity remained substandard under aqueous condition due to poor interaction with substrate (H^+ from buffer) and degradation of the catalyst/active site under catalytic conditions.

In **Paper II**, we aimed at encapsulating the [FeFe] site inside a water-soluble polymeric scaffold, to provide a basic outer coordination sphere along with an anchoring group in a single platform. The strategy met our expectations with regards to improved activity, but decreased the loading of active sites 4-5-fold, compared to the diiron complex deprived of polymer scaffold described in **Paper I**. Unfortunately, the polymeric scaffold could not protect the active site from degradation. In addition, we performed a life cycle assessment study to further highlight the importance of the metallopolymer strategy from a sustainability point of view.

In Paper III, we redesigned our metallopolymer by replacing the active site with what was expected to be a more robust diiron active site. In parallel, the new design could allow to tune and increase the fraction of active sites in the polymer chain. We found that the resulting metallopolymers showed an improved stability during electrolysis. However, the active site still remains the weak link in this assembly. Hence further improvement is still required.

On a more positive note, it is noteworthy to mention that we demonstrated through Papers **II** and **III**, that the metallopolymer approach is a highly promising for the preparation of synthetic systems and their employment in an energy conversion context. Clearly this could be extended to various energy conversion applications in future.

Finally, in **Paper IV**, we explored a biohybrid system by preparing and characterising semisynthetic hydrogenases. The detailed analysis provides some valuable insight towards the design of bioinspired catalysts for H^+/H_2 conversion. For example, this study demonstrated that how interaction with between active and secondary coordination sphere could impact on the rate of the catalysis. This study showed that tuning the secondary coordination sphere could turn an oxygen sensitive material into oxygen tolerant.

In closing, I think the insights that we learned throughout this thesis work motivates as followed

- Nature provides the ideal guidelines in order to continued search for an efficient catalyst.
- Heterogenous electrocatalysis is much more efficient and relevant for the practical application than that under homogenous condition.
- Immobilisation of catalyst using π-π interaction offers higher loading capacities and strong anchoring facilities.
- The metallopolymer approach is promising to design efficient catalyst for energy conversion in future. For that, the design of active and robust catalytic sites is crucial.
- Finally, evaluating environmental footprint of the product is essential from a sustainability perspective.

Résumé Francis

La décarbonisation mondiale nécessite une plus grande dépendance aux ressources énergétiques renouvelables, comme le suggère le récent rapport du (IPCC 2022).[18] Dans cette thèse, je me suis concentré sur l'hydrogène propre (H_2) comme stockage d'énergie renouvelable. L'énergie peut être stockée dans une liaison H–H à haute densité énergétique (enthalpie de combustion = –143 kJ mol^{-1}). L'utilisation de H_2 comme combustible dans les piles à combustible H_2/O_2 génère de l'électricité avec de la chaleur et de l'eau comme sous-produits. Cependant, la méthodologie actuelle de production de H_2 repose fortement sur «l'hydrogène gris» (c'est-à-dire utilisant des combustibles fossiles), qui émet des quantités substantielles de CO_2 (~ 10 kg d'équivalent CO_2 émis par kg de production de H_2). Par conséquent, la production à grande échelle de H_2 à faible teneur en carbone (c'est-à-dire d'hydrogène vert) promet de répondre à la demande énergétique mondiale tout en contribuant à l'objectif énergétique de zéro émission nette. Actuellement, la technologie « hydrogène vert » progresse à un stade prématuré et des développements supplémentaires dans ce domaine sont nécessaires.

Parmi les diverses sources d'énergie renouvelables disponibles, la technique de « l'hydrogène vert », c'est-à-dire la production de H_2 par « électrolyse solaire », est l'une des plus prometteuses. Ce dernier processus utilise l'énergie solaire pour alimenter la division de H_2O en O_2 et H_2. Néanmoins, l'implication de processus multi-électroniques et multi-protons ($4e^-$,$4H^+$) de la réaction mentionnée précédemment entraîne une cinétique de réaction lente et nécessite un catalyseur efficace (c'est-à-dire un matériau qui aide la réaction à s'exécuter plus rapidement) pour surmonter la cinétiquebarrière. Du point de vue économique, le catalyseur doit être bon marché, durable et extensible.

Les enzymes hydrogénases ont été découvertes pour la première fois dans les années 1930.[174] La synthèse de $\{Fe_2(\mu\text{-}S_2)(CO)_6\}$a été rapportée pour la première fois en 1928 sans aucune information sur les hydrogénases [FeFe]. La première structure cristalline des hydrogénases [FeFe] était rapporté dans les années 1990s[20] qui a déclenché le développement de la catalyse bioinspirée basée sur le noyau $\{Fe_2(\mu\text{-}S_2)(CO)_6\}$ en raison de ses similitudes structurelles avec le cofacteur $[2Fe]_H$.[19,91] domaine avec des efforts continus pour trouver l'équilibre optimal entre l'activité, la durabilité, la pérennité et le coût des catalyseurs. Cela me motive toujours à rechercher un meilleur système catalytique, et a également abouti à cette thèse. Dans le projet eSCALED, notre objectif était de développer un dispositif bioinspiré sans métaux nobles pour la production de H_2 ou la réduction de CO_2 par électrolyse solaire. J'étais responsable du développement de matériaux cathodiques pour la production de H_2. Par conséquent, mon objectif était de toujours rechercher des matériaux applicables à des conditions similaires à celles d'un appareil. Compte tenu de cet objectif et de ma motivation personnelle, mon parcours doctoral global se résume de la manière suivante.

Dans **l'article I**, nous avons visé directement une stratégie d'immobilisation pour des sites actifs à base de $\{Fe_2(\mu\text{-}S_2)(CO)_6\}$bioinspirés, car cela constitue une étape clé pour les matériaux d'électrodes à base moléculaire pour les applications de dispositifs. La méthode d'ancrage que nous avons choisie était les interactions π-π, en utilisant le pyrène. Pour cela, nous avons conçu et synthétisé un complexe ponté naphtoquinone $\{Fe_2(\mu\text{-}S_2)(CO)_6\}$comprenant deux molécules de pyrène par site actif. Le principe derrière le choix du pyrène était que le pyrène a une forte tendance à se lier avec des électrodes comme les nanotubes de carbone multiparois (MWNT) en utilisant des interactions π-π. Le complexe résultant a présenté une amélioration de la capacité

de charge sur l'électrode par rapport aux rapports précédents, et une communication électronique appréciable entre les électrodes et les catalyseurs. Enfin, et surtout, le groupe d'ancrage est apparu très stable pendant la catalyse. Pourtant, l'activité est restée inférieure à la norme dans des conditions aqueuses en raison d'une mauvaise interaction avec le substrat (H^+ du tampon) et de la dégradation du catalyseur/site actif dans des conditions catalytiques.

Dans **l'article II**, nous avons cherché à encapsuler le site [FeFe] à l'intérieur d'un échafaudage polymère soluble dans l'eau, afin de fournir une sphère de coordination externe de base ainsi qu'un groupe d'ancrage dans une plate-forme unique. Pour cela, nous avons conçu pour incorporer le même noyau ponté de naphtoquinone $\{Fe_2(\mu\text{-}S_2)(CO)_6\}$ mentionné dans **l'article I**, à l'intérieur d'un échafaudage polymère contenant une amine tertiaire (pour l'échange de protons entre le tampon et les sites actifs) et un pyrène (pour immobilisation sur électrode) à la sphère de coordination externe. Pour ce faire, nous avons conçu et synthétisé le monomère contenant du pyrène. Étant donné que le pyrène pourrait apporter une hydrophobicité importante à l'échafaudage polymère et avoir un impact sur l'activité, nous avons donc prévu de synthétiser une série de métallopolymères en faisant varier le pourcentage de pyrène dans la chaîne polymère.La stratégie a répondu à nos attentes en ce qui concerne l'amélioration de l'activité d'environ 70 fois plus d'activités avec moins d'exigences de surpotentiel que le catalyst mentionné dans le document II dans des conditions équivalentes. De plus, nous avons démontré qu'environ 7 à 8 % de pyrène par chaîne polymère est la composition optimisée afin d'équilibrer l'activité et la durabilité. Cependant, la stratégie métallopolymère a entraîné une chute de la charge des sites actifs de 4 à 5 fois, par rapport au complexe de difer dépourvu d'échafaudage polymère décrit dans **l'article I**. Malheureusement, l'échafaudage polymère ne pouvait pas protéger le site actif de la dégradation. En parallèle, nous avons réalisé une étude d'analyse du cycle de vie (LCA) pour souligner davantage l'importance de la stratégie métallopolymère d'un point de vue de la durabilité. Nous avons constaté que l'incorporation d'un site actif à l'intérieur d'un échafaudage polymère cause environ 80 % d'impact environnemental en moins pour une production électrochimique de H_2 équivalente à celle d'un site diiron dépourvu de métallopolymères. De plus, l'étude LCA pourrait identifier les MWNT en tant que composants les plus exigeants pendant le processus de production de H_2.

Dans **l'article III**, afin de surmonter la limitation (c'est-à-dire la dégradation) des métallopolymères mentionnée dans **l'article II**, nous avons repensé notre métallopolymère en remplaçant le site actif par ce qui devait être un site actif diiron plus robuste. Plus précisément, nous avons remplacé le groupe naphtoquinone pontant par un groupe fonctionnel amine tertiaire substitué par du styrène. Le groupe styrène tête de pont pourrait permettre d'ajuster et d'augmenter la fraction de sites actifs dans la chaîne polymère lors de la polymérisation. Le groupe amine pourrait offrir une fonctionnalité d'échange de protons placée à proximité immédiate du site diiron. Les métallopolymères résultants pourraient offrir une meilleure durabilité au prix d'une activité deux fois moindre par rapport aux métallopolymères mentionnés dans le **document II** dans des conditions équivalentes. Pour être précis après 3 heures d'électrolyse, le courant ou l'activité des métallopolymères à la surface de l'électrode reste remarquablement stable pendant 20 heures. Cependant, nous avons constaté que le site actif reste toujours le maillon faible de ce montage. Par conséquent, d'autres améliorations sont encore nécessaires pour accroître l'activité au-delà de l'échelle quotidienne.

Sur une note plus positive, il convient de mentionner que nous avons démontré à travers les **articles II et III**, que l'approche métallopolymère est très prometteuse pour la préparation de systèmes synthétiques et leur emploi dans un contexte de conversion d'énergie Il est clair que cela pourrait être étendu à différentes applications de conversion énergétique dans le futur.

Enfin, dans **l'article IV**, nous avons exploré un système biohybride en préparant et en caractérisant des hydrogénases semi-synthétiques en ajustant les propriétés électroniques et

structurelles des sites actifs des hydrogénases [FeFe]. Pour être précis, nous remplaçons l'un des ligands CN présents dans les sites actifs natifs et incorporés à l'intérieur de deux échafaudages d'hydrogénases [FeFe] structurellement distincts. Les enzymes hydrogénases hybrides résultantes se sont révélées moins sensibles aux inhibiteurs tels que O_2, CO. Cependant, il a également été constaté que les enzymes résultantes étaient moins actives pour l'évolution de H2. Fait intéressant, l'activité et la sensibilité trouvées varient entre deux échafaudages protéiques implicites. Nous avons essayé d'étudier les détails structurels des cofacteurs à l'intérieur des enzymes pour comprendre la différence de comportement. Nous avons constaté que l'interaction du cofacteur modifié avec les acides aminés environnants jouait un rôle clé dans la sensibilité et l'activité. Ainsi, nous avons pu démontrer que l'interaction entre les sphères de coordination active et secondaire pouvait avoir un impact sur l'activité, la sensibilité, l'état redox des mêmes sites actifs. L'analyse détaillée fournit des informations précieuses sur la conception de catalyseurs bioinspirés pour la conversion H^+/H_2. Par exemple, cette étude a montré que l'ajustement de la sphère de coordination secondaire pouvait transformer un matériel sensible à l'oxygène en un matériel tolérant à l'oxygène.

Pour conclure, je crois que les idées que nous avons apprises au cours de cette thèse motivent ce qui suit :

(i) Continuer à s'inspirer de la Nature dans la recherche continue d'un catalyseur idéal.
(ii) L'immobilisation du catalyseur à l'aide de l'interaction π-π offre des capacités de chargement plus élevées et des installations d'ancrage solides.
(iii) L'approche métallopolymère est prometteuse pour concevoir un catalyseur efficace pour la conversion d'énergie à l'avenir. Pour cela, la conception de sites catalytiques actifs et robustes est cruciale.
(iv) Enfin, l'évaluation de l'empreinte environnementale du produit est essentielle du point de vue de la durabilité.

Popular Science Summary

Global decarbonization requires more reliance on renewable energy resources as suggested by the recent IPCC report (2022). In this thesis, I focused on clean hydrogen (H_2) as a renewable energy storage. Energy can be stored in high energy dense H–H bond. Then the H_2 can be used as a fuel in H_2/O_2 fuel cells (cell that produces electricity from chemical reaction) to generates electricity with heat and water as sub-products. However, the current H_2 production methodology highly relies on "gray hydrogen" (*i.e.* using fossil fuels), which emits substantial amounts of carbon dioxide (a gas that found in air, can trap heat and increase the temperature in earth atmosphere) . Therefore, the production of low carbon or carbon free H_2 (*i.e.* green hydrogen) at scale holds the promise to meet the global energy demand while contributing to the net zero emission energy goal. Currently, "green hydrogen" technology is progressing at a pre-mature stage and further developments in this field are required.

Among various available renewable energy sources, the "green hydrogen" technology, *i.e.* H_2 production using "solar electrolysis", is one of the most promising technologies. The latter process uses solar energy to power the splitting of water (H_2O) into O_2 and H_2. Nevertheless, the involvement of multi-electronic and multi-proton ($4e^-$,$4H^+$) processes of the previously mentioned reaction results in slow reaction kinetics and demands an efficient catalyst (*i.e.* a material that help the reaction to run faster) to overcome the kinetic barrier. From an economic perspective, the catalyst should be of low-cost, durable, and scalable.

Hydrogenase enzymes (enzyme is the catalyst made by nature) already architected by nature do the H_2 production from water at excellent rates (~10,000 molecules of H_2 per molecule of enzyme per second) with negligible overpotential (additional thermodynamic push) requirements using inexpensive 3d transition metals at neutral pH. Thus, hydrogenase enzymes meet most of the previously mentioned criteria to be an ideal candidate for an H_2 production catalyst for "green hydrogen" technology. Yet, their durability under atmospheric oxygen and scalability remain barriers concerning industrial demands. However, intensive efforts are going on to use this impressive biomolecule for large-scale applications. In parallel, due to their excellent activities, hydrogenase enzymes remain a blueprint for developing synthetic catalysts for equivalent applications. Thus, understanding the science running in hydrogenase enzymes and translating the insights on developing bioinspired catalysts, followed by integrating the resulting catalyst in devices, are the sensible steps to put "green hydrogen" technology forward.

My thesis focused to cover the aforementioned steps within the scope of the project in the following ways.

Firstly, since immobilization (or anchoring) of the catalyst on electrode (a conductive material that exchanges electron) is compulsory for developing devices. Therefore, we planned to design a bioinspired (inspired from hydrogenase enzyme) catalyst to graft it on the electrode surface H_2 production in water. The anchoring strategy was found very promising as the durability of the catalyst on electrode was impressive throughout the catalysis (H_2 production). Unfortunately, the catalyst was limited by substandard activity and degradation (turned into something that does not produce H_2 anymore) of the catalyst.

In the second step, we planned to act against the poor activity and durability by wrapping the active site inside a designed polymer (a large molecule made of one or more than one repetitive molecules). The strategy was encouraging as the resulting polymers could elevate the activity substantially than the catalyst discussed earlier. In parallel, an environmental impact for H_2 production (how much CO_2 emitted per kg of H_2 production) by the polymers was studied.

In the third step, we focused on understanding the science pursued in [FeFe] hydrogenase enzymes. Hydrogenase chemistry has been extensively studied for more than 90 years. Yet, the scope of this chemistry is huge and only a fraction of it has been revealed. We aimed to understand the chemical (by changing particular chemical composition) and structural (by

changing the structure) influences on the activity and sensitivity of [FeFe] hydrogenases. This study is promising and yields some key insights for developing semi-artificial hydrogenase enzyme for energy-relevant application in the future.

The overall thesis showcased that the how an efficient catalyst can be developed, inspiring from biology and used in device for H_2 production in water.

Populärvetenskaplig Sammanfatning

Den här avhandlingen är delvis en påminnelse om hur brådskande våra miljöproblem är. Miljöförändringar förväntas medföra stark turbulens för mänskligheten. Bland de stora problemen kommer energikrisen att vara det första problemet, då det redan blivit akut i stora delar av världen. Global uppvärmning, luftföroreningar, havsförsurning och höjning av havsnivån i oroväckande takt kommer också att vara kritiska att ta itu med.

I det sammanhanget skulle vätgas (H_2) kunna vara ett potentiellt alternativ till fossila bränslen, och möjliggöra ett energisystem med nollutsläpp. H_2 har kapaciteten att lagra stora mängder energi på sikt, och användningen av H_2 i en bränslecell för att generera el resulterar bara i värme och vatten som bprodukter. Att producera H_2 med en kolfri process (dvs. med hjälp av förnybar energi) kan därför vara vår räddning ur ett miljö- och hållbarhetsperspektiv. Sådan vätgas kallas också för "Grönt vätgas".

Men H_2-produktionsmetodologin förlitar sig för närvarande på "Grå vätgas". Det vill säga vätgas producerad med hjälp av icke-förnybar energi, en process som släpper ut en betydande mängd CO_2. Tekniken för "grön vätgas" är under utveckling i detta skede.

Bland olika förnybara källor inom "grön vätgas"-teknik är H_2-produktion med solelektrolys en av de lovande teknikerna. Den senare processen använder elektricitet för att dela H_2O i O_2 och H_2 (kallad vattenelektrolys). Denna reaktions multielektroniska karaktär resulterar i långsam kinetik och kräver katalysatorer för att genomföras. Katalysatorn ska vara billig, aktiv, hållbar och skalbar.

Hydrogenasenzym som redan skapats av naturen, utför vätgasproduktionen från vatten med utmärkt hastighet utan energiförluster, och klarar detta med hjälp av billiga och lättillgängliga metaller (järn och nickel). Således uppfyller hydrogenasenzymer alla kriterier för att vara en idealisk katalysatorkandidat. Även om robusthet och skalbarhet kan vara hinder för större industriella applikationer, men intensiva ansträngningar pågår för att använda det i storskalig tillämpning. Dessutom skulle hydrogenasenzymer kunna utgöra en guide för utveckling av syntetiska katalysatorer för motsvarande tillämpning. I ljuset av detta har jag valt att fokusera på tre specifika typer av studier, som jag anser vara viktiga och lovande för grön vätgasteknik:

(i) Förstå hur hydrogenasenzymer fungerar på molekylnivå.

(ii) Översätt insikterna från (i), för att utveckla bioinspirerade katalysatorer och förbättra dessa för att användning i apparater för vätgasproduktion från vatten.

(iii) Utvärdera slutligen miljöavtrycket för potentiellt relevanta katalysatorer.

Mitt doktorsarbete syftade till att bidra till ovannämnda tre punkter enligt följande

I **papper I**, **II** och **III** koncentrerade vi oss på bioinspirerade katalysatorer, förbättrade dem för att tillverka elektrodmaterial som kan användas i apparater och bedömde deras miljöavtryck. Kort sagt fokuserade vi på punkt (ii) och (iii), som beskrivits tidigare.

I **artikel IV** fokuserade vi på att identifiera en del av de faktorer som gör hydrogenasenzymerna så effektiva, dvs punkt (i). Även om hydrogenasenzymerna har studerats i mer än 90 år, så är komplexiteten av deras kemi enorm och vi är fortfarande inte helt klara över hur de fungerar. Vi kunde i detta arbete visa på hur vi genom att använda syntetisk kemi kunde framställa mer robusta former av enzymerna.

Ett stort tema i avhandlingen är att metallpolymerer är ett lovande tillvägagångssätt för att utveckla bioinspirerade katalysatorer, eftersom de kan främja aktiviteten och robustheten för katalysatorer. Arbetet trycker även på att en immobiliseringsstrategi alltid bör vara en del av den molekylära designen för att möjliggöra användningen av katalysatorn under apparatliknande betingelser.

Slutligen bör studier på hydrogenasenzymer utföras för att modifiera denna utmärkta biomolekyl enligt våra krav och därigenom vidare förbättra denna biokatalysator.

Acknowledgements

I think results of doctoral study is not only the thesis but also yourself. In order to make it possible, there are so many persons that helps throughout the thesis.

I would like to start with my supervisors **Prof. Gustav Berggren** (UU), **Dr. Vincent Artero** (UGA). Without them, this study would not be possible. I have no words to acknowledge them. They were always very patient, kind to me throughout the journey. They have always motivated me to think everything in more scientific way.

The next should be **Dr. Reuillard Bertrand** from UGA. You have been one of the most humble and inspiring researchers that I have come across. You are a true motivation and I always wanted to be a researcher and person like you in future.

I would like to thank **Jose Jorge Espí Gallart** from eurecat for being humble to me throughout the LCA study. Despite from a different background, you always motivated me to involved in this study.

I would like to thank **Prof. Laurent Billon** from UPPA for his kind support throughout the study. I was very motivated by his time management and learning polymer science from him

I would like to thank my co-supervisor **Prof. Sascha Ott** for very kind and supportive throughout studies.

I would like to thank **Prof. Leif Hammarström** for very kind, supportive and energetic throughout this project.

I would like to thank Laia **Francesch** from UPPA, for being heart of this project. You were humble, kind and treated us like your child. Countless things to learn from you.

I would like to thank **Prof. Antoine Bousquet** for being very kind and supportive during the project. I enjoyed playing football with you during workshop in Anglet.

I would like to thank **Dominique Foix, Pierre Marcasuzaa** for their kind gesture and support.

I would like to thank **Anders Thapper** for always being kind, helpful and guide me in various way.

I would like to thank **Prof. Peter Lindblad, Pia Lindberg, Starla Glover** for their support.

AJB, thanks for everything from study to discussion. So much happy time in office after work. You will be missed.

Nidhi, thanks for always being kind. I always find you with smile and energetic face. I would like to that **Andjela, Andrea, Martin**, **Minli, Maria, Nora** for being very humble and supportive to me. **Monika**, **Amol**, **Samir**: Thanks for being kind, supportive and all funny discussion during lunch time. You guys are special.

Robin correction, **Dr. Durr**. You are the one college from whom I learned a lot from starting day of this project. Thanks for extremely supportive and kind to me.

Sagar (Kesto da), thanks for being supportive and helping me with you precious suggestions. Our lunch discussion will always be in my mind.

Marco, thanks for helping me to learn biology. You are very helpful and kind to me.

Princess, you are amazing the way you pursue your study. I have learned a lot from you. Thanks a lot for being so humble and funny.

Kaija, thanks a lot for your kind-hearted nature. I always saw you working hard with big smile. You are a true motivation.

I would like to thank **Holly** for always being nice to me. I learned a lot of synthetic chemistry from you.

Mira, Larissa, Olha, Claudia, Luca thanks a lot for everything.

I would like to thank the other BBC group members for being very helpful and kind to me and all their supports throughout my study: **Fikret Memedov**, **Ping Huang, Henrik Land, Moritz,**

Sergii Shylin, Brigitta Nemeth, Ann Magnuson, Michael Cheah, Fatemeh Khosravitabar, Petko Chernev, Marcus Lundberg, Shipra Prakash and **Long Ho Pham.**

From my CEA, Grenoble group: **Angel**, **Mariam**, **Nabil**, **Jonathan**, **Yao**, **Matt**, **Kun, Manos, Duc, Louis** you guys live in my heart. Thanks a lot for countless memories.

I would like to thank **Dr. Murielle Chavarot Kerlidou** for her support and kind gestures.

I would like to thank **Dr. Matthieu Koepf** for his help and kind heart. Your dedication to work is a motivation for me.

I would like to thank **Adina Morozan** for being extremely helpful.

I would like to thank **Jennifer Fize** for being so humble and helpful.

Finally, I would like to thank **eSCALED project** under European Union's Horizon 2020 research and innovation programme under grant agreement No. 765376 for proving me this opportunity to accomplish this study.

Last but not the least, I would like to thank **my parents and family** for their dedication and support throughout my life.

References

1 H. Ritchie, M. Roser and P. Rosado, 2022.
2 Z. Liu, Z. Deng, S. J. Davis, C. Giron and P. Ciais, *Nat Rev Earth Environ*, 2022, **3**, 217–219.
3 H. Ritchie, M. Roser and P. Rosado, *Our World in Data*.
4 IPCC, *Working Group III contribution to the Sixth Assessment Report of the*, IPCC, 2022.
5 S. van Renssen, *Nat. Clim. Chang.*, 2020, **10**, 799–801.
6 IEA, *The Future of Hydrogen*, IEA, 2019.
7 Bloomberg L.P., *Hydrogen Economy Outlook: Key Messages*, Bloomberg L.P., 2020.
8 *Hydrogen Europe*, 2022.
9 *IEA (2022), Hydrogen Supply, IEA, Paris*, .
10 D. Castelvecchi, *Nature*, 2022, **611**, 440–443.
11 *Hydrogen*, International Renewable Energy Agency, 2022.
12 G. Glenk and S. Reichelstein, *Nat. Energy*, 2019, **4**, 216–222.
13 Y. Zhou, R. Li, Z. Lv, J. Liu, H. Zhou and C. Xu, *Chinese Journal of Chemical Engineering*, 2022, **43**, 2–13.
14 M. Carmo, D. L. Fritz, J. Mergel and D. Stolten, *Int. J. Hydrog. Energy*, 2013, **38**, 4901–4934.
15 B. Zhang, L. Fan, R. B. Ambre, T. Liu, Q. Meng, B. J. J. Timmer and L. Sun, *Joule*, 2020, **4**, 1408–1444.
16 M. David, C. Ocampo-Martínez and R. Sánchez-Peña, *J. Energy Storage*, 2019, **23**, 392–403.
17 W. Lubitz, H. Ogata, O. Rüdiger and E. Reijerse, *Chem. Rev.*, 2014, **114**, 4081–4148.
18 M. Stephenson and L. H. Stickland, *Biochem J*, 1931, **25**, 205–214.
19 J. T. Kleinhaus, F. Wittkamp, S. Yadav, D. Siegmund and U.-P. Apfel, *Chem. Soc. Rev.*, 2021, **50**, 1668–1784.
20 J. W. Peters, W. N. Lanzilotta, B. J. Lemon and L. C. Seefeldt, .
21 D. W. Mulder, E. S. Boyd, R. Sarma, R. K. Lange, J. A. Endrizzi, J. B. Broderick and J. W. Peters, *Nature*, 2010, **465**, 248–251.
22 Y. Nicolet, C. Piras, P. Legrand, C. E. Hatchikian and J. C. Fontecilla-Camps, *Structure*, 1999, **7**, 13–23.
23 D. W. Mulder, E. M. Shepard, J. E. Meuser, N. Joshi, P. W. King, M. C. Posewitz, J. B. Broderick and J. W. Peters, *Structure*, 2011, 19, 1038–1052.
24 H. Land, M. Senger, G. Berggren and S. T. Stripp, *ACS Catal.*, 2020, **10**, 7069–7086.
25 Y. Nicolet, C. Piras, P. Legrand, C. E. Hatchikian and J. C. Fontecilla-camps, 13–23.
26 J. A. Birrell, V. Pelmenschikov, N. Mishra, H. Wang, Y. Yoda, K. Tamasaku, T. B. Rauchfuss, S. P. Cramer, W. Lubitz and S. Debeer, *J. Am. Chem. Soc.*, 2020, **142**, 222–232.
27 D. Goldfarb, *Phys. Chem. Chem. Phys.*, 2009, **11**, 6553–6554.
28 G. Berggren, A. Adamska, C. Lambertz, T. R. Simmons, J. Esselborn, M. Atta, S. Gambarelli, J.-M. Mouesca, E. Reijerse, W. Lubitz, T. Happe, V. Artero and M. Fontecave, *Nature*, 2013, **499**, 66–69.

29 A. S. Pandey, T. V. Harris, L. J. Giles, J. W. Peters and R. K. Szilagyi, *J. Am. Chem. Soc.*, 2008, **130**, 4533–4540.
30 A. J. Cornish, H. Yang, J. W. Peters and E. L. Hegg, 2011, **286**, 38341–38347.
31 B. Ginovska-pangovska, M. Ho, J. C. Linehan, Y. Cheng, M. Dupuis, S. Raugei and W. J. Shaw, *BBA - Bioenergetics*, 2014, **1837**, 131–138.
32 P. Knörzer, A. Silakov, C. E. Foster, F. A. Armstrong, W. Lubitz and T. Happe, *J. Biol. Chem.*, 2012, **287**, 1489–1499.
33 M. C. Posewitz, P. W. King, S. L. Smolinski, L. Zhang, M. Seibert and M. L. Ghirardi, *J. Biol. Chem.*, 2004, **279**, 25711–25720.
34 P. W. King, M. C. Posewitz, M. L. Ghirardi and M. Seibert, *J. Bacteriol.*, 2006, **188**, 2163–2172.
35 S. E. McGlynn, E. M. Shepard, M. A. Winslow, A. V. Naumov, K. S. Duschene, M. C. Posewitz, W. E. Broderick, J. B. Broderick and J. W. Peters, *FEBS Letters*, 2008, **582**, 2183–2187.
36 I. Czech, A. Silakov, W. Lubitz and T. Happe, *FEBS Letters*, 2010, **584**, 638–642.
37 J. Meyer, *Cell. Mol. Life Sci.*, 2007, **64**, 1063–1084.
38 J. Esselborn, C. Lambertz, A. Adamska-Venkatesh, T. Simmons, G. Berggren, J. Noth, J. Siebel, A. Hemschemeier, V. Artero, E. Reijerse, M. Fontecave, W. Lubitz and T. Happe, *Nat. Chem. Biol.*, 2013, **9**, 607–609.
39 M. W. Ratzloff, J. H. Artz, D. W. Mulder, R. T. Collins, T. E. Furtak and P. W. King, *J. Am. Chem. Soc.*, 2018, **140**, 7623–7628.
40 C. Sommer, A. Adamska-Venkatesh, K. Pawlak, J. A. Birrell, O. Rüdiger, E. J. Reijerse and W. Lubitz, *J. Am. Chem. Soc.*, 2017, **139**, 1440–1443.
41 M. Haumann and S. T. Stripp, *Acc. Chem. Res.*, 2018, **51**, 1755–1763.
42 M. A. Martini, O. Rüdiger, N. Breuer, B. Nöring, S. DeBeer, P. Rodríguez-Maciá and J. A. Birrell, *J. Am. Chem. Soc.*, 2021, **143**, 18159–18171.
43 A. Adamska, A. Silakov, C. Lambertz, O. Rüdiger, T. Happe, E. Reijerse and W. Lubitz, *Angew. Chem. Int. Ed.*, 2012, **51**, 11458–11462.
44 M. Winkler, M. Senger, J. Duan, J. Esselborn, F. Wittkamp, E. Hofmann, U.-P. Apfel, S. T. Stripp and T. Happe, *Nat. Commun.*, 2017, **8**, 16115.
45 M. Senger, S. Mebs, J. Duan, O. Shulenina, K. Laun, L. Kertess, F. Wittkamp, U.-P. Apfel, T. Happe, M. Winkler, M. Haumann and S. T. Stripp, *Phys. Chem. Chem. Phys.*, 2018, **20**, 3128–3140.
46 V. Pelmenschikov, J. A. Birrell, C. C. Pham, N. Mishra, H. Wang, C. Sommer, E. Reijerse, C. P. Richers, K. Tamasaku, Y. Yoda, T. B. Rauchfuss, W. Lubitz and S. P. Cramer, *J. Am. Chem. Soc.*, 2017, **139**, 16894–16902.
47 D. W. Mulder, M. W. Ratzloff, M. Bruschi, C. Greco, E. Koonce, J. W. Peters and P. W. King, *J. Am. Chem. Soc.*, 2014, **136**, 15394–15402.
48 Y. Nicolet, A. L. de Lacey, X. Vernède, V. M. Fernandez, E. C. Hatchikian and J. C. Fontecilla-Camps, *J. Am. Chem. Soc.*, 2001, **123**, 1596–1601.
49 J. A. Birrell, V. Pelmenschikov, N. Mishra, H. Wang, Y. Yoda, K. Tamasaku, T. B. Rauchfuss, S. P. Cramer, W. Lubitz and S. DeBeer, *J. Am. Chem. Soc.*, 2020, **142**, 222–232.
50 A. Adamska-Venkatesh, D. Krawietz, J. Siebel, K. Weber, T. Happe, E. Reijerse and W. Lubitz, *J. Am. Chem. Soc.*, 2014, **136**, 11339–11346.
51 H. Land, A. Sekretareva, P. Huang, H. J. Redman, B. Németh, N. Polidori, L. S. Mészáros, M. Senger, S. T. Stripp and G. Berggren, *Chem. Sci.*, 2020, **11**, 12789–12801.
52 N. Chongdar, J. A. Birrell, K. Pawlak, C. Sommer, E. J. Reijerse, O. Rüdiger, W. Lubitz and H. Ogata, *J. Am. Chem. Soc.*, 2018, **140**, 1057–1068.
53 P. Rodríguez-Maciá, E. J. Reijerse, M. Van Gastel, S. Debeer, W. Lubitz, O. Rüdiger and J. A. Birrell, *J. Am. Chem. Soc.*, 2018, **140**, 9346–9350.

54 S. Morra, M. Arizzi, F. Valetti and G. Gilardi, *Biochemistry*, 2016, **55**, 5897–5900.
55 P. S. Corrigan, J. L. Tirsch and A. Silakov, *J. Am. Chem. Soc.*, 2020, **142**, 12409–12419.
56 M. Winkler, J. Duan, A. Rutz, C. Felbek, L. Scholtysek, O. Lampret, J. Jaenecke, U. Apfel, G. Gilardi, F. Valetti, V. Fourmond, E. Hofmann, C. Léger and T. Happe, *Nat. Commun.*, 1–10.
57 A. Kubas, C. Orain, D. De Sancho, L. Saujet, M. Sensi, C. Gauquelin, I. Meynial-Salles, P. Soucaille, H. Bottin, C. Baffert, V. Fourmond, R. B. Best, J. Blumberger and C. Léger, *Nat. Chem.*, 2017, **9**, 88–95.
58 K. D. Swanson, M. W. Ratzloff, D. W. Mulder, J. H. Artz, S. Ghose, A. Hoffman, S. White, O. A. Zadvornyy, J. B. Broderick, B. Bothner, P. W. King and J. W. Peters, *J. Am. Chem. Soc.*, 2015, **137**, 1809–1816.
59 M. Winkler, J. Duan, A. Rutz, C. Felbek, L. Scholtysek, O. Lampret, J. Jaenecke, U.-P. Apfel, G. Gilardi, F. Valetti, V. Fourmond, E. Hofmann, C. Léger and T. Happe, *Nat. Commun.*, 2021, **12**, 756.
60 S. Morra, M. Arizzi, F. Valetti and G. Gilardi, *Biochemistry*, 2016, **55**, 5897–5900.
61 C. Léger and P. Bertrand, *Chem. Rev.*, 2008, **108**, 2379–2438.
62 N. Kornienko, K. H. Ly, W. E. Robinson, N. Heidary, J. Z. Zhang and E. Reisner, *Acc. Chem. Res.*, 2019, **52**, 1439–1448.
63 E. Lojou, *Electrochimica Acta*, 2011, **56**, 10385–10397.
64 F. A. Armstrong, N. A. Belsey, J. A. Cracknell, G. Goldet, A. Parkin, E. Reisner, K. A. Vincent and A. F. Wait, *Chem. Soc. Rev.*, 2008, **38**, 36–51.
65 M. Sensi, M. del Barrio, C. Baffert, V. Fourmond and C. Léger, *Curr. Opin. Electrochem.*, 2017, **5**, 135–145.
66 N. Plumeré, O. Rüdiger, A. A. Oughli, R. Williams, J. Vivekananthan, S. Pöller, W. Schuhmann and W. Lubitz, *Nature Chem*, 2014, **6**, 822–827.
67 A. A. Oughli, S. Hardt, O. Rüdiger, J. A. Birrell and N. Plumeré, *Chem. Commun.*, 2020, **56**, 9958–9961.
68 J. Szczesny, N. Marković, F. Conzuelo, S. Zacarias, I. A. C. Pereira, W. Lubitz, N. Plumeré, W. Schuhmann and A. Ruff, *Nat Commun*, 2018, **9**, 4715.
69 A. Ruff, F. Conzuelo and W. Schuhmann, *Nat Catal*, 2020, **3**, 214–224.
70 J. A. Laureanti, M. O'Hagan and W. J. Shaw, *Sustain. Energy Fuels*, 2019, **3**, 3260–3278.
71 C. Esmieu, P. Raleiras and G. Berggren, *Sustain. Energy Fuels*, 2018, **2**, 724–750.
72 A. C. Ghosh, C. Duboc and M. Gennari, *Coord. Chem. Rev.*, 2021, **428**, 213606.
73 B. Kandemir, S. Chakraborty, Y. Guo and K. L. Bren, *Inorg. Chem.*, 2016, **55**, 467–477.
74 D. Schilter, J. M. Camara, M. T. Huynh, S. Hammes-Schiffer and T. B. Rauchfuss, *Chem. Rev.*, 2016, **116**, 8693–8749.
75 L. Sun, C. Duboc and K. Shen, *ACS Catal.*, 2022, 9159–9170.
76 J. F. Siebel, A. Adamska-Venkatesh, K. Weber, S. Rumpel, E. Reijerse and W. Lubitz, *Biochemistry*, 2015, **54**, 1474–1483.
77 M. Lorenzi, J. Gellett, A. Zamader, M. Senger, Z. Duan, P. Rodríguez-Maciá and G. Berggren, *Chem. Sci.*, 2022, **13**, 11058–11064.
78 L. Kertess, F. Wittkamp, C. Sommer, J. Esselborn, O. Rüdiger, E. J. Reijerse, E. Hofmann, W. Lubitz, M. Winkler, T. Happe and U.-P. Apfel, *Dalton Trans.*, 2017, **46**, 16947–16958.
79 C. Sommer, C. P. Richers, W. Lubitz, T. B. Rauchfuss and E. J. Reijerse, *Angew. Chem. Int. Ed.*, 2018, **57**, 5429–5432.
80 C. Esmieu, P. Raleiras and G. Berggren, *Sustain. Energy and Fuels*, 2018, **2**, 724–750.

81 J. A. Laureanti, M. O'Hagan and W. J. Shaw, *Sustain. Energy and Fuels*, 2019, **3**, 3260–3278.
82 D. W. Wakerley and E. Reisner, *Energy and Environ. Sci.*, 2015, **8**, 2283–2295.
83 D. Schilter, J. M. Camara, M. T. Huynh, S. Hammes-Schiffer and T. B. Rauchfuss, *Chem. Rev.*, 2016, **116**, 8693–8749.
84 B. Kandemir, S. Chakraborty, Y. Guo and K. L. Bren, *Inorg. Chem.*, 2016, **55**, 467–477.
85 A. C. Ghosh, C. Duboc and M. Gennari, *Coord. Chem. Rev.*, 2021, **428**, 213606.
86 Y. Li and T. B. Rauchfuss, *Chem. Rev.*, 2016, **116**, 7043–7077.
87 N. Coutard, N. Kaeffer and V. Artero, *Chem. Commun.*, 2016, **52**, 13728–13748.
88 V. Artero, M. Chavarot-Kerlidou and M. Fontecave, *Angew. Chem. Int. Ed.*, 2011, **50**, 7238–7266.
89 A. Dutta, A. M. Appel and W. J. Shaw, *Nat Rev Chem*, 2018, **2**, 244–252.
90 V. S. Thoi, Y. Sun, J. R. Long and C. J. Chang, *Chem. Soc. Rev.*, 2013, **42**, 2388–2400.
91 G. A. N. Felton, C. A. Mebi, B. J. Petro, A. K. Vannucci, D. H. Evans, R. S. Glass and D. L. Lichtenberger, *J. Organomet. Chem.*, 2009, **694**, 2681–2699.
92 M. Karayilan, W. P. Brezinski, K. E. Clary, D. L. Lichtenberger, R. S. Glass and J. Pyun, *Angew. Chem. Int. Ed.*, 2019, **58**, 7537–7550.
93 A. Roy, C. Madden and G. Ghirlanda, *Chem. Commun.*, 2012, **48**, 9816.
94 A. Roy, M. D. Vaughn, J. Tomlin, G. J. Booher, G. Kodis, C. R. Simmons, J. P. Allen and G. Ghirlanda, *Chem. Eur. J.*, 2020, **26**, 6240–6246.
95 S. Roy, T.-A. D. Nguyen, L. Gan and A. K. Jones, *Dalton Trans.*, 2015, **44**, 14865–14876.
96 F. Wang, W.-J. Liang, J.-X. Jian, C.-B. Li, B. Chen, C.-H. Tung and L.-Z. Wu, *Angew. Chem.*, 2013, **125**, 8292–8296.
97 M. Wen, X.-B. Li, J.-X. Jian, X.-Z. Wang, H.-L. Wu, B. Chen, C.-H. Tung and L.-Z. Wu, *Sci Rep*, 2016, **6**, 29851.
98 X. Zhu, W. Zhong and X. Liu, *Int. J. Hydrog. Energy*, 2016, **41**, 14068–14078.
99 W. P. Brezinski, M. Karayilan, K. E. Clary, K. C. McCleary-Petersen, L. Fu, K. Matyjaszewski, D. H. Evans, D. L. Lichtenberger, R. S. Glass and J. Pyun, *ACS Macro Letters*, 2018, **7**, 1383–1387.
100 S. K. Ibrahim, X. Liu, C. Tard and C. J. Pickett, *Chem. Commun.*, 2007, 1535.
101 K. N. Green, J. L. Hess, C. M. Thomas and M. Y. Darensbourg, *Dalton Trans.*, 2009, 4344–4350.
102 L. Wang, Z. Xiao, X. Ru and X. Liu, *RSC Adv.*, 2011, **1**, 1211.
103 X. Ru, X. Zeng, Z. Li, D. J. Evans, C. Zhan, Y. Tang, L. Wang and X. Liu, *J. Pol. Sci., Part A: Poly. Chem.*, 2010, **48**, 2410–2417.
104 C. Zhan, X. Wang, Z. Wei, D. J. Evans, X. Ru, X. Zeng and X. Liu, *Dalton Trans.*, 2010, **39**, 11255–11262.
105 W. P. Brezinski, M. Karayilan, K. E. Clary, N. G. Pavlopoulos, S. Li, L. Fu, K. Matyjaszewski, D. H. Evans, R. S. Glass, D. L. Lichtenberger and J. Pyun, *Angew. Chem. Int. Ed.*, 2018, **57**, 11898–11902.
106 O. In-noi, K. J. Haller, G. B. Hall, W. P. Brezinski, J. M. Marx, T. Sakamoto, D. H. Evans, R. S. Glass and D. L. Lichtenberger, *Organometallics*, 2014, **33**, 5009–5019.
107 F. Zhang, C. P. Richers, T. J. Woods and T. B. Rauchfuss, *Angew. Chem., Int. Ed.*, 2021, **60**, 20744–20747.
108 S. J. Borg, T. Behrsing, S. P. Best, M. Razavet, X. Liu and C. J. Pickett, *J. Am. Chem. Soc.*, 2004, **126**, 16988–16999.
109 B. E. Barton and T. B. Rauchfuss, *Inorg. Chem.*, 2008, **47**, 2261–2263.
110 V. C.-C. Wang, C. Esmieu, H. J. Redman, G. Berggren and L. Hammarström, *Dalton Trans.*, 2020, **49**, 858–865.

111 J. Wang, S. Dou and X. Wang, 2021, 1–14.
112 R. M. Bullock, A. K. Das and A. M. Appel, *Chem. Euro J.*, 2017, **23**, 7626–7641.
113 K. E. Dalle, J. Warnan, J. J. Leung, B. Reuillard, I. S. Karmel and E. Reisner, *Chem. Rev.*, 2019, **119**, 2752–2875.
114 M. E. Ahmed, S. Dey, B. Mondal and A. Dey, *Chem. Commun.*, 2017, **53**, 8188–8191.
115 S. Dey, A. Rana, S. G. Dey and A. Dey, *ACS Catal.*, 2013, **3**, 429–436.
116 A. Ghedjatti, N. Coutard, L. Calvillo, G. Granozzi, B. Reuillard, V. Artero, L. Guetaz, S. Lyonnard, H. Okuno and P. Chenevier, *Chem. Sci.*, 2021, **12**, 15916–15927.
117 J. Schild, B. Reuillard, A. Morozan, P. Chenevier, E. Gravel, E. Doris and V. Artero, *J. Am. Chem. Soc.*, 2021, **143**, 18150–18158.
118 V. Vijaikanth, J.-F. Capon, F. Gloaguen, P. Schollhammer and J. Talarmin, *Electrochem. commun.*, 2005, **7**, 427–430.
119 C. M. Thomas, O. Rüdiger, T. Liu, C. E. Carson, M. B. Hall and M. Y. Darensbourg, *Organometallics*, 2007, **26**, 3976–3984.
120 A. Le Goff, V. Artero, R. Metayé, F. Moggia, B. Jousselme, M. Razavet, P. D. Tran, S. Palacin and M. Fontecave, *Int. J. Hydrog. Energy*, 2010, **35**, 10790–10796.
121 E. Xu, Z. Xiao, H. Liu, L. Long, L. Li and X. Liu, *RSC Adv.*, 2012, **2**, 10171.
122 X. Ru, X. Zeng, Z. Li, D. J. Evans, C. Zhan, Y. Tang, L. Wang and X. Liu, *J. Polym. Sci. A Polym. Chem.*, 2010, **48**, 2410–2417.
123 M. E. Ahmed, S. Dey, M. Y. Darensbourg and A. Dey, *J. Am. Chem. Soc.*, 2018, **140**, 12457–12468.
124 M. E. Ahmed, A. Nayek, A. Križan, N. Coutard, A. Morozan, S. Ghosh Dey, R. Lomoth, L. Hammarström, V. Artero and A. Dey, *J. Am. Chem. Soc.*, 2022, **144**, 3614–3625.
125 P.-H. Zhao, J.-R. Li, Z.-Y. Ma, H.-F. Han, Y.-P. Qu and B.-P. Lu, *Inorg. Chem. Front.*, 2021, **8**, 2107–2118.
126 I. Sádaba, M. López Granados, A. Riisager and E. Taarning, *Green Chem.*, 2015, **17**, 4133–4145.
127 A. Zamader, B. Reuillard, J. Pécaut, L. Billon, A. Bousquet, G. Berggren and V. Artero, *Chem. Eur. J.*, , DOI:10.1002/chem.202202260.
128 A. D. Wilson, R. H. Newell, M. J. McNevin, J. T. Muckerman, M. Rakowski DuBois and D. L. DuBois, *J. Am. Chem. Soc.*, 2006, **128**, 358–366.
129 M. L. Helm, M. P. Stewart, R. M. Bullock, M. R. DuBois and D. L. DuBois, *Science*, 2011, **333**, 863–866.
130 S. M. Moni, R. Mahmud, K. High and M. Carbajales-Dale, *J. Ind. Ecol.*, 2020, **24**, 52–63.
131 A. Lotrič, M. Sekavčnik, I. Kuštrin and M. Mori, *Int. J. Hydrog. Energy*, 2021, **46**, 10143–10160.
132 M. A. Curran, Ed., *Goal and Scope Definition in Life Cycle Assessment*, Springer Netherlands, Dordrecht, 2017.
133 European Commission. Joint Research Centre. Institute for Environment and Sustainability., *International Reference Life Cycle Data System (ILCD) Handbook :general guide for life cycle assessment : detailed guidance.*, Publications Office, LU, 2010.
134 M. Goedkoop, R. Heijungs, M. Huijbregts, De Schryver, An de, Struijs, J aap, and Van Zelm, Rosalie, in *ReCiPe 2008, Report I: Characterisation*, Universiteit Leiden, Netherlands, 1st edn., 2009, vol. 1, pp. 1–132.
135 A. Zamader, B. Reuillard, P. Marcasuzaa, A. Bousquet, L. Billon, J. J. Espí Gallart, G. Berggren and V. Artero, *ACS Catal.*, 2023, **13**, 1246–1256.

136 F. Arrigoni, F. Rizza, L. Bertini, L. De Gioia and G. Zampella, *Eur. J. Inorg. Chem.*, 2022, e202200153.
137 G. B. Hall, J. Chen, C. A. Mebi, N. Okumura, M. T. Swenson, S. E. Ossowski, U. I. Zakai, G. S. Nichol, D. L. Lichtenberger, D. H. Evans and R. S. Glass, *Organometallics*, 2013, **32**, 6605–6612.
138 J. Wang, S. Dou and X. Wang, *Sci. Adv.*, 2021, **7**, eabf3989.
139 D. G. Nocera, *Acc. Chem. Res.*, 2017, **50**, 616–619.
140 C. C. L. McCrory, S. Jung, I. M. Ferrer, S. M. Chatman, J. C. Peters and T. F. Jaramillo, *J. Am. Chem. Soc.*, 2015, **137**, 4347–4357.
141 J. Chen, A. K. Vannucci, C. A. Mebi, N. Okumura, S. C. Borowski, M. Swenson, L. T. Lockett, D. H. Evans, R. S. Glass and D. L. Lichtenberger, *Organometallics*, 2010, **29**, 5330–5340.
142 W. P. Brezinski, M. Karayilan, K. E. Clary, N. G. Pavlopoulos, S. Li, L. Fu, K. Matyjaszewski, D. H. Evans, R. S. Glass, D. L. Lichtenberger and J. Pyun, *Angew. Chem. Int. Ed.*, 2018, **57**, 11898–11902.
143 J.-F. Capon, F. Gloaguen, P. Schollhammer and J. Talarmin, *J. Electroanal. Chem*, 2004, **566**, 241–247.
144 L. Schwartz, P. S. Singh, L. Eriksson, R. Lomoth and S. Ott, *C. R. Chim.*, 2008, **11**, 875–889.
145 J. Chen, A. K. Vannucci, C. A. Mebi, N. Okumura, S. C. Borowski, L. T. Lockett, M. Swenson, D. L. Lichtenberger, D. H. Evans and R. S. Glass, *Phosphorus Sulfur Silicon Relat. Elem.*, 2011, **186**, 1288–1292.
146 G. A. N. Felton, A. K. Vannucci, J. Chen, L. T. Lockett, N. Okumura, B. J. Petro, U. I. Zakai, D. H. Evans, R. S. Glass and D. L. Lichtenberger, *J. Am. Chem. Soc.*, 2007, **129**, 12521–12530.
147 A. Le Goff, V. Artero, B. Jousselme, P. D. Tran, N. Guillet, R. Métayé, A. Fihri, S. Palacin and M. Fontecave, *Science*, 2009, **326**, 1384–1387.
148 E. S. Andreiadis, P.-A. Jacques, P. D. Tran, A. Leyris, M. Chavarot-Kerlidou, B. Jousselme, M. Matheron, J. Pécaut, S. Palacin, M. Fontecave and V. Artero, *Nat. Chem.*, 2013, **5**, 48–53.
149 N. B. Williams, A. Nash, N. Yamamoto, M. Patrick, I. C. Tran and J. Gu, *Adv Materials Inter*, 2021, **8**, 2001961.
150 R. J. Wright, W. Zhang, X. Yang, M. Fasulo and T. D. Tilley, *Dalton Trans.*, 2012, **41**, 73–82.
151 G. A. N. Felton, B. J. Petro, R. S. Glass, D. L. Lichtenberger and D. H. Evans, *J. Am. Chem. Soc.*, 2009, **131**, 11290–11291.
152 L. Bertini, C. Greco, L. De Gioia and P. Fantucci, *J. Phys. Chem. A*, 2009, **113**, 5657–5670.
153 J. W. Tye, M. Y. Darensbourg and M. B. Hall, *Inorg. Chem.*, 2006, **45**, 1552–1559.
154 W. P. Brezinski, M. Karayilan, K. E. Clary, K. C. McCleary-Petersen, L. Fu, K. Matyjaszewski, D. H. Evans, D. L. Lichtenberger, R. S. Glass and J. Pyun, *ACS Macro Lett.*, 2018, **7**, 1383–1387.
155 C. Zhan, X. Wang, Z. Wei, D. J. Evans, X. Ru, X. Zeng and X. Liu, *Dalton Trans.*, 2010, **39**, 11255.
156 D. Heine, C. Pietsch, U. S. Schubert and W. Weigand, *J. Polym. Sci. A Polym. Chem.*, 2013, **51**, 2171–2180.
157 A. Zamader, B. Reuillard, L. Billon, G. Berggren and V. Artero, *Manuscript under preparation*.
158 S. Ott, M. Kritikos, B. Åkermark, L. Sun and R. Lomoth, *Angew. Chem.*, 2004, **116**, 1024–1027.

159 J. F. Siebel, A. Adamska-Venkatesh, K. Weber, S. Rumpel, E. Reijerse and W. Lubitz, *Biochemistry*, 2015, **54**, 1474–1483.
160 C. Esmieu and G. Berggren, *Dalton Trans.*, 2016, **45**, 19242–19248.
161 H. Li and T. B. Rauchfuss, *J. Am. Chem. Soc.*, 2002, **124**, 726–727.
162 O. Lampret, A. Adamska-Venkatesh, H. Konegger, F. Wittkamp, U.-P. Apfel, E. J. Reijerse, W. Lubitz, O. Rüdiger, T. Happe and M. Winkler, *J. Am. Chem. Soc.*, 2017, **139**, 18222–18230.
163 G. Goldet, C. Brandmayr, S. T. Stripp, T. Happe, C. Cavazza, J. C. Fontecilla-Camps and F. A. Armstrong, *J. Am. Chem. Soc.*, 2009, **131**, 14979–14989.
164 A. R. Finkelmann, M. T. Stiebritz and M. Reiher, *Chem. Sci.*, 2014, **5**, 215–221.
165 J. L. Hartwell, in *Organic Syntheses*, ed. John Wiley & Sons, Inc., John Wiley & Sons, Inc., Hoboken, NJ, USA, 1944, vol. 24, p. 22.
166 Taiyuan University of Technology, CN 108892103A, 2015.
167 United States Patent, US 3691217, 1972.
168 Statw Intellectual Property Office of Poeple`s republic of China, CN 106279227A, 2017.
169 Paris LaDefense, France, US 4851568A, 1989, 5.
170 United States Patent, US 7335343B2, 2005, 5.
171 A. Yahyazadeh and B. Khoshandam, *Results Phys.*, 2017, **7**, 3826–3837.
172 M. Voll and P. Kleinschmit, in *Ullmann's Encyclopedia of Industrial Chemistry*, John Wiley & Sons, Ltd, 2010, vol. 7, pp. 1–22.
173 *The Annals of Occupational Hygiene*, , DOI:10.1093/annhyg/met042.
174 H. Reihlen, A. V. Friedolsheim and W. Oswald, *Justus Liebigs Annalen der Chemie*, 1928, **465**, 72–96.